First principles phase diagram calculations in group IV carbides and Mg_2SiO_4 liquid from Molecular Dynamics

Von der Fakultät für Biologie, Chemie und Geowissenschaften
der Universität Bayreuth

zur Erlangung der Würde eines Doktors der Naturwissenschaften

- Dr. rer. nat. -

Genehmigte Dissertation

vorgelegt von
Omar Adjaoud
Aus Tizi-Ouzou (Algerien)

Bayreuth, Februar 2009

Prüfungsausschuß:

Prof. J. Breu, Universität Bayreuth	(Vorsitzender)
Prof. D. Rubie, Universität Bayreuth	(1. Gutachter)
Prof. L. Stixrude, University College London	(2. Gutachter)
Prof. F. Langenhorst, Universität Bayreuth	
Prof. St. Kümmel, Universität Bayreuth	

Tag der Einreichung:	13.02.2009
Tag des wissenschaftlichen Kolloquiums:	10.06.2009

Contents

Zusammenfassung

Atomistische Simulationen der Stabilität und physikalischen Eigenschaften von Erdmaterialien spielen eine zunehmend wichtige Rolle in der Hochdruck-Mineralogie. Sie geben Einblicke in Materialverhalten und können bei der Planung von Experimenten hilfreich sein. Sie erlauben es auch, Eigenschaften zu untersuchen und physikalische Bedingungen zu erreichen, die experimentell noch nicht zugänglich sind. Besonders Methoden aus der Dichtefunktional-Theorie haben sich dabei als zuverlässig erwiesen. Es ist inzwischen möglich, ein großes Spektrum an Mineralzusammensetzungen und zahlreiche Eigenschaften mit Hilfe der Dichtefunktional-Theorie zu berechnen. Es gibt jedoch immer noch interessante Probleme, die mit solchen Methoden nicht zugänglich sind. Die Berechnung von Phasendiagrammen in chemisch komplexen Systemen und Transporteigenschaften von Schmelzen gehören dazu.

Die Phasendiagramme der binären Karbide TiC-ZrC, TiC-HfC und ZrC-HfC wurden hier mit Hilfe von Elektronenstruktur- und Energieberechnungen aus der Dichtefunktional-Theorie bestimmt. Bildungsenergien einer großen Zahl von Zellen mit einer Zusammensetzung (M,M')C, mit M,M'=Ti, Zr oder Hf, wurden mit Hilfe von Pseudopotentialen berechnet. Die dabei bestimmten Energien bilden die Basis für die Anpassung eines Cluster-Entwicklungs Hamilton-Operators, der durch Monte-Carlo Simulationen effizient zur Berechnung des festen Phasendiagrams eingesetzt wird, d.h. zur Berechnung der Mischbarkeit von verschieden Komponenten. Der Hamilton-Operator kann direkt aus den statischen Bildungsenergien bestimmt werden oder unter Berücksichtigung der Vibrationsenergie des Gitters. Da die Berechnung der Vibrationsenergie für die große Zahl an Strukturen unmöglich ist, wird eine transferierbare Kraftkonstanten-Näherung verwendet: Kraftkonstanten werden für direkte Nachbarn in Abhängigkeit des Bindungsabstandes berechnet. Diese Kraftkonstanten werden für alle Strukturen verwendet, indem jeweils Bindungslänge und Bindungspartner bestimmt werden und die entsprechende Kraftkonstante Anwendung findet. Hiermit wurden in TiC-ZrC und HfC-TiC große Mischungslücken vorhergesagt, die erst bei Temperaturen von mehr als 2000 K geschlossen werden. Das System HfC-ZrC zeigte vollständige Löslichkeit schon bei Raumtemperatur. Für HfC-TiC wurde ein nahezu symmetrisches Phasendiagramm vorhergesagt, während für HfC-ZrC und TiC-ZrC asymmetrische Phasendiagramme bestimmt wurden.

Flüssiges Mg_2SiO_4 unter hohem Druck ist für den Magma-Ozean der frühen Erde von großer Wichtigkeit. Aufgrund des hohen Schmelzpunkts sind Experimente in diesem System schwierig, und das Wissen über thermodynamische und Transporteigenschaften ist begrenzt. Simulationen mit Hilfe der Molekulardynamik können diese Lücke füllen. Im Moment sind Berechnungen, die auf Dichtefunktional-Theorie beruhen auf wenige hundert Atome und Simulationsdauern von wenigen Picosekunden beschränkt. Während solche Simulationen die Bestimmung von thermodynamischen Eigenschaften erlauben, sind zur Berechnung von Transporteigenschaften mit ausreichender Genauigkeit längere Simulationen und größere Zellen notwendig. Im Gegensatz dazu erlauben klassische Potentiale Berechnungen mit einer großen Zahl von Atomen und langen Simulationszeiten. Solche Potentiale sind jedoch nur beschränkt zwischen verschiedenen Bedingungen transferierbar, und Resultate deshalb von bedingter Aussagekraft. Die Entwicklung von flexiblen (aspherischen) Potentialen, die an Ergebnisse aus der Dichtefunktionaltheorie angepasst

werden, füllt die Lücke zwischen diesen beiden Methoden.

Eine solche Potentialmethode wurde für Molekulardynamik-Simulationen an Mg_2SiO_4 Schmelze angewandt, um deren thermodynamische und Transporteigenschaften bei hohem Druck (0-32 GPa) und hoher Temperatur (2600-3200 K) zu berechnen. Die Ergebnisse für thermodynamische Eigenschaften stimmen gut mit den Berechnungen mit Hilfe der Dichtefunktionaltheorie überein. Ins Besondere wurde ein Grüneisen-Parameter γ gefunden, der mit Druck zunimmt. Die Simulationen ergaben für Diffusivität eine Abnahme mit Druck und für die Viskosität eine Zunahme. Beide Transporteigenschaften folgen einem Arrhenius-Gesetz über den gesamten Druck- und Temperaturbereich. Da Diffusivität und Viskosität unabhängig voneinander bestimmt wurden, kann hier die Eyring-Beziehung untersucht werden, die oft zur Umrechnung von Diffusivität zu Viskosität verwendet wird: der Proportionalitätsfaktor in dieser Beziehung, die Länge für ein Diffusionsereignis, wurde mit λ=18 Å bei 0 GPa bestimmt. Dieser Wert stimmt gut mit Ergebnissen von klassischen Molekulardynamik-Simulationen überein, ist jedoch deutlich größer als experimentelle Bestimmungen, die 2.8 Å $< \lambda <$ 5 Å ergaben. Aus den Ergebnissen wurden eine Adiabate und das dazugehörige Viskositätsprofil für den Magmaozean berechnet.

Summary

Atomistic simulations on stability and physical properties of Earth materials are playing an increasingly important role in high pressure mineralogy. Such computations can provide guidance for experimental studies and insight into underlying causes of observations, or explore conditions and properties that are inaccessible to experiments at the current time. A variety of approaches have been applied in such research, with density functional theory based methods having become a reliable tool in computational mineral sciences. Despite this progress there are interesting problems which density functional theory based methods are not able to tackle on a routine basis. These include computations of phase diagrams and transport properties in liquids.

The sub-solidus phase diagrams of the binary systems TiC-ZrC, TiC-HfC, ZrC-HfC at ambient pressure are computed based on electronic structure and energy calculations within density functional theory. Formation energies for a large number of supercells with compositions of (M,M')C, M,M'=Ti, Zr, or Hf, are computed by a plane-wave pseudopotential method. The energies serve as a basis for fitting cluster expansion Hamiltonians that are used to explore the sub-solidus phase diagram, i.e. stability of ordered intermediate compounds and the degree of miscibility in the systems by Monte Carlo simulations. Hamiltonians can be fit to the formation energies of the cells directly or after taking into account vibrational free energy. As it is prohibitive to compute vibrational free energy for all configurations they are approximated by the transferable force constant scheme: nearest neighbor force constants are computed for the end-member crystals with imposed but varying lattice parameters. The resulting bond stiffness versus bond length relationships are applied to the superstructures, using the relaxed bond lengths and their chemical identities as predictor. Significant miscibility gaps were predicted for the binaries TiC-ZrC and HfC-TiC, with consolute temperature in excess of 2000 K, in good agreement with experiments. The system HfC-ZrC shows complete miscibility at room temperature. Approximately symmetric phase diagram for HfC-TiC and asymmetric phase diagrams for HfC-ZrC and TiC-ZrC were predicted. With the success of the method in the simple carbide systems similar computations can now be performed for geologically relevant mineral families.

Mg_2SiO_4 liquid at high pressure is of central importance in our understanding of melts that occur in the deep Earth and in particular in the early history of our planet, when it was in a magma ocean stage. Due to high melting temperatures little is known experimentally about its high pressure thermodynamic and transport properties that govern magma ocean structure and dynamics. Molecular dynamics simulations now fill this gap. Currently, density functional theory based computations are restricted to a few hundred atoms and a few picoseconds. While such simulations allow for determination of thermodynamic properties, longer run durations and larger cells are necessary to obtain transport properties such as diffusivity and viscosity with sufficient precision. By contrast, semi-empirical pair potentials provide an efficient route to perform large-scale molecular dynamics simulations. They suffer, however, from the fact that the transferability of the potentials to different conditions is not guaranteed. The development of aspherical flexible potentials that are fit to density functional theory results bridge the gap between ab-initio methods and classical potentials.

Comprehensive large-scale molecular dynamics simulations using the aspherical ionic model were performed on Mg_2SiO_4 melt to obtain thermodynamic properties as well as diffusivity and viscosity. The pressure-temperature range covered was 0-32 GPa and 2600-3200 K. The thermodynamic parameters agree well with density functional theory based results: the Grüneisen parameter γ was found to increase significantly with pressure. Diffusivity is predicted to decrease and viscosity to increase with pressure. Both transport properties were readily fit with closed Arrhenius expression. Independent estimates on diffusivity and viscosity allows an examination of their relation through the Eyring equation, often employed to compute viscosity from diffusivity data. The proportionality factor between them, the translation distance for a diffusion event λ, is determined as λ=18 Å at 0 GPa, and decreases with pressure. This is in good agreement with previous molecular dynamics simulations using classical potentials, but significantly larger than other estimates of λ based on experimental data that yield 2.8 Å $< \lambda <$ 5 Å. Combining the thermodynamic and viscosity fits a magma ocean adiabat and the associated viscosity profile were computed.

Chapter 1

Introduction

1.1 Motivation

Knowledge of the composition and structure of the Earth's interior is necessary for understanding a wide range of geophysical phenomena and their origin and evolution. Our information of the Earth's deep interior comes from geophysical observations, geochemical studies of natural rocks and minerals, numerical simulations of mantle dynamics, as well as experimental and theoretical studies on the physical and chemical properties of Earth materials at high pressures and temperatures.

The most detailed information about the structure of the Earth comes from analysis of seismic waves. The mantle is characterized by major seismic velocity discontinuities at 410 and 660 km depths which forms a transition zone. These discontinuities are caused by phase transformations. At a depth of 410 km, $(Mg,Fe)_2SiO_4$ olivine transforms to the high-pressure polymorph of wadsleyite β-$(Mg,Fe)_2SiO_4$. At a depth of 660 km, which is the bottom of the transition zone and top of the lower mantle, ringwoodite breaks down to an assemblage of $(Mg,Fe)(Si,Al)O_3$ with the perovskite structure and (Mg,Fe)O magnesiowüstite. The region that lies just above the core-mantle boundary (D'' layer) is one that exhibits significant heterogeneity and anomalous properties [1].

The phase stability of minerals plays a crucial role in understanding the geophysical and geochemical properties of Earth. Relations between structural, thermodynamic and physical properties are derived for various types of phase transition induced by changing temperature, pressure or composition. Phase diagrams of minerals help to explain seismological data and the geochemical signature of rocks. The recent experimental and theoretical [2–4] discovery of a post-perovskite phase ($CaIrO_3$-type structure) in $MgSiO_3$ holds the key to understanding the shear-wave discontinuity at the top of the D'' layer, with important implications for heat transport, thermal instabilities, and chemical properties of the lower mantle.

Melting is a ubiquitous process in planetary interiors that has major consequences for their chemical and thermal evolution. The properties of silicate liquids are thus essential for understanding a wide range of geophysical phenomena related to the deep Earth and its origin and evolution. There are a number of lines of evidence that strongly indicate that the Earth and other terrestrial planets were partially or wholly molten, at least at certain intervals, during the accretion process [5, 6]. In this context viscosity of silicate melts is the most important physical property as it controls a range of processes such as

convection dynamics [7], crystal growth [8], and crystal settling [9]. In addition, transport properties of silicate melts (viscosity and diffusion) would have strongly influenced early differentiation mechanisms. In the present mantle, partial melting may explain the ultra-low-velocity zone (ULVZ) found in the D″ layer near the core-mantle boundary [10, 11]. In addition, gravitationally stable partial melt layers have also been proposed in the upper mantle such as at the top of the 410 km discontinuity [12–14].

Despite this importance, the knowledge of thermodynamic and transport properties of silicate melts is limited. Melt with bulk Earth composition is characterized by high temperatures, which makes measurements challenging even at ambient pressure. Extrapolation of experimental data from supercooled liquids to high temperatures [e.g. 15] or extrapolation using partial molar models [e.g. 16, 17] in order to obtain heat capacity [15, 18, 19] or compressibility [16, 20, 21] at ambient pressure can be used as a benchmark of thermodynamic investigation of silicate melts.

At ambient pressure, viscosity of liquid silicates [22] can be measured using the rotating cup method [23]. At high pressure *in-situ* viscosity measurements of silicate melts are investigated by the "falling sphere" method, in which the sinking velocity of a solid sphere through a liquid can be related to viscosity through Stokes' law [24–26]. For low viscosity depolymerized melts, such as diopside [25], peridotite [26] or the Mg_2SiO_4 liquid studied in this thesis, the fast sinking velocity makes the measurements challenging. In addition, the rapid increase of melting temperature with pressure for Mg_2SiO_4 [27] makes high pressure experiments even more difficult and scarce.

1.1.1 Experimental approaches

High pressure experimental methods involve synthesising samples under high pressure conditions and either studying them *in-situ*, or looking at quenched samples. This can involve different techniques such as piston-cylinder presses, multi-anvil presses, diamond anvil cell (DAC), or dynamic compression by shock waves.

The piston-cylinder apparatus [28] works by the principle of pressure amplification. The sample is place in a cylindrical hole inside a 'bomb' or pressure vessel made from tungsten carbide. Pressure is applied by forcing a tungsten carbide anvil into the hole. This uniaxial compression is converted to a more hydrostatic force by surrounding the sample with a soft, deformable material such as pyrophyllite or NaCl. Samples are heated using an internal graphite resistance furnace. With the piston cylinder apparatus, pressures up to ∼5 GPa and temperatures up to 2200 °C can be achieved, with a sample volume of typically ∼200 mm^3. The piston-cylinder press is durable and robust, and maintains high pressures and temperatures over long periods of time, days to even weeks.

Higher pressures can be achieved using a multi-anvil apparatus. The sample cell in such designs is octahedral. Samples are loaded into holes drilled in ceramic octahedra which acts as the pressure medium. The faces of the octahedron seat against the truncated corners of a series of eight tungsten carbide (or occasionally sintered diamond) anvils [29]. This series of eight anvils forms one stage of the device. A second stage is comprised of two sets of three wedges, which act upon the faces of the assemblage of anvils. As with the piston-cylinder apparatus, an internal resistance furnace (graphite or $LaCrO_3$) is used to achieve simultaneously high temperatures. Multi-anvil apparatus can produce

much higher pressures than the piston-cylinder. Depending on the choice of the cubes and load, up to 25 GPa can be achieved at up to ∼2700 °C, and conditions can be controlled for time periods of several hours. The sample volumes are between 14 mm^3 for lower pressures and ∼1 mm^3 for higher pressures

The DAC is based upon the opposed-diamond configuration, in which a sample is placed between the polished culets of two diamonds and is contained on the sides by a metal gasket [30]. The two most common methods of heating on DACs are internal laser heating and external electrical heating. In addition to being recognized as the hardest and least compressible material, diamond has the important property of being transparent to most of the spectrum of electromagnetic radiation, including X-ray, portions of ultraviolet, visible, and most of the infrared region. The pressure at the centre of the Earth (365 GPa) can be achieved with DAC at high temperatures. However, sample volumes are as small as 0.0002 mm^3.

In shock compression, shock waves are generated in a sample target essentially using explosives or high-velocity projectiles launched by a light-gas (hydrogen) gun. The quantities measured are the shock wave velocity U_s and the "particle velocity" U_p (the velocity imparted to the particles of the sample by shock wave) as well as the temperature. From U_s and U_p the pressure and density can be obtained using the Rankine-Hugoniot equations. Details of the experimental apparatus and methods of measurement are given in reference [31].

1.1.2 Computational approaches

Computational simulations provide an alternative approach to study properties of materials at high pressure and temperature which have supplemented experimental efforts over the past two decades.

Molecular dynamics (MD) simulations using semi-empirical potentials have been used to study structural, thermodynamical, and transport properties of silicate melts [e.g. 32–34]. They have the advantage that the potentials allow for long simulation times that are important for reliably constraining transport properties. However, the transferability of the potentials used at high pressure and temperature must be evaluated carefully.

Recent developments in the atomistic simulation of solids and liquids based on the full solution of the quantum mechanical equations for the electrons based on Hartree-Fock and DFT allow the theoretical study from first principles of the structural, thermal, and elastic properties of minerals at arbitrary conditions of pressure and temperature [e.g. 35–38]. First principles calculations are accurate and transferable to different structure types and to different thermodynamic conditions. However, computational requirements pose severe limitations on the maximum simulation cell sizes and run durations. In order to go beyond the limitions of semi-empirical potentials and first principles calculations, a flexible aspherical ion model [39, 40] has been proposed to bridge these two approaches. The parameters of the potential are fitted to reproduce first principles results. This potential has been applied successfully for oxides and silicates in solid and melt phases [e.g. 39–42].

Computer simulations have been able to guide experiments or shed light on numerous situations in the mineral and Earth sciences over the past year. Two examples illustrate

the contributions of computational work in advancing our understanding of minerals and physical properties at high pressure.

For lower mantle mineralogy Stixrude *et al.* [43] have investigated the lattice dynamics of $CaSiO_3$ with the linear response perovskite and predicted a low temperature distortion from the commonly assumed cubic symmetry. This work has been followed up by a large number of other *ab-initio* computations [44–49] that did also predict different types of distortions, only recently been confirmed experimentally [50] and the distortion has been identified to be tetragonal.

Elastic constants for hexagonal transition metals are the center of interest of Earth sciences as the Earth's solid inner core is most likely composed of hcp iron [51], and elastic constants of this phase are necessary to interpret the elastic anisotropy in the inner core [52]. In the late 1990s experimental efforts have focused on determining the elastic constants in the diamond anvil cell through lattice strain experiments in which a sample is exposed to non-hydrostatic stress and the resulting changes in lattice parameters can be evaluated by means of the elastic constant tensor [53]. By computing the pressure dependence of the elastic constant tensor for rhenium which crystallizes in the hcp phase even at ambient pressure [54] and comparing the results to lattice strain experiments on the same material [55] computations show that the method can not reliably be applied for hcp metals as it measures not only the elastic but also the plastic response of the sample [56].

1.2 Methods

Computer modeling has become a powerful tool in material science, engineering, nanotechnology, and geomaterials. Through direct access to the atomic structure and the respective atomic motions, a fundamental atomistic understanding of macroscopic observations may be achieved. Furthermore, simulations allow to make predictions for physical and chemical properties of materials, supplementing experimental efforts. Different techniques exist to study materials from an atomistic viewpoint.

1.2.1 Electronic structure computations

Density functional theory (DFT) [57, 58] computations have the desirable aspects of accuracy, and reliability with virtually no empirical input for most condensed matter systems. DFT has become the primary tool for calculating the electronic structure in condensed matter, and is increasingly important for quantitative studies of molecules and other finite systems. The remarkable successes of the approximate local density (LDA) [59] and generalized-gradient approximation (GGA) [60] functionals within the Kohn-Sham approach [59] have led to widespread interest in DFT as the most promising approach for accurate, practical methods in the theory of materials.

The modern formulation of DFT originated in Hohenberg and Kohn theorems, formulated in 1964 [57]. They did show that a special role can be assigned to the electron density in the ground state of a quantum many-body system: the electronic density $n(r)$ can be considered as a "basic variable", *i.e.* all properties of the system can be considered

to be unique *functionals* of the ground state density. Following in 1965, Mermin [58] extended the Hohenberg-Kohn arguments to finite temperature canonical and grand canonical ensembles. Although the finite temperature extension has not been widely used, it illuminates both the generality of DFT and the difficulty of realizing the promise of exact DFT. Also in 1965 appeared the other classic work of this field by Kohn and Sham [59], whose formulation of DFT has become the basis of most present-day methods for treating electrons in atoms, molecules, and condensed matter.

Born-Oppenheimer Approximation

One of the most important approximations used in solid state physics is the *Born-Oppenheimer Approximation* which deals with the motion of nuclei of atoms with respect to electrons. Since the electronic problem (with N electrons) is already not trivial, adding the nuclei of atoms into the equation is too complicated to be solved analytically or numerically. A way to avoid these additional complications is to use the fact that the mass of the electrons is much smaller than the mass of the nuclei, meaning that the electrons move much faster than the nuclei and adjust adiabatically to the position of the nuclei, which change on a much longer time scale. Therefore one may consider for the electronic problems the positions of ions ($\vec{R}_i$) as fixed and determine the ground state energy $E_0(\vec{R}_0, ...\vec{R}_n)$ for these given positions $\vec{R}_0, ...\vec{R}_n$ of the n nuclei. The motion of the nuclei then requires the solution of the Hamiltonian $\sum_{n'} -\frac{1}{2M_{n'}}\nabla^2_{n'} + E_0(\vec{R}_0, ...\vec{R}_n)$ where the ground state energy of the electronic problem acts as an interaction potential for the nuclei.

Here and in the following, atomic units are used ($\hbar = 1$; $m_e = \frac{1}{2}$; $e^2 = 2$; energies in Rydberg, 1 Ry = 13.6058 eV; lengths in units of Bohr radius).

Hohenberg-Kohn Theorems

The approach of Hohenberg and Kohn is to formulate a density functional theory as an *exact theory of many-body systems*. The formulation applies to any system of interacting particles in an external potential $V_{ext}(\vec{r})$, including the problem of electrons in the field of fixed nuclei, for which the Hamiltonian can be written as

$$\mathcal{H} = \sum_{i=1}^{N} -\nabla_i^2 + \sum_{i,j} \frac{1}{|\vec{r}_i - \vec{r}_j|} - \sum_i V_{ext}(\vec{r}_i). \tag{1.1}$$

Kohn-Sham Approach

Kohn and Sham [59] used the variational principle implied by the minimal properties of the energy functional to derive single-particle Schrödinger equations for the electrons. For this the energy functional is first split into four parts:

$$E[n] = T[n] + \int\int \frac{n(\vec{r})n(\vec{r'})}{|\vec{r} - \vec{r'}|} d\vec{r} d\vec{r'} + E_{xc}[n] + \int n(\vec{r}) V_{ext}(\vec{r}) d\vec{r} \tag{1.2}$$

which describes the kinetic, the Hartree, the exchange-correlation and the external energy. In contrast to the Hartree integral, an explicit form of the other functionals, T and E_{xc},

is not known in general. Ignoring this problem for the moment, the variational principle is used and we obtain

$$\frac{\delta E[n]}{\delta n(\vec{r})} = -\mu \frac{\delta(N - \int n(\vec{r})d\vec{r})}{\delta n(\vec{r})} = \mu, \tag{1.3}$$

where μ is a Lagrange multiplier taking care of particle conservation. The kinetic energy is now split into a term T_0 implying the kinetic energy functional $T_0[n(\vec{r})]$ of noninteracting particles and T_{xc} which stands for the rest, *i.e.* we write

$$T = T_0 + T_{xc}. \tag{1.4}$$

This is an important step because it is known how to calculate the kinetic energy T_0 for noninteracting particles and hence one can determine the functional derivative $\delta T_0[n]/\delta n(\vec{r})$ by using

$$n(\vec{r}) = \sum_{i=1}^{N} |\Phi_i(\vec{r})|^2 \tag{1.5}$$

where the summation is over N states with lowest eigenvalues and

$$T_0[n] = \sum_{i=1}^{N} \int \nabla \Phi_i^*(\vec{r}) \nabla \Phi_i(\vec{r}), \tag{1.6}$$

Φ being a single particle wave function.

By varying the latter equation and after adding a potential-energy term the Euler-Lagrange equation is obtained which is also, in fact, a single-particle Schrödinger equation:

$$(-\nabla^2 + v'(\vec{r}))\Phi_i(\vec{r}) = \epsilon_i \Phi_i(\vec{r}) \tag{1.7}$$

We try to determine the potential energy $v'(\vec{r})$ such that the density $n(\vec{r})$ obtained from eq. (1.5) minimizes the total energy. Thus, multiplying eq. (1.7) with $\Phi_i^*(\vec{r})$, requiring the functions $\Phi_i(\vec{r})$ to be normalized, integrating and summing up, we obtain

$$T_0[n] = \sum_{i=1}^{N} \epsilon_i - \int v'(\vec{r}) n(\vec{r}) d\vec{r}. \tag{1.8}$$

The variation (eq. (1.3)) is now easily carried out. We note that terms containing $\delta\epsilon_i$ cancel $\delta v'$ (because of eq. (1.7)) and obtain $v'(\vec{r})$ which is called the effective single particle potential $v_{eff}(\vec{r})$:

$$v_{eff}(\vec{r}) = v_{ext}(\vec{r}) + 2 \int \frac{n(\vec{r'})}{|\vec{r} - \vec{r'}|} d\vec{r'} + v_{xc}(\vec{r}) \tag{1.9}$$

with

$$v_{xc}(\vec{r}) = \frac{\delta(E_{xc} + T_{xc})}{\delta n(\vec{r})}. \tag{1.10}$$

By varying $E[n(\vec{r})]$ with respect to $\Phi_i(\vec{r})$ instead of $n(\vec{r})$ and adding the Lagrange constraint $\sum_i \epsilon_i (\int d\vec{r} \Phi * (\vec{r})) \Phi(\vec{r}) \quad - 1)$ for the normalisation of the Φ, the following so-called Kohn-Sham equation is obtained for the single partial wave function Φ_i

$$\big[-\nabla^2 + v_{eff}(\vec{r}) - \epsilon_i \big] \Phi_i(\vec{r}) = 0. \tag{1.11}$$

It is a Schrödinger equation with the external potential replaced by the effective potential which depends on the density. The density itself depends on the single-particle states Φ_i via eq. (1.5). The Kohn-Sham equation thus constitutes a self-consistent field problem.

Although density-functional theory as outlined above provides a scheme to reduce the entire many-body problem to a Schrödinger-like effective single-particle equation, the eigenvalues ϵ_i have no direct physical meaning since they have been introduced only as Lagrange parameters. Nevertheless, they are often and quite successfully taken as approximate excitation energies.

Exchange and Correlation Approximations

The simplest approximation for the exchange-correlation functional is the local density approximation (LDA), first suggested in the original work of Kohn and Sham [59], and then generalized to spin-polarized systems [61–63] (local spin density approximation or LSDA). In the LDA it is assumed that the contribution to the exchange correlation energy from each point r with the local electron density n(r) is the same as in the uniform electron gas with the corresponding electron density n(r). That is, the exchange-correlation functional takes the form

$$E_{xc}^{LDA} = \int d\vec{r} n(\vec{r}) \epsilon_{xc}^{hom}[n(\vec{r})], \tag{1.12}$$

where $\epsilon_{xc}^{hom}(n)$ is the exchange-correlation energy per particle in the homogeneous electron gas with density n. For the homogeneous electron gas, an accurate dependence of ϵ_{xc} on the density n is extracted from quantum Monte Carlo calculations [64], and then, in one or another way, parametrized to simplify its application [65–67].

Although by construction the LDA approximation is expected to work only for systems with slowly varying density, it appears to be quite accurate for many atomic, molecular and condensed matter systems even with significant density variations. Not surprisingly, there are many situations where the LDA leads to unacceptably large errors and even qualitatively wrong results (for details see Refs. [68, 69]). In particularly the LDA (and the LSDA) noticeably overestimates the bonding strength in most transition metals [70] and their compounds[71–74], and can give a wrong ground-state structure, like for iron [75].

A natural way to improve on the LDA (LSDA) is to include density gradients in the approximate exchange-correlation functional. The most straightforward procedure, suggested in Ref. [59], is to add to the LDA functional one more non-zero term in the gradient expansion of the exchange-correlation functional (gradient expansion approximation or GEA). In reality, the GEA appears to be much worse than the LDA. The basic problem is that gradients in real materials are so large that the expansion breaks down. To overcome these problems, the generalized gradient approximation (GGA) has been introduced [60]. In GGA the gradient expansion is replaced by generalized functionals of density gradients, which are designed to incorporate the important features of the exact exchange-correlation functional. In contrast to the LDA, there is no unique definition of ϵ_{xc}^{GGA}, and many different functional forms have been suggested, as reviewed in Ref. [69].

The most commonly used version of GGA is that of Perdew and Wang 1991 (PW91) [76] and Perdew, Burke and Ernzerhof [77] (PBE). The last one improves the accuracy

of the description of the ground-state properties of many atomic, molecular and solid systems [69, 78]. In view of this fact the present work uses GGA-PBE.

Implementations: basis functions

The first step of any numerical implementation of the DFT is to represent the Kohn-Sham wave functions (Φ_i) as discrete functions of numbers. This is done by expanding the wave functions in some basis functions, and truncating such an expansion at some finite number of terms. Then the desired discrete representation is given by the coefficients of the expansion. The choice of basis functions is crucial for the efficiency of the computational method. With the optimal choice, as few expansion terms as possible should be necessary to represent the wave functions with a reasonable accuracy. The most common basis functions can be divided into three categories: plane waves, localized, and mixed basis functions.

A basis of plane waves (PW) [79] presents several useful features: (i) plane waves treat equally all regions of space; (ii) they constitute a complete and orthogonal set; (iii) the plane wave basis is independent of the coordinates of the nuclei. In particular, for periodic systems the PW basis presents the added advantage that they are inherently periodic themselves. Of course, completeness is only achieved if an infinite number of plane waves is used whereas a finite (truncated) set must be chosen for computational reasons. However, convergence to completeness can be easily monitored by increasing the number of plane waves until the calculated properties do not change as the size of the basis set is increased.

For systems with localized states and large regions of vacuum or very low charge density regions, methods using localized basis functions are often thought to represent a more suitable choice [80]. The SIESTA code [81] is such an implementation, with strictly confined numerical basis functions, that can include multiple-zeta and polarization orbitals. The one-particle problem is solved using linear combination of atomic orbitals (LCAO), within a $\vec{k}$-space representation, in a standard norm-conserving pseudopotential [82] scheme, so the basis refers only to valence electrons. The localized basis are written in a real space numerical mesh, so the accuracy of a given calculation is dependent on the mesh definition (fineness of the mesh). The way SIESTA is implemented relates the fineness of the mesh to an energy cutoff, analogous to the cutoff in a PW basis set.

Mixed basis functions are built up by a basis set constituted by plane waves and localized functions. They consists of localized functions centred at atomic sites which are chosen to optimize the description of localized orbitals near atomic site, and plane waves to account for the remaining (in interstitial region) smooth contributions of the wave functions. The mixed basis functions are implimented in Linearized Augmented Planewave (LAPW) Method [83]. The localized functions nature of the mixed basis functions in the vicinity of the atoms leads to an efficient representation, while the plane wave nature in the interstitial region allows for highly accurate solutions for any atomic arrangement: close-packed or open, high-symmetry or low, surfaces or bulk. However, the generality and accuracy of LAPW method comes at a price: there is a large basis set of plane waves.

Pseudopotentials

First-principles methods can be divided into two major categories: the all-electron (AE) and pseudopotential [84] (PP) types. AE methods explicitly account for all electrons in the system, usually employing mixed basis functions in which the plane waves are augmented around each ionic species in order to describe the complex features of the wave function near the nuclei. Although AE methods are very accurate, they are also generally quite expensive. By contrast, PP methods are approximations to the AE case that dramatically reduce the cost associated with such simulations and are based on the fact that the electronic states of an atom generally are well separated energetically into discrete core and valence electronic states. Since only valence electrons contribute significantly to the bonding and many other properties, it is therefore tempting to reduce the AE problem to one of pseudoatoms in which only valence electrons are taken into account explicitly in the DFT equations. Such pseudopotentials are derived from first-principles calculations on isolated atoms, where one first performs an AE calculation in order to get the AE wave functions and eigenenergies. Then a new set of pseudo-wavefunctions is constructed so that within some core cutoff radius r_c, often corresponding to the outermost extremum of the AE wave function, the AE wave functions are smoothed out to obtain smooth and nodeless pseudo-wave-functions. Beyond this cutoff radius, and because it is desirable that the atomic properties are correctly described in the valence region, the pseudo-wave-functions match the AE.

Although PP methods are an approximation to the AE case, they have been shown to yield results very similar to AE methods, and years of development of the method have made it a very efficient, accurate, and robust tool for studying the electronic properties of materials. Nevertheless, the otherwise reliable PP theory frequently produces unsatisfactory results (in the sense of being highly sensitive to parameter choice) for the case of transition elements [85, 86] and as a consequence, the method has been used sparingly for materials containing transition metal atoms.

1.2.2 Potential models: atomic discription

The impact of atomistic modeling is constrained mainly by two factors: the accuracy of the model and the accessible length and time scales. Due to the considerable increase in computing power in recent years, the usage of very accurate quantum-chemical methods to calculate structural and dynamic properties of complex geomaterials has become feasible. Electronic structure methods in the framework of DFT provide a means of modeling accurately a wide range of structures and chemical compositions from first-principles, i.e. without specific assumptions for the atomic interaction in a specific structure. Approximations have to be made for the exchange-correlation functional. Although being accurate and transferable, DFT is currently limited to systems with a few hundred atoms and time scales of a few picoseconds. In many cases, this is sufficient to study, e.g. the equations of state and the elastic constants of minerals [87], the relative phase stability of different crystal phases as a function of pressure, P, and temperature, T [88], or crystal defect calculations [89].

For larger scale problems (several hundreds to millions of atoms, hundreds of picoseconds to nanoseconds), required, e.g. for modeling of viscous melts, interfaces or grain

boundaries, interatomic potentials are typically employed. In this case, the atomic interactions are described by a more or less complex analytical function. Its parameters are optimized either by reference to experimental data [90–92] or higher level theoretical methods [93–95].

Typical pair potential: Rigid Ion Model (RIM)

Interatomic potentials for ionic materials have been developed over the years by using the ionic model mostly with formal charges and describing the short-range interactions in terms of pair potentials of the Born-Mayer and Buckingham form [96]. In this model the ions are treated as rigid particles which are undistorted by their environment. The typical form of this potential is

$$V_{ij}(r_{ij}) = \frac{q^i q^j}{r_{ij}} + B_{ij} e^{-\alpha_{ij} r_{ij}} - \frac{C_{ij}}{R_{ij}^6} - \frac{D_{ij}}{R_{ij}^8}, \tag{1.13}$$

where V_{ij} and r_{ij} are the interaction energy and the distance of particles i and j, respectively. q^i and q^j are charges on the ions and the first term (V^M) of the expression is electrostatic energy (Madelung potential) of the point charges and is generally evaluated by the method of Ewald summation [97]. The second term (V^{rep}) reflects the fact that an isolated electro distribution tails off exponentially and so the repulsion between ions at short range due to the Pauli exclusion principle can be approximated by a constant B_{ij} times an exponential overlap of ionic charge distributions; the final two terms (V^{pol}) model the ion dispersion interactions which are always attractive and which represent van der Waals, as a sum of dipole-induced dipole (R_{ij}^6 term), dipole-induced quadrupole (R_{ij}^8 term) and higher order terms which are generally neglected.

Recently, Guillot and Sator [33, 34], and Lacks *et al.* [32] have used this type of potential to study silicate melts at high pressure. This potential form has the advantage that it has a pairwise form and it is quick and easy to evaluate, so that relative large system sizes and long times may be simulated with relative ease. However, it has been recognized for a long time that this form does not contain some of physics relevant for many real ionic systems. q^i,α_{ij},B_{ij},C_{ij}, and D_{ij} are parameters of the model which may be determined by physical reasoning, empirical considerations or by fitting to data obtained from ab initio calculations. Introducing a functional (self-consistence) or environment-dependent (such as coordination) parameters can result in the force field method to become a many body problem [39–42, 95, 98–103].

Flexible potential: Aspherical Ion Model (AIM)

Many systems contain anions, which have an appreciable size relative to interionic distances and which are not rigid, in the sense that they become aspherically distorted and can change their size in the condensed phase depending on their environments. This, in practice, can be realized by slightly modifying the second term (V^{rep}) and the final two terms (V^{pol}) and the total Hamiltonian so that the parameters described above (B_{ij}, C_{ij}, and D_{ij}) become three dimensional variables. Such methods have been developed and advanced by Madden *et al.* [39, 40].

The repulsive part of the potential can be written as:

$$\begin{aligned} V^{rep} &= \sum_{i\in O, j\in Mg,Si} [A^{-+}e^{-a^{-+}\rho^{ij}} + B^{-+}e^{-b^{-+}\rho^{ij}} + C^{-+}e^{-c^{-+}r_{ij}}] \\ &+ \sum_{i,j\in O} A^{--}e^{-a^{--}r_{ij}} \\ &+ \sum_{i\in O}[D(e^{\beta\delta\sigma^i} + e^{-\beta\delta\sigma^i}) + (e^{\zeta^2|\nu^i|^2} - 1) + (e^{\eta^2|\kappa^i|^2} - 1)], \end{aligned} \tag{1.14}$$

with

$$\rho^{ij} = r_{ij} - \delta\sigma^i - S^{(1)}_\alpha \nu^i_\alpha - S^{(2)}_{\alpha\beta}\kappa^i_{\alpha\beta}. \tag{1.15}$$

Summation over repeated indices is implied. a^{-+}, b^{-+}, and c^{-+} are characterizing the rate at which the atomic electron densities decay. A^{-+}, B^{-+}, and C^{-+} are some universal energies scale relating the amount of overlap to the replusive energy. The variable $\delta\sigma^i$ characterizes the deviation of the radius of oxide anion i from its default value, ν^i_α are a set of three variables describing the Cartesian components of a dipolar distortion of the ion, and $\kappa^i_{\alpha\beta}$ are a set of five independent variables describing the corresponding quadrupolar shape distortions ($\mid \kappa \mid^2 = \kappa^2_{xx} + \kappa^2_{yy} + \kappa^2_{zz} + 2(\kappa^2_{xy} + \kappa^2_{xz} + \kappa^2_{yz})$ with a traceless matrix κ). $S^{(1)}_\alpha = r_{ij,\alpha}/r_{ij}$ and $S^{(2)}_{\alpha\beta} = 3r_{ij,\alpha}r_{ij,\beta}/r^2_{ij} - \delta_{\alpha\beta}$ are interaction tensors. The last summations include the self-energy terms, representing the energy required to deform the anion charge density, with β, ζ and η as effective force constants. The extent of each ion's distortion is determined at each molecular dynamics time-step by energy minimization.

The polarization part of the potential incorporates dipolar and quadrupolar contributions [104],

$$\begin{aligned} V^{pol} &= \sum_{i,j\in O} \Bigg((q^i\mu^j_\alpha - q^j\mu^i_\alpha)T^{(1)}_\alpha + (\frac{q^i\theta^j_{\alpha\beta}}{3} + \frac{\theta^i_{\alpha\beta}q^j}{3} - \mu^i_\alpha\mu^j_\beta)T^{(2)}_{\alpha\beta} \\ &\quad + (\frac{\mu^i_\alpha\theta^j_{\beta\gamma}}{3} + \frac{\theta^i_{\alpha\beta}\mu^j_\gamma}{3})T^{(3)}_{\alpha\beta\gamma} + \frac{\theta^i_{\alpha\beta}\theta^j_{\gamma\delta}}{9}T^{(4)}_{\alpha\beta\gamma\delta}) \Bigg) \\ &+ \sum_{i\in O, j\in Mg,Si} \left(q^j\mu^i_\alpha[1 - g_D(r^{ij})]T^{(1)}_\alpha + \frac{\theta^i_{\alpha\beta}q^j}{3}[1 - g_Q(r^{ij})]T^{(2)}_{\alpha\beta} \right) \\ &+ \sum_{i\in O} \left(k_1 \mid \vec{\mu}^i \mid^2 + k_2\mu^i_\alpha\theta^i_{\alpha\beta}\mu^i_\beta + k_3\theta^i_{\alpha\beta}\theta^i_{\alpha\beta} + k_4 \mid \vec{\mu}^i \cdot \vec{\mu}^i \mid^2 \right). \end{aligned} \tag{1.16}$$

Here $k_1 = \frac{1}{2\alpha}$, $k_2 = \frac{B}{4\alpha^2 C}$, $k_3 = \frac{1}{6C}$, $k_4 = \frac{-B^2}{16\alpha^4 C}$, α, B and C the dipole, dipole-dipole-quadrupole and quadrupole polarizabilities of the oxygen ion, respectively, and $T_{\alpha\beta\gamma\delta} = \nabla_\alpha\nabla_\beta\nabla_\gamma\nabla_\delta ... \frac{1}{r_{ij}}$ are the multipole interaction tensors [105]. The instantaneous values of these moments are obtained by minimization this expression. The charge-dipole and charge-quadrupole cation-anion asymptotic functions include terms which account for penetration effects at short-range by using Tang-Toennies damping functions [106] of the form,

$$g_D(r^{ij}) = c_D e^{-b_D r^{ij}} \sum_{k=0}^{4} \frac{(b_D r^{ij})^k}{k!}, \tag{1.17}$$

$$g_Q(r^{ij}) = c_Q e^{-b_Q r^{ij}} \sum_{k=0}^{6} \frac{(b_Q r^{ij})^k}{k!}, \tag{1.18}$$

with D and Q standing for dipolar and quadrupolar parts. While the parameters b_D and b_Q determine the range at which the overlap of the charge densities affects the induced multipoles, the parameters c_D and c_Q determine the strength of the ion response to this effect. Only oxygen ions are considered polarizable.

The AIM potential takes into consideration the compression of the electron densities of the anions by the Madelung potential and overlap-mediated interactions with their coordination shell, as well as the polarization effects arising from the large interionic coulomb fields, which are importance of the many-body effects in ionic systems [40, 107, 108]. The parameters of AIM potential are fitted to reproduce forces, dipoles, quadrupoles and the stress tensor of reference atomis configurations calculated from first-principles, that is, without the help of any experimental input [39, 40, 103]. The AIM potential is transferable not only for different coordination environments [110, 111] but also for different temperature and pressure conditions [42, 103, 109].

1.2.3 Hamiltonian formulations

First-principles approaches to the modeling of phase equilibria rely on the integration of accurate quantum-mechanical total-energy calculations and statistical-mechanical modeling. This requires an efficient way to examine many different configurations in a system. Phase stability at constant temperature is determined by the free energy [1] F. The free energy can be expressed as a sum of a configurational contribution F_{conf} and vibrational contributions F_{vib}. The configurational contribution accounts for the fact that atoms can jump from one lattice site to another, while the vibrational contribution accounts for the vibrations of each atom around its equilibrium position. Depending on the material studied, contributions from magnetic effects F_{mag} and electronic effects F_{elec} can be significant. In this work we have considered only configurational and vibrational contributions to the free energy.

Configurational contribution to free energy

The configurational contribution to free energy of an alloy can, in principle, be computed as accurately as desired through a techique known as the *cluster expansion* [112–116]. The cluster expansion is a generalization of the well-known Ising Hamiltonian. In the common case of a binary alloy system, the Ising model consists of assigning a spinlike occupation variable to each site i of the parent lattice, which takes the value -1 or $+1$ depending on the type of atom occupying the site. A particular arrangement of spins of the parent lattice is called a *configuration* and can be represented by a vector $\vec{\sigma}$ containing the value of occupation variable for each site in the parent lattice.

[1] Striclty speaking, at constant pressure, the Gibbs free energy $G = F + PV$ should be used instead of the Helmotz free energy F, but at atmospheric pressure, the PV term is negligible for an alloy.

The energy (per atom) is represented as a polynomial in the occupation variables:

$$E(\sigma) = \sum_{\alpha} m_{\alpha} J_{\alpha} \langle \prod_{i \in \beta} \sigma_i \rangle, \tag{1.19}$$

where α is a cluster (a set of sites i). The sum is taken over all clusters α that are not equivalent by a symmetry operation of the space group of the parent lattice, while the average is taken over all clusters β that are equivalent to α by symmetry. The coefficients J_{α} are called effective cluster interaction (ECI), and the multiplicity of a cluster, m_{α}, is the number of symmetrically equivalent clusters, divided by the number of lattice sites.

It can be shown that when all clusters α are considered in the sum, the cluster expansion is able to represent any function $E(\sigma)$ of configuration σ by an appropriate selection of the values of J_{α}. However, the real advantage of the cluster expansion is that, in practice, it is found to converge rapidly. An accuracy that is sufficient for phase diagram calculations can be achieved by keeping only clusters α which are relatively compact (e.g. short-range pairs or small triplets). The unknown parameters ECI's can then be determined by fitting them to the energy of a relatively small number of configurations obtained through first-principle calculations using cross-validation (CV) score [117] which is defined as

$$CV = \frac{1}{N} \sum_{i=1}^{N} (E_i - \hat{E}_i)^2. \tag{1.20}$$

E_i is the calculated energy of structure i, whereas $\hat{E}_i$ is the predicted value of the energy of structure i obtained from a least-squares fit to the $(N-1)$ other structural energies. This fitting approach is known as the structure inverse method or Connolly-Williams method [118]. The advantage of CV score is that the chosen set of clusters maximizes the predictive power of the cluster expansion for any structure, whether or not it is included in the fit. This is an improvement relative to the standard mean square error criterion which only minimizes the error for structures that are included in the fit.

Vibrational contribution to free energy

The quantum treatment of lattice vibrations in the harmonic approximation provides a reliable description of thermal vibrations in many solids for low to moderately high temperatures [119]. Under the harmonic approximation [119, 120] and in the high temperature limit (also known as the classical limit), the vibrational energy of a phase α can be obtained from equipartition theorem, and is independent of the phase α considered. Hence, lattice vibrations are mainly expected to influence phase stability through their entropy contribution. Under these assumptions, the vibrational entropy per atom can be obtained from the phonon density of states (DOS), $g(\omega)$ [119]:

$$S_{vib} = -k_B \int_0^{\infty} g(\omega) ln(\omega) d\omega. \tag{1.21}$$

In lattice dynamic theory [121], the phonon DOS can be determined from eigenvalues of dynamical matrix which is defined as a function of the force constant tensor $\phi(i, j)$.

This tensor relates the displacement $u(j)$ of atom j from its equilibrium position to the forces $f(i)$ acting on atom i as follows:

$$f(i) = -\phi(i,j)u(j). \tag{1.22}$$

In order to calculate the force constants, we can employ the supercell method [122–126]. The basic idea is to perturb an atom j away from its equilibrium position by an amount $u(j)$, calculate the force $f(i)$ acting on atom i using first-principles calculations, and then solve a set of linear equations $f(i) = -\phi(i,j)u(j)$ to yield the force constant tensor $\phi(i,j)$. This process has to be repeated for many configurations and also for large supercells, making the overall precedure computationally demanding. A way to alleviate this problem is to use the transferable force constant (TFC) approach [127–130]. In this approach, three assumptions are necessary:

1. Only the nearest neighbor interactions are considered (because the longer range force constants do not exhibit good transferability).

2. The bending stiffnesses b are averaged over various spatial directions (i.e., to obtain effective isotropic bending stiffnesses).

3. The off-diagonal terms in the bond stiffness tensor $\phi(i,j)$ are constrained to be zero.

Hence, the resulting bond stiffness tensor has only two independent terms, namely the stretching stiffness s and the isotropic bending stiffness b:

$$\phi(i,j) = \begin{pmatrix} b & 0 & 0 \\ 0 & b & 0 \\ 0 & 0 & s \end{pmatrix}.$$

This symmetrization ensures that the force constants never have a symmetry that is lower than the environment into which they are transferred. For this fact only nearest neighbor force constants for high symmetry are needed to calculate them as functions of bond lengths. The resulting bond stiffness versus bond length relationships are then used to predict force constants for all remaining superstructures, using the relaxed bond lengths and the chemical identities of bonds as predictors of their stiffnesses.

Configuration dependence of the vibrational free energy is parameterized with a cluster expansion, in a similar manner as the configurational free energy, except that the resulting ECI's ($J_\alpha(T)$) are now temperature-dependent.

The process of calculating the phase diagram of an alloy system can be summarized as follows. First, the energy of the alloy in a relatively small number of configurations is calculated through first-principles calculations. Next, the calculated energies (configurational and vibrational) are used to fit the unknown coefficients of the cluster expansion ($J_\alpha(T)$). Finally, with the help of this compact representation ($F(\sigma,T) = \sum_\alpha m_\alpha J_\alpha(T)\langle\prod_{i\in\beta}\sigma_i\rangle$), the energy of a large number of configurations is sampled, in order to determine the phase boundaries. This can be accomplished with either the Cluster Variation Method (CVM) [131, 132], the low-temperature expansion (LTE) [133], or Monte Carlo (MC) simulations [134]. In this work we have used MC in semi-grand-canonical ensemble, also known as the transmutation ensemble. In this ensemble, the energy and concentration of an alloy with a fixed total number of atoms are allowed to fluctuate while temperature and chemical potentials are externally imposed.

1.3 Scope of the thesis

In the current thesis we have picked two avenues of research, partly motivated by the scientific questions at hand, partly to explore methodological approaches, understand and gain experience in the method.

In the first project (chapter 2) we compute from first-principles the phase diagram of TiC-ZrC, TiC-HfC, and ZrC-HfC solid solutions at ambient pressure. We chose this project in order to explore the possibilities of the cluster expansion approach to solid-solution computations in a chemically and crystallographically simple, nevertheless technologically important, system and gain experience in using the method as implemented in the ATAT package [117, 135, 136]. We were particularly interested in the application and limits of the transferable force constant model [127–130] as implemented in ATAT.

Similar to NaCl-KCl [137] the carbide systems have the advantage that experimental data on solubility limits are available [138–140] which allowed us to compare and explore the computational phase diagram both in terms of consolute points and shape in detail.

The second project deals with large scale molecular dynamics simulations of thermodynamic (chapter 3) and transport properties (chapter 4) in Mg_2SiO_4 melt. This project had the scientific motivation to explore and understand the experimental finding of anomalous viscosity behavior in depolymerized melts between 10-15 GPa [25, 26], as well as obtaining viscosity values for higher pressures to better constrain magma ocean structure in the early Earth. After exploring various approaches we realized transport properties could not be computed with sufficient precision with density functional theory methods. Not wanting to use classical potential because of potentially poor transferability, we decided to apply the flexible potential method [39, 40] in the melt simulations, which promised a decent compromise in transferability [41] and efficiency. With this method we were able to run molecular dynamic simulations for more than 100 picoseconds (1 fs timestep) and use cells with $\sim$ 2000 atoms.

Chapters 2-4 are based on the following manuscripts:

Chapter 2:
O. Adjaoud, G. Steinle-Neumann, B.P. Burton, and A. van de Walle, (2009) First-principles phase diagram calculations for the HfC-TiC, ZrC-TiC and HfC-ZrC solid solutions, Phys. Rev. B (to be submitted).

Chapter 3:
O. Adjaoud, G. Steinle-Neumann, and J. Sandro, (2008) Mg_2SiO_4 Liquid under High Pressure from Molecular Dynamics, Chem. Geol., **256**, 185-192.

Chapter 4:
O. Adjaoud, G. Steinle-Neumann, and J. Sandro, (2009) Transport properties of Mg_2SiO_4 melt at high pressure: Viscosity of the magma ocean, Geophy. Res. Lett. (to be submitted).

Bibliography

[1] E. J. Garnero, Annu. Rev. Earth Planet. Sci. **28**, 509537 (2000).

[2] M. Murakami , Hirose K., Kawamura K., Sata N. and Ohishi Y., Science **304**, 855858 (2004).

[3] A. R. Oganov and S. Ono, Nature **430**, 445-448 (2004).

[4] S.-H. Shim, T. S. Duffy, R. Jeanloz, and G. Shen, Geophys. Res. Lett. **31**, L10603 (2004).

[5] D. J. Stevenson, Formation and early evolution of the Earth, in Mantle Convection: Plate Tectonics and Global Dynamics, edited by W. R. Peltier, pp. 817873, Gordon and Breach, New York, 1989.

[6] V. S. Solomatov, Fluid dynamics of a terrestrial magma ocean, in Origin of the Earth and Moon, edited by R. M. Canup and K. Righter, pp. 323338, U. of Arizona Press, Tucson, 2000.

[7] Y. Abe, Phys. Earth Planet. Inter. **100**, 27-39 (1997).

[8] V. S. Solomatov, D. J. Stevenson, J. Geophys. Res. **98**, 5407-5418 (1993).

[9] V. S. Solomatov, D.J., Stevenson, J. Geophys. Res. **98**, 5375-5390.

[10] Q. Williams , J. Revenaugh and and E. Garnero, Science **281**, 546549 (1998).

[11] T. Lay, E. J. Garnero, and Q. Williams, Phys. Earth Planet. Inter. **146**, 441-461 (2004).

[12] J. Revenaugh and S. A. Sipkin, Nature **369**, 474-476 (1994).

[13] T. R. A. Song, D. V. Helmberger and S. P. Grand, Nature **427**, 530-533 (2004).

[14] K. N. Matsukage, Z. C. Jing, and S. Karato, Nature **438**, 488-491 (2005).

[15] J. A. Tangemann, B. L. Phyllips, A. Navrotsky, J. K. R. Weber, A .D. Hixson, T. A. Key, Geophys. Res. Lett. **28**, 2517-2520 (2001).

[16] R. A. Lange, I. S. E. Carmichael, Geochim. Cosmochim. Acta **51**, 2931-2946 (1987).

[17] S. M. Rigden, T. J. Ahrens, E. M. Stolper, J. Geophys. Res. **94**, 9508-9522 (1989).

[18] J. F. Stebbins, I. S. E. Carmichael, L. K. Moret, Contrib. Mineral. Petrol. **86**, 131-148 (1984).

[19] R. Lange, A. Navrotsky, Contrib. Mineral. Petrol. **110**, 311-320 (1992).

[20] Y. Bottinga, Earth. Plant. Sci. Lett. **74**, 350-360 (1985).

[21] M. L. Rivers, I. S. E. Carmichael, J. Geophys. Res. **92**, 9247-9270 (1987).

[22] G. Urbain, Y. Bottinga, P. Richet, Geochim. Cosmochim. Acta **46**, 1061-1072 (1982).

[23] J. O'M Bockris and D. L. Lowe, J. Sci. instr. **30**, 403-405 (1953).

[24] I. Kushiro, Year B.-Carnegie Inst. Wash. **77** , 675-678. (1978).

[25] J. E. Reid, A. Suzuki, K. Funakoshi, H. Terasaki, H., B. T. Poe, D. C. Rubie, E. Ohtani, Phys. Earth Planet. Inter. **139**, 45-54 (2003).

[26] C. Liebske, B. Schmickler, H. Terasaki, B. T. Poe, A. Suzuki, K. Funakoshi, R. Ando, D. C. Rubie, D.C., Earth Planet. Sci. Lett. **240**, 589-604 (2005).

[27] E. Ohtani, M. Kumazawa, Phys. Earth Planet. Inter. **27**, 32-38 (1981).

[28] T. Dunn, The piston-cylinder apparatus, in: Luth, R.W. (ed): Experiments at High Pressure and Applications to the Earth's Mantle, MAC short course handbook, Vol.21. Mineralogical association of Canada, (1993) p. 39-94.

[29] J. Graham, The multianvil press. In Sammis, C.G and Henvey, T.L. (eds.), Geophysics Part A, Laboratory Measurements, Methods of experimental physics. Academic Press, Orlando (1987).

[30] A. Jayaraman, Diamond Anvil Cell and High-Pressure Physical Investigations, Reviews of Modern Physics **55**, 65-108 (1983).

[31] T. J. Ahrens, Shock wave techniques for geophysics and planetary physics. In Methods of Experimental Physics, C. G. Sammis and T. L. Henyey eds., Academic Press **24 A**, 185-235 (1987).

[32] D. J. Lacks, D. B. Rear, J. A. Van Orman, Geochim. Cosmochim. Acta **71**, 1312 (2007).

[33] B. Guillot, N. Sator, Geochim. Cosmochim. Acta **71**, 1249 (2007).

[34] B. Guillot, N. Sator, Geochim. Cosmochim. Acta **71**, 4538 (2007).

[35] B. B. Karki, L. Stixrude, S. J. Clark, M. C. Warren, G. J. Ackland, and J. Crain, Am. Mineral. **82**, 635 (1997).

[36] A. R. Oganov, J. P. Brodholta, and G. D. Pricea, Earth Planet. Sci. Lett. **184**, 555 (2001).

[37] L. Stixrude, B. Karki, Science **310**, 297 (2005).

[38] N. P. de Koker, L. Stixrude, B. B. Karki, B.B., Geochim. Cosmochim. Acta **72**, 1427 (2008).

[39] A. Aguado, L. Bernasconi, S. Jahn, P. A. Madden, Faraday Discuss. **124**, 171 (2003).

[40] P. A. Madden, R. Heaton, A. Aguado, S. Jahn, J. Mol. Struct. (Theochem) **771**, 9 (2006).

[41] S. Jahn, Am. Mineral. **93**, 1486 (2008).

[42] O. Adjaoud, G. Steinle-Neumann, and S. Jahn, Chem. Geol., **256**, 185 (2008).

[43] L. Stixrude, R.E. Cohen, R. Yu and H. Krakauer, Am. Mineral. **81** 1293 (1996).

[44] S. Akber-Knutson, M. S. T. Bukowinski, and J. Matas, Geophys. Res. Lett. **29**, 1034 (2002).

[45] B. Magyari-Köpe, L. Vitos, G. Grimvall, B. Johansson, and J. Kolaar, Phys. Rev. B **65**, 193107 (2002).

[46] R. Caracas, R. M. Wentzcovitch, D. G. Price, and J. Brodholt, Geophys. Res. Lett. **32**, 06306 (2005).

[47] L. Li, D. J. Weidner, J. Brodholt , D. Alfé, G. D. Price, R. Caracas, and R. Wentzcovitch, Phys. Earth Planet. Inter **155**, 249 (2006).

[48] R. Caracas and R. Wentzcovitch, Acta Cryst. B **62**, 1025 (2006).

[49] D. Y. Jung, and A. R. Oganov, Phys. Chem. Miner. **32**, 146 (2005).

[50] S. Ono, Y. Ohishi, and K. Mibe, Am. Mineral. **89**, 1480 (2004).

[51] J. H. Nguyen and N C. Holmes, Nature 427, 339 (2004).

[52] X.Song, and D. V. Helmberger, Geophys. Res. Lett., **20** 285 (1993).

[53] A. K. Singh, H. K. Mao, J. Shu, and R. J. Hemley, Phys. Rev. Lett. 80, 2157 (1998).

[54] G. Steinle-Neumann, L. Stixrude, and R. E. Cohen, Phys. Rev. B **60**, 791 (1999).

[55] T.S. Duffy, G. Shen, D.L. Heinz, J. Shu, Y. Ma, H.K. Mao, R.J.. Hemley, and A.K. Singh, Phys. Rev. B **60**, 15063 (1999).

[56] H.-R. Wenk, S. Matthies, R. J. Hemley, H.-K. Mao, J. Shu, Nature **405**, 1044 (2000).

[57] P. Hohenberg and W. Kohn, Phys. Rev. **136**, B864-871 (1964).

[58] N. David Mermin, Phys. Rev. **137**, A1441-1443 (1965).

[59] W. Kohn and L. J. Sham, Phys. Rev. **140**, A1133-1138 (1965).

[60] D. C. Langreth and M. J. Mehl, Phys. Rev. Lett. **47**, 446 (1981).

[61] O. Gunnarsson and B. I. Lundqvist, Phys. Rev. B **13**, 4274 (1976).

[62] U. von Barth and L. Hedin, J. Phys. C: Solid State Phys. **5**, 1629 (1972).

[63] O. Gunnarsson, B. I. Lundqvist, and S. Lundqvist, Solid State Commun. **11**, 149 (1972).

[64] D. M. Ceperley and B. J. Alder, Phys. Rev. Lett. **45**, 566 (1980).

[65] S. H. Vosko, L. Wilk, and M. Nusair, Can. J. Phys. **58**, 1200 (1980).

[66] J. P. Perdew and A. Zunger, Phys. Rev. B **23**, 5048 (1981).

[67] J. P. Perdew and Y. Wang, Phys. Rev. B **45**, 13244 (1992).

[68] R. O. Jones and O. Gunnarsson, Rev. Mod. Phys. **61**, 689 (1989).

[69] S. Kurth, J. P. Perdew, and P. Blaha, Int. J. Quant. Chem. **75**, 889 (1999).

[70] V. L. Moruzzi, J. F. Janak, and A. R. Williams, Calculated Electronic Properties of Metals (Pergamon, New York, 1978).

[71] J. Häglund, G. Grimvall, T. Jarlborg, and A. Fernández Guillermet, Phys. Rev. B **43**, 14400 (1991).

[72] J. Häglund, G. Grimvall, and T. Jarlborg, Phys. Rev. B **44**, 2914 (1991).

[73] A. Fernández Guillermet, J. Häglund, and G. Grimvall, Phys. Rev. B **45**, 11557 (1992).

[74] A. Fernández Guillermet, J. Häglund, and G. Grimvall, Phys. Rev. B **48**, 11673 (1993).

[75] C. S. Wang, B. M. Klein, and H. Krakauer, Phys. Rev. Lett. **54**, 1852 (1985).

[76] J. P. Perdew, J. A. Chevary, S. H. Vosko, K. A. Jackson, M. A. Pederson, D. J. Singh, and C. Fiolhais, Phys. Rev. B **46**, 6671 (1992).

[77] J. P. Perdew, K. Burke, and M. Ernzerhof, Phys. Rev. Lett. **77**, 3865 (1996).

[78] Y. M. Juan and E. Kaxiras, Phys. Rev. B **48**, 14944 (1993).

[79] M. C., Payne, M. P., Teter, D. C., Allan, T. A. Arias, J. D. Joannopoulos, Rev. Mod. Phys. **64**, 1045 (1992).

[80] J. Junqueira, O. Paz, D. SanchezPortal, E. Artacho, Phys. Rev.B **64**, 235111 (2001).

[81] J. M. Soler, E. Artacho, J. D. Gale, A. Garcia, J. Junquera, P. Ordejon, D. Sanchez-Portal, J. Phys. Cond. Matter. **14** 2745 (2002).

[82] N. Troullier, J. L. Martins, Phys. Rev. B **43**, 1993 (1991).

[83] D. Singh, Plane waves, pseudopotentials and the LAPW method, Kluwer Academic Publishers Boston, 1994, and references therein.

[84] W. E. Pickett, Comput. Phys. Rep. **9**, 115 (1989).

[85] I. Grinberg, N. J. Ramer, and A. M. Rappe, Phys. Rev. B **63**, 201102 (2001).

[86] D. Porezag, M. R. Pederson, and A. Y. Liu, Phys. Rev. B **60**, 14132 (1999).

[87] L. Li, D.J. Weidner, J. Brodholt, D. Alfe, G.D. Price, R. Caracas and R. Wentzcovitch, Phys. Earth Planet. Int. **155** 249 (2006).

[88] L. Li, D.J. Weidner, J. Brodholt, D. Alfe, D.G. Price, R. Caracas and R. Wentzcovitch, Phys. Earth Planet. Int. **155** 260 (2006).

[89] F. Zhang and A.R. Oganov, Earth Planet. Sci. Lett. **248**, 54 (2006).

[90] M. Matsui, Phys. Earth Planet. Int. **116**, 9 (1999).

[91] M. Matsui, Phys. Earth Planet. Int. **121**, 77 (2000).

[92] M. Blanchard, K. Wright and J.D. Gale, Phys. Chem. Miner. **32** 332 (2005).

[93] S. Tsuneyuki, M. Tsukada, H. Aoki and Y. Matsui, Phys. Rev. Lett. **61** 869 (1988).

[94] B. W. H. van Beest, G.J. Kramer and R.A. van Santen, Phys. Rev. Lett. **64** 1955 (1990).

[95] P. Tangney and S. Scandolo, J. Chem. Phys. **117** 8898 (2002).

[96] C. R. A. Catlow, C. M. Freeman, M. S. Islam, R. A. Jackson, M. Leslie, and S. M. Tomlinson, Phil. Mag. A **58**, 123(1988).

[97] D. Frenkel and B. Smit, Understanding Molecular Simulation. Academic Press (2001).

[98] S. Jahn, P. A. Madden, J. Non-Cryst. Solids **353**, 3500 (2007).

[99] M. Wilson, P. A. Madden, N. C. Pyper, and J. H. Harding, J. Chem. Phys. **104**, 8068 (1996).

[100] A. Rowley, P. Jemmer, M. Wilson, and P. A. Madden, J. Chem. Phys. **108**, 10209 (1998).

[101] P. Tangney and S. Scandolo, J. Chem. Phys. **119**, 9673 (2003).

[102] A. Aguado, P. A. Madden, Phys. Rev. Lett. **94**, 68501 (2005).

[103] S. Jahn, P. A. Madden, Phys. Earth Planet. Inter. **162**, 129 (2007).

[104] M. Wilson, P. A. Madden, B. J. Costa-Cabral, J. Phys. Chem. **100**, 1227 (1996).

[105] Stone, A.J., 1996. The theory of intermolecular forces. Oxford University Press, Oxford.

[106] K. T. Tang, J. P. Toennies J. P., J. Chem. Phys. **80**, 3726 (1984).

[107] P. A. Madden, M. Wilson, Chem. Soc. Rev. **25**, 339 (1996).

[108] P. A. Madden, M. Wilson, J. Phys. Condens. Matt. **12**, A95 (2000).

[109] A. Aguado and P.A. Madden, Phys. Rev. B **70**, 245103 (2004).

[110] S. Jahn, P.A. Madden and M. Wilson, Phys. Rev. B **69** 020106 (2004).

[111] S. Jahn, P.A. Madden and M. Wilson, Phys. Rev. B **74** 024112 (2006).

[112] J. M. Sanchez, F. Ducastelle, and D. Gratias, Physica A **128**, 334 (1984).

[113] D. de Fontaine, Solid State Phys. **47**, 33 (1994).

[114] A. Zunger In: P. E. Turchi, and A. Finel, editors. Statics and dynamics of alloy phase transformations. NATO ASI Series. New York: Plenum Press; 1994.

[115] G. L. W. Hart, v. Blum, M. J. Walorski, and A. Zunger A., Nat. Mater. **4**, 391 (2005).

[116] A. van de Walle, G. Ghosh, and M. Asta, *Ab initio* modeling of alloy phase stability. In: G. Bozzolo, R. D. Noebe, and P. Abel, editors. Applied computational materials modeling: theory, simulation and experiment. New York: Springer; p. 1-34 (2007).

[117] A. van de Walle and G. Ceder, J. Phase Equilib. **23**, 348 (2002).

[118] J. W. Connolly and A. R. Williams, Phys. Rev. B, **27**, 5169 (1983).

[119] A. A. Maradudin, E. W. Montroll, and G. H. Weiss, Theory of Lattice Dynamics in the Harmonic Approximation, 2nd edn., Academic Press, New York, 1971.

[120] W. Ashcroft and N. D. Mermin, Solid State Physics, Holt Rinehart and Winston, New York, 1976.

[121] M. T. Dove, Introduction to Lattice Dynamics, Combridge University Press, 1993.

[122] A. Zunger, S.-H. Wei, L.G. Ferreira, and J. E. Bernard, Phys. Rev. Lett. **65**, 353 (1990).

[123] K. A. Mäder and A. Zunger, Phys. Rev. B, **51**, 10462 (1995)

[124] I. A. Abrikosov, S. I. Simak, B. Johansson, A. V. Ruban, and H. L. Skriver, Phys Rev B **56**, 9319 (1997).

[125] C. Jiang, C. Wolverton, J. Sofo, L. Q. Chen, and Z.-K. Liu, Phys Rev B **69**, 214202 (2004).

[126] D. Shin, A. van de Walle, Y. Wang, and Z.-K. Liu, Phys Rev B, **76**, 144204 (2007).

[127] A. van de Walle and G. Ceder, Phys. Rev. B **61**, 5972 (2000).

[128] A. van de Walle, Ph.D. thesis, Massachusetts Institute of Technology, Cambridge, 2000.

[129] A. van de Walle and G. Ceder, Rev. Mod. Phys. **74**, 11 (2002).

[130] E. J. Wu, G. Ceder, and A. van de Walle, Phys. Rev. B **67**, 134103 2003.

[131] R. Kikuchi. Phys. Rev. **81**, 988 (1951).

[132] F. Ducastelle. Order and Phase Stability in Alloys. Elsevier Science, New York, 1991.

[133] A. F. Kohan, P. D. Tepesch, G. Ceder, C. Wolverton, Comp. Mat. Sci. **9**, 389 (1998).

[134] K. Binder, D. W. Heermann, Monte Carlo Simulation in Statistical Physics, Springer-Verlag, New York, 1988.

[135] A. van de Walle, M. Asta, and G. Ceder. CALPHAD J. **26**, 539 (2002).

[136] A. van de Walle and M. Asta, Modelling Simul. Mater. Sci. Eng. **10**, 521 (2002).

[137] B.P. Burton and A. van de Walle, Chem. Geol. **225**, 222 (2006).

[138] R. Kieffer, H. Nowotny, A. Neclcel, P. Ettmayer, and L. Usner, Montsh. Chem. **99**, 1020 (1968); R. Kieffer and P. Ettmayer, Angew. Chem. internat. Edit — Vol. 9 (1970) — No. 12.

[139] P. Rogl, S. K. Naik, and E. Rudy, Monatshefte für Chemie **108**, 1189 (1997).

[140] A.E. Kowalskii, E. Ya Vrzheshch, in: S.J. Bashkirov (Ed.), Hard Metals Production Technology and Research in the USSR, Pergamon Press, 1964.

Chapter 2

Phase diagram calculations for the (M,M')C solid solutions

2.1 Abstract

We have performed first-principles phase diagram calculations for the quasibinary systems HfC-TiC, TiC-ZrC and HfC-ZrC. We have used a plane-wave pseudopotential method to compute formation energies which serve as a basis for fitting cluster expansion Hamiltonians, both with and without an approximation for excess vibrational entropy. Significant miscibility gaps are predicted for the quasibinaries TiC-ZrC and HfC-TiC, with consolute temperature in excess of 2000 K. The system HfC-ZrC shows complete miscibility at room temperature. We have found an approximately symmetric phase diagram for HfC-TiC and asymmetric phase diagrams for HfC-ZrC and TiC-ZrC.

2.2 Introduction

The transition metal carbides, including the group IV (Ti, Zr, Hf) carbides have extremely high melting points and are therefore referred to collectively as the "refractory carbides." In addition to their stability at high temperatures, these compounds exhibit interesting physical properties such as high hardness, high electrical conductivity and superconductivity [1]. These properties make them suitable as bulk or thin film materials in many technological applications: they are used as first-wall coatings for fusion reactors, protective coatings for cutting tools, and low-friction coatings for bearings. Their hardness is retained to very high temperatures, and they have low chemical reactivity. They are attacked only by concentrated acid or base in the presence of oxidizing agents at room temperature, and retain good corrosion resistance to high temperatures. The transition metal carbides have been explored for their potential application as diffusion barrier in electronic devices, too [2]. Aside from the pure end members the solid solutions formed by these carbides are of significant importance as properties can be optimized by varying the composition in the binary - and higher order - systems.

Systematic experimental investigations of the phase diagrams and physical properties of such nonstoichiometric compounds are extremely challenging as many compositions need to be explored, and due to the high melting points and limited solubility for the

refractory carbide make it very difficult to look at their miscibility behavior in detail, although experiments have been performed [3–5].

At the same time, calculations make it possible to establish the shape of the phase diagram to a sufficient degree of accuracy if the interactions in the system as a function of temperature and composition are known. Several semiempirical methods exist to construct phase diagrams based on approximate free energy functions such as the model of subregular solutions [6–8] fitted to existing experimental data. Such thermodynamic models have also been applied to the group IV carbides [9–11].

Although these methods are useful to obtain phase diagrams and thermodynamic functions it is desirable to compute them strictly from knowledge of the constituent atoms without empirical parameters. In order to calculate phase equilibria the Gibbs free energy must be known for competing structures over a wide range of concentrations. The energies of formation for a large number of phases over a range of stoichiometries need to be determined. At present, the three most widely employed approaches for this purpose can be summerized as follows. The most direct approach is the supercell method (e.g.[12–16]), which is commonly employed to analyze local atomic structures and variations in bond lengths with chemical composition. The supercell method is based on the principle of spatial ergodicity, according to which all possible finite atomic arrangements are realized in a single infinite sample. This approach is computationally prohibitive when the size of the supercell is on the order of hundreds of atoms. In contrast to the supercell approach, methods based on perturbation theory perform the configurational average analytically. The most well-known approximation within alloy theory is the so-called coherent potential approximation (CPA) (e.g.[17–19]). Recently it has also been demonstrated how short-range order effects can be incorporated in total energy calculations using a nonlocal modification of the CPA [19]. Within the CPA-based methods no self-consistent calculation of elastic relaxation energies has been demonstrated to date, and such effects are generally treated using separate theoretical frameworks [20–22]. A third option is to apply the cluster expansion (CE) approach [23–27]; this approach allows incorporating contributions to solid-solution energies arising from short-range order as well as elastic relaxations. In the CE method effective cluster interactions are fit to an extensive set of formation energies of supercells in the binary system which is then explored to compute the compute the phase diagram from Monte Carlo simulations. This approach is implemented in the alloy theoretic automated toolkit (ATAT) code [28–30]. This code was used to study phase stabilities of intermetallics, alloys, and pseudobinary systems: e.g. [31–36].

In this study, we explore by means of the CE method the sub-solidus phase diagram of the binary refractory carbide solid solutions HfC-TiC, ZrC-TiC and HfC-ZrC, by combining the ATAT package with *ab initio* total energy calculations. We look in detail at the extent of miscibility between the phases and the consolute temperature and composition. As experimental data and thermodynamic assessments of these systems are available we compare predictions from the computations to measurements.

2.3 Methodology

Formation energies, ΔE_f (Figs. 2.1) were calculated for transition metal carbides HfC, TiC, and ZrC and many $M_mM'_nC_{(m+n)}$ supercells, in which M and M′ are Hf, Ti, or Zr. All electronic structure calculations were performed with the Vienna *ab initio* simulation program (VASP,[37]) using ultrasoft Vanderbilt-type pseudopotentials [38] with the generalized gradient approximation (GGA) for exchange and correlation [39]. Valence electron configurations for the pseudopotentials are Hf = $5p^66s^25d^2$, Ti = $3d^34s^1$, Zr = $4s^24p^65s^24d^2$, and C = $2s^22p^2$. Total energy calculations were converged with respect to k-point sampling, and an energy cutoff of 500 eV was used which yields ΔE_f values that are converged to within a few meV per cation (Hf, Ti, Zr). Cell constant and ionic positions were fully relaxed in all supercell computations.

Based on these results the first-principles phase diagram (FPPD) calculations were performed with the ATAT software package [28–30]. VASP calculations were used to construct CE Hamiltonians [23], and the optimal cluster sets were determined by minimizing the cross-validation score [28] between the *ab initio* computations and the CE prediction. The cross-validation score is analogous to a weighted root mean square error, and provides a quantitative measure of predictive power of the CE. The effective cluster interactions (ECIs) which define the CE are obtained by a least-square fit to the VASP energies.

Contributions of lattice vibrations (F_{vib}) to the free energies were approximated [40]: To reduce the computational burden of obtaining phonon densities of states for a large set of superstructures, the bond-length-dependent transferable force constant scheme [40] was employed: as discussed in Ref. [32], nearest-neighbor force constants were obtained for the end members HfC, TiC, and ZrC as functions of imposed lattice parameters that are relevant for the respective systems: in each system the lattice parameters are varied between the end-member equilibrium constants, and forces are computed for five-six volumes in-between. Depending on the variations in lattice constant this can lead to slightly different force constants for the same end-member, e.g. HfC in the TiC-HfC and the HfC-ZrC system.

The resulting bond stiffness versus bond length relationships were applied to predict force constants for all remaining superstructures, using the relaxed bond lengths and the chemical identities of bonds as predictors of their stiffnesses. The quantum mechanical expression for the free energy was used, rather than the typical high-temperature (classical) limit. Then the resulting free energies were fit to temperature-dependent CE, which served as input for grand-canonical Monte Carlo simulations in order to calculate phase diagrams.

2.4 Results and Discussion

Figure 2.1 shows the databases of static (0 K) formation energies from the *ab initio* computations, ΔE_f, that were used in fitting the cluster expansion Hamiltonians, and the corresponding formation energies predicted from the CEs. The formation energies of all the ordered structures studied in the three systems are positive (Fig. 2.1). This is consistent with the fact that the experimental phase diagrams show no ordered intermediate

compound [3, 4]. We further see large formation energies for both the HfC-TiC and TiC-ZrC systems (several 100 meV/cation) which are one order of magnitude larger than for the HfC-ZrC solid solution. This suggests extensive miscibility gaps with large consolute temperatures for these two systems (Fig. 2.1), as is the case for AlN-InN in previous work [33]. The formation energies in the HfC-ZrC are more in line with AlN-GaN in the same study and can be expected to lead to complete miscibility even at room temperature, consistent with experimental data.

The CEs were fitted with a moderate number of structures to obtain a good cross-validation score (Table 2.1): they consist mostly of pair interactions plus 1-2 triplet clusters (Table 2.1 and Fig. 2.2). The convergence of the effective cluster interactions (Fig. 2.2) is relatively fast: pair interactions of less than the 5th neighbor shell are required to obtain converged CEs. This is in contrast to studies in metal based solid solutions, e.g. Al-TM (TM = Ti, Zr and Hf) where interactions beyond the 10th neighbor shell are required [36], and a large number of many-body (triplet and four-body) clusters are needed. The ECIs show a general trend of decreasing in amplitude with distance (Fig. 2.2), as expected, except for a significant negative value at four times the nearest neighbor distance. Examining the crystal structure this corresponds to ordering of metal ions of the same type on second neighbor sites along the cell edges. As no ordered phases are found that are energetically stable this can be understood as an indication of phase separation in the carbide systems. For all three systems the resulting cross-validation score is significantly below 10 meV/atom which is considered an excellent value for the CE [28]. We have explored different expansions of the CEs and added additional structures to explore the ECI behavior at four times the nearest neighbor distance and found the feature to be robust.

The presence of three-body terms (Table 2.1) in the CE Hamiltonians for the three systems implies that the FPPD calculations yield asymmetric phase diagrams.

Fig. 2.3 shows the cluster expansions of volumes as functions of bulk composition. Trends for all three systems are close to linear, ideal solution, behavior with a fit for HfC-ZrC that is within computational error of ideal mixing (Vegard's law). A positive deviation from ideal behavior in HfC-TiC and TiC-ZrC is observed; the excess volume of mixing in these systems again implies immiscibility that would even increase if the system was pressurized. In contrast, immiscibility caused by a negative volume of mixing as computed for the wurtzite-structured nitrides [33] would result in a decrease of immiscibility under pressure.

The dependence of the stretching and bending force constants on bond length are shown in Fig. 2.4. The stretching force constants decrease monotonically with increasing bond length. The bending terms, by contrast, are relatively insensitive to changes in bond length. Furthermore, the Ti-C stretching and bending force constants in the systems HfC-TiC and TiC-ZrC are found to lie in the single curve. This explains the transferable force constants for the bond Ti-C between different chemical systems. This effect was also found in the Au-Cu, Au-Pd, and Cu-Pd systems by Wu *et al.* [41]. However, in the Al-TM systems, the Al-Al bond force constants exhibited differences amongst the three binary alloy sytems [35].

The phase diagrams of the binary systems are computed with and without vibrational free energy contributions (Fig. 2.5). As expected from the presence of three-body terms in

the ECIs (Table 2.1 and Fig. 2.2) the phase diagrams are asymmetric. The system HfC-TiC and TiC-ZrC show complete immiscibility below ~ 750 K and ~ 1000 K, respectively, consistent with experimental data [3, 4]. By contrast, the HfC-ZrC system is completely miscible at room temperature. In all cases the asymmetry in solubility is slightly shifted towards the side with the larger cation [42] (Fig. 2.6), i.e. ZrC in the systems HfC-ZrC and TiC-ZrC, and HfC in the system HfC-TiC. The consolute temperature (T_C) for the HfC-TiC and TiC-ZrC without F_{vib} are considerably higher than experimental estimates (Table 2.2), with consolute compositions (X_C) at 0.50 for HfC-TiC and TiC-ZrC, and 0.58 for HfC-ZrC.

Adding vibrational contributions to the free energy in the carbide solid solutions yields lower T_C in all three cases . Most significant changes occur in the TiC-ZrC system where T_C is lowered by 655 K ($\sim 19\%$) and the composition is shifted to the TiC side ($X_C = 0.59$) (Figs. 2.5 and 2.6, Table 2.2), with T_C still significantly larger than the experimental data [3]. As they are at least partially based on the experimental data thermodynamic assessments of the system [9–11] are in much better agreement with experiments.

In the HfC-TiC and HfC-ZrC systems T_C decreases by 155 K ($\sim 7\%$) and 10 K ($\sim 4\%$), respectively (Figs. 2.5 and 2.6, Table 2.2). After accounting for vibrational contributions the agreement with experimental data for HfC-TiC is excellent [3, 4] (Table 2.2). They also compare favorably with macroscopic thermodynamics [9–11] . In agreement with our computations the system HfC-ZrC shows complete miscibility at room temperature in the thermodynamic data [10] .

The consolute temperature can also be rationalized in terms of the difference between the ionic radii of the exchangeable cations $\%\Delta R_{ij} = 200|R_i - R_j|/(R_i + R_j)$ (Fig. 2.6): the positive correlation between $\%\Delta R_{ij}$ and T_C supports the notion that the immiscibility in these systems is caused by an ionic size effect. Similarly, the reduction of T_C due to vibrational free energy ($\%\Delta T_C$) correlates with $\%\Delta R_{ij}$ and hence with T_C as well: within these systems relative contributions to the free energy increase as T_C increases. This is in contrast to the to wurtzite-structured nitrides [33] where the reduction in T_C is anti-correlated to the $\%\Delta R_{ij}$.

Considerations of elastic energy in the binary systems provides an alternative way to assess the energetics of substituting cations in the solid solutions and rationalize the asymmetry of the phase diagrams. Here we compute the elastic energy by the $\epsilon - G$ approximation [43–46] for the three binary systems . This energy is calculated as follow: The equations of state (EoS) of end members HfC, TiC, and ZrC are computed, i.e. E(V) where the volume of the cell for the end members are varied and then transformed to $E(X)$ via the CE volumes (Fig. 2.3). Finally $\Delta E(X)$ is approximated by a linear combination of end member EoS (e.g. for HfC-TiC, $\Delta E(X) = (1 - X)E_{HfC}(X) + XE_{TiC}(X)$). The resulting $\Delta E(X)$ for HfC-ZrC is symmetric (Fig. 2.7), for HfC-TiC and TiC-ZrC $\Delta E(X)$ is asymmetric with mixima closer to the end member with the smaller ion [42] (Fig. 2.7). This implies that more energy is required to replace a smaller ion with a larger one than vice versa - and that the deviation from $X = 0.5$ is directly correlated with difference in ionic radius between the cations (Fig. 2.6). This is consistent with previous work on the wurtzite-structured nitrides [33] and the quasibinary system TiC-ZrC [46].

2.5 Conclusions

First principles phase diagram calculations for the quasibinary systems HfC-TiC, TiC-ZrC, and HfC-ZrC predict miscibility gaps with consolute temperatures, T_C = 2120 K, 2695 K, and 238 K, respectively. Miscibility gaps are predicted for all three quasibinaries with approximately symmetric phase diagram for HfC-TiC and asymmetric phase diagrams for HfC-ZrC and TiC-ZrC, consistent with thermodynamic assessments in these system. For the carbide binary solid solutions the degree of miscibility and T_C is directly related to differences in ionic radii of the exchangeable cations, with larger ions more readily replaced by smaller ones than vice a versa.

2.6 Acknowledgments

This work was in part funded by the Graduate School "Oxides" in the Elite Netzwerk Bayern, funded by the State of Bavaria and the collaboration between GSN and AvdW has been supported by the Bavaria California Technology Center (BaCaTeC). We greatly appreciate helpful discussion with Dan Frost and Nico de Koker.

2.7 Tables

Table 2.1: Characteristics of the calculated cluster expansions.

Characteristics	HfC-TiC	TiC-ZrC	HfC-ZrC
Number of structures	45	41	29
Number of clusters	2+11+1	2+10+1	2+11+2
Cross-Validation scores (meV/atom)	7.1	5.2	2.2

Table 2.2: Calculated consolute points.

System Method	Without F_{vib} $\{X_C, T_C(K)\}$	With F_{vib} $\{X_C, T_C(K)\}$	Method references
HfC-TiC	0.50, 2275	0.50, 2120	FPPD[1]
		0.55, 2133	Exp.[2]
		0.55, 2053	Exp.[3]
		0.60, 2173	SE[4]
		0.56, 2075	SR[5]
TiC-ZrC	0.50, 3350	0.41, 2695	FPPD[1]
		0.45, 2273	Exp.[2]
		0.45, 2373	SE[4]
		0.35, 2281	SR[5]
HfC-ZrC	0.58, 248	0.58, 238	FPPD[1]
		−, <300	SR[5]

[1] FPPD = First principles phase diagram, this work. [2] Experimental results from Kieffer *et al.* [3]. [3] Experimental results from Rogl *et al.* [4]. [4] SE = Combined CALPHAD modelling with experimental data and *ab initio* results from Markström *et al.* [9]. [5] SR = Subregular model from Gusev [10].

2.8 Figures

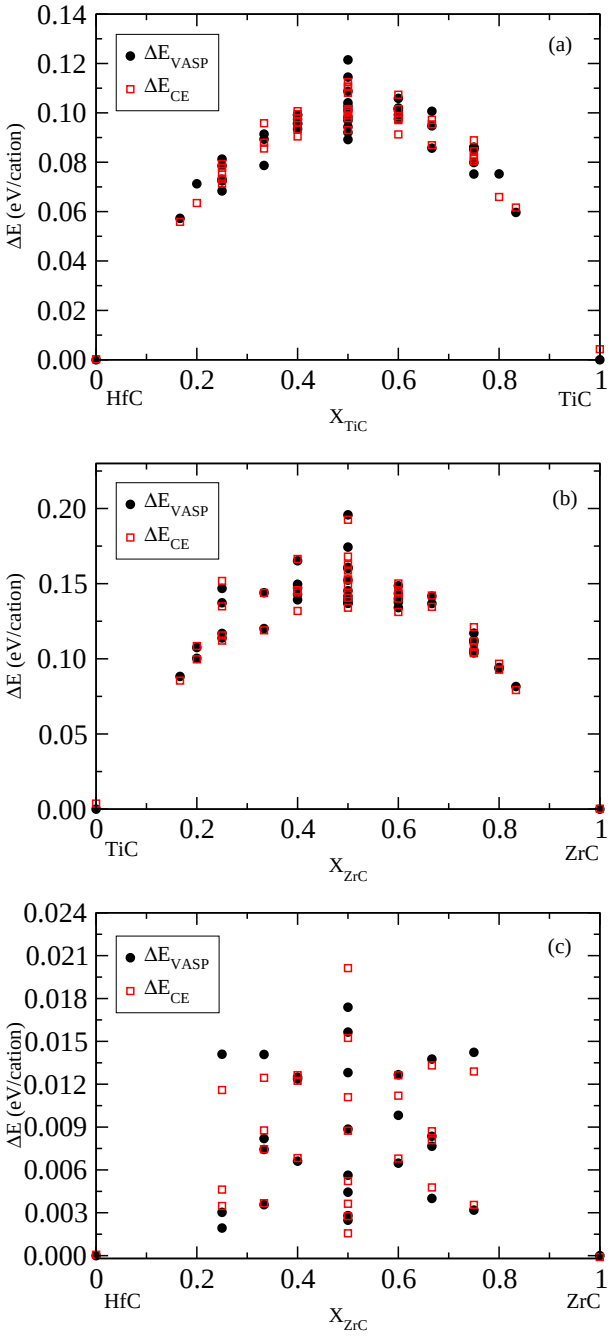

Figure 2.1: Formation energies, ΔE_f, for (a) $Hf_{1-x}Ti_xC$, (b) $Ti_{1-x}Zr_xC$, and (c) $Hf_{1-x}Zr_xC$ supercells. Closed circles are VASP results, and open squares are values calculated with cluster expansion Hamiltonians that were fit to VASP results.

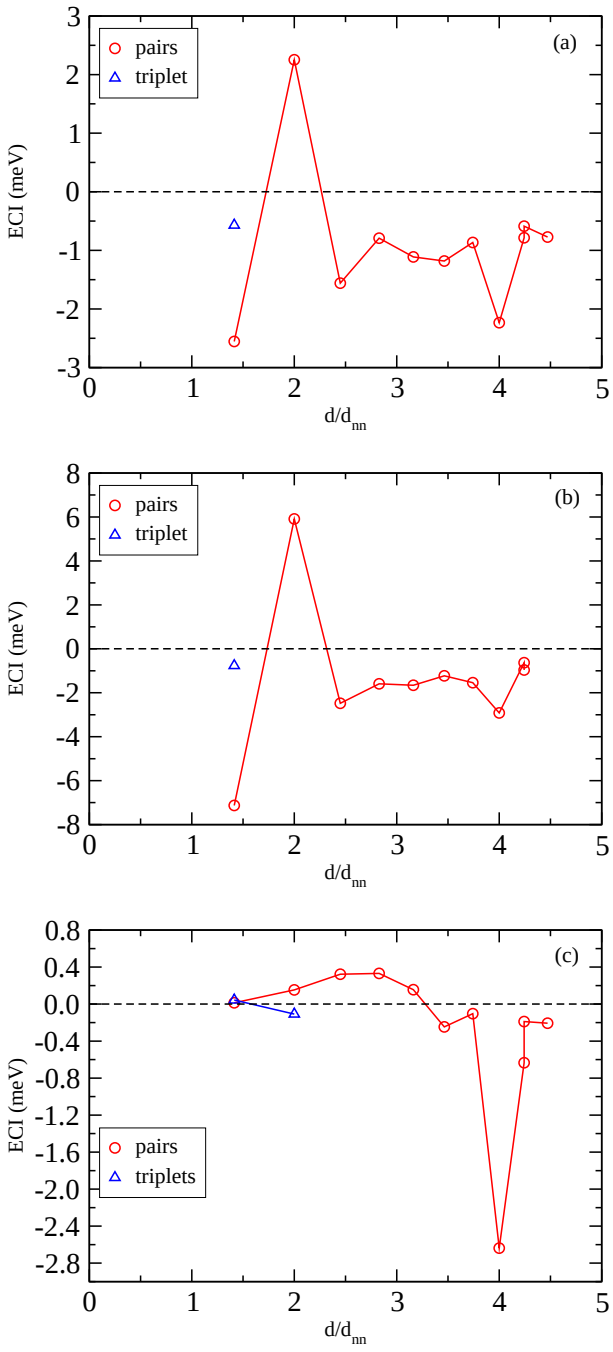

Figure 2.2: Calculated ECIs as functions of cluster diameter (normalized by nearest neighbor distance) in (a) HfC-TiC, (b) TiC-ZrC, and (c) HfC-ZrC sytems.

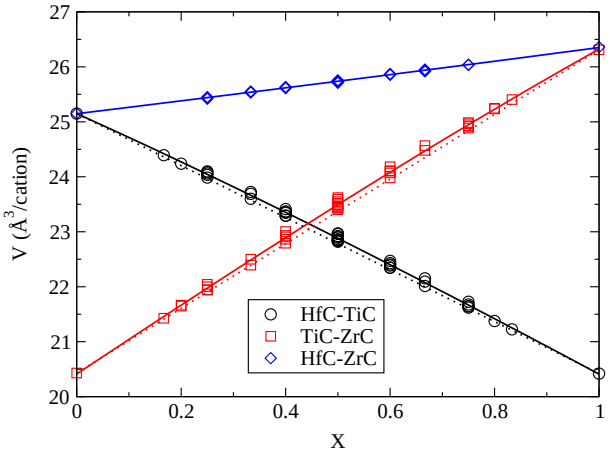

Figure 2.3: Cluster expansion fits (solid lines), and VASP supercell calculations (circles, squares, and diamands), of volume as functions of composition for the systems HfC-TiC, TiC-ZrC, and HfC-ZrC. The dashed lines connect end points for supercell calculations.

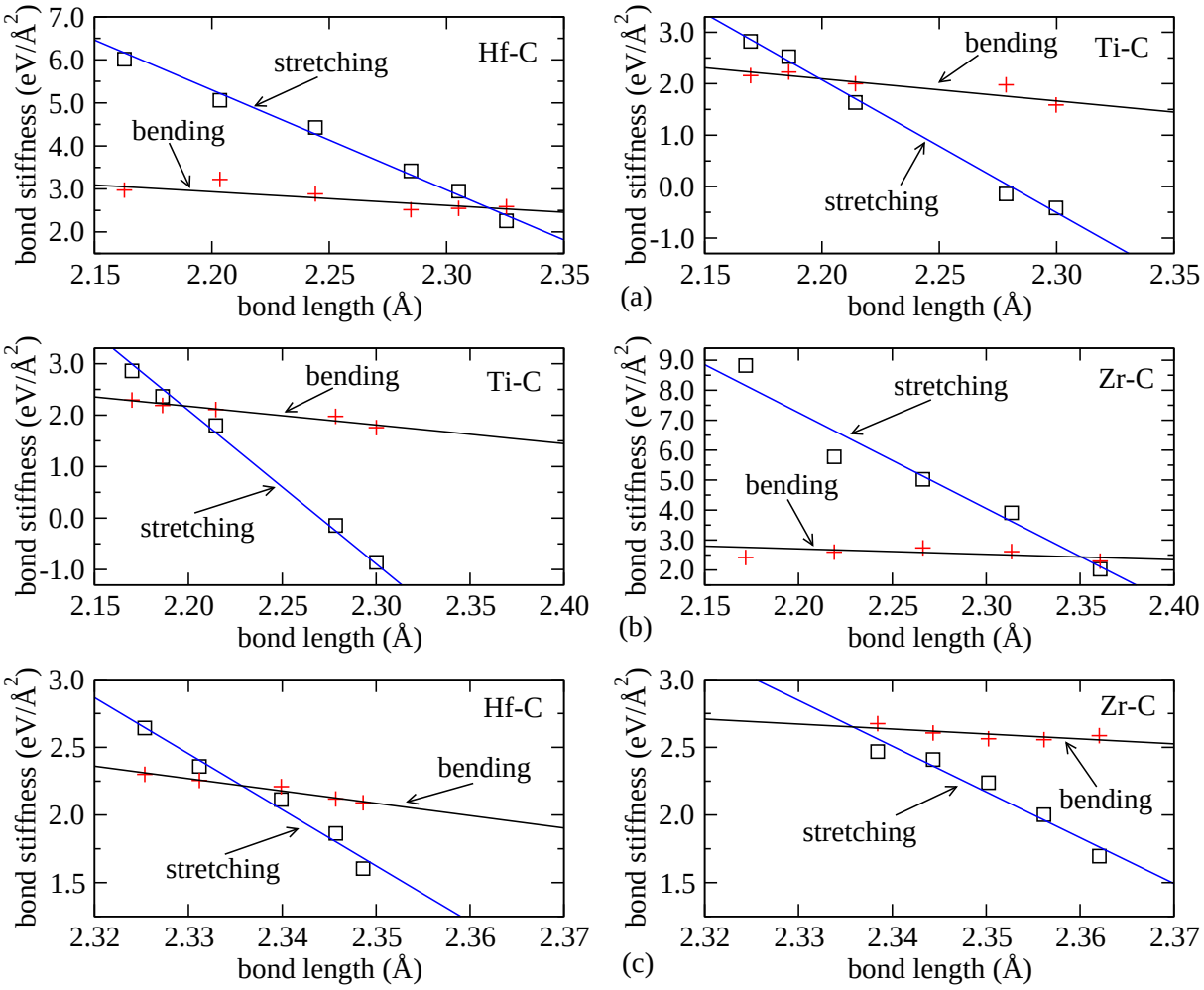

Figure 2.4: Nearest neighbor strectching and bending force constants versus bond length in (a) HfC-TiC, (b) TiC-ZrC, and (c) HfC-ZrC sytems. Squares and crosses indicate *ab initio* data points, and lines are linear fits used in the calculations of the vibrational free energy.

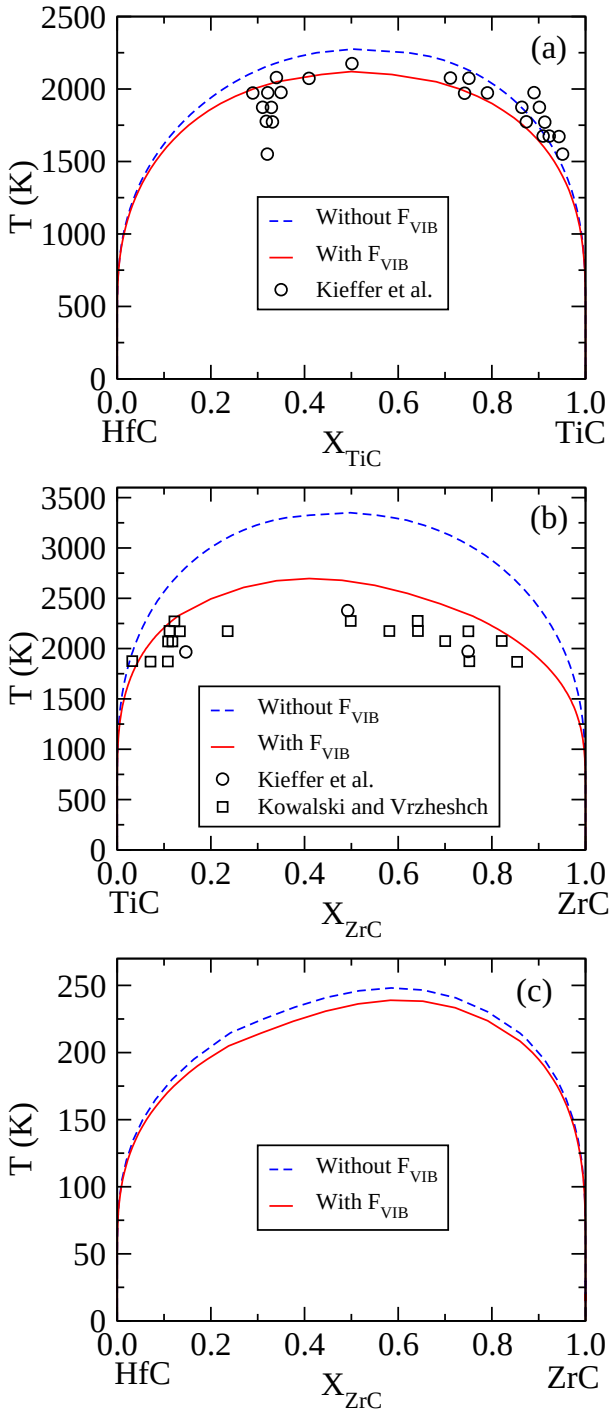

Figure 2.5: Calculated phase diagrams for the systems: (a) HfC-TiC, (b) TiC-ZrC, and (c) HfC-ZrC. Dashed (blue) curves are for calculations that did not include F_{vib}, and solid (red) curves are for calculations that did. Open circles are experimental data from Kieffer *et al.* [3]. Open squares are experimental data from Kowalskii and Vrzheshch [5].

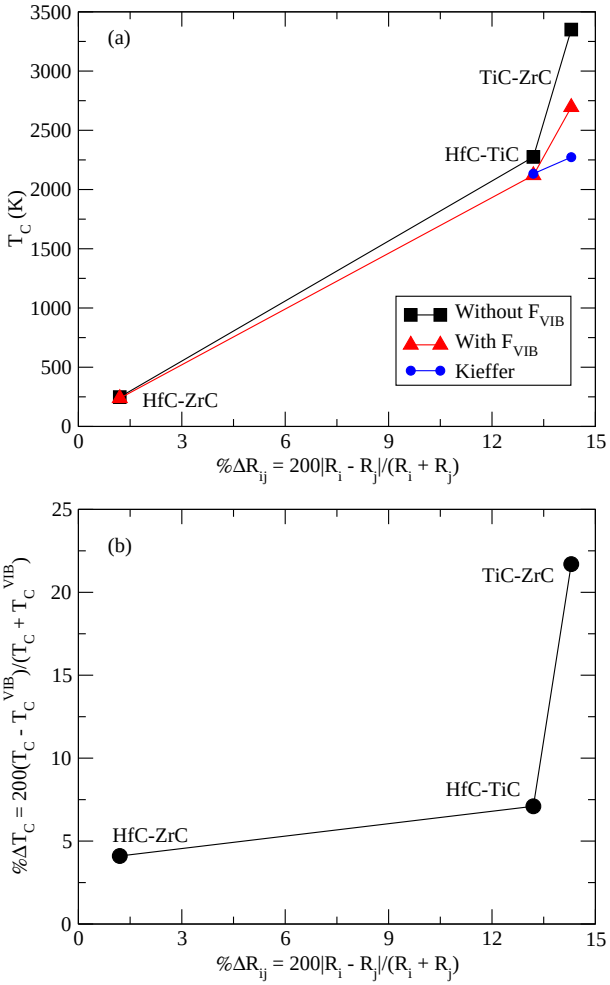

Figure 2.6: (a) Variation of the consolute temperature T_C as a function of the percentage difference in the ionic radii of exchangeable ions [42] from the calculations with (triangles) and without F_{vib} (squares). Experimental data are included for reference [3, 4]. (b) Related percentage reduction in T_C from including F_{vib} in the cluster expansion Hamiltonian.

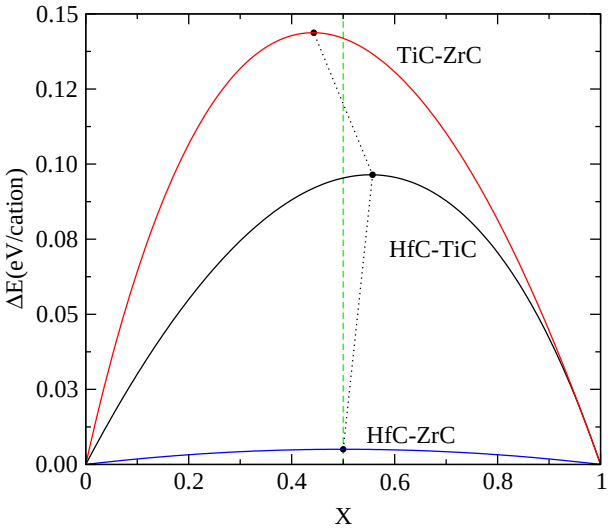

Figure 2.7: Elastic energy estimated by the $\epsilon - G$ approximation [45] for the systems HfC-TiC, TiC-ZrC, and HfC-ZrC. The dotted line connects the maximas.

Bibliography

[1] L. E. Toth, in Transition Metal Carbides and Nitrides, Academic Press, New York, 1971.

[2] H.-Y. Tsai, S.-C. Sun and S.-J. Wang, J. Electrochem. Soc. **147**, 2766 (2000).

[3] R. Kieffer, H. Nowotny, A. Neclcel, P. Ettmayer, and L. Usner, Montsh. Chem. **99**, 1020 (1968); R. Kieffer and P. Ettmayer, Angew. Chem. internat. Edit — Vol. 9 (1970) — No. 12.

[4] P. Rogl, S. K. Naik, and E. Rudy, Monatshefte für Chemie **108**, 1189 (1997).

[5] A.E. Kowalskii, E. Ya Vrzheshch, in: S.J. Bashkirov (Ed.), Hard Metals Production Technology and Research in the USSR, Pergamon Press, 1964.

[6] Murray J. L., in Phase Diagrams of Binary Titanium Alloys (Ed. J. L.Murray), Metals Park, Ohio, USA: ASM Int. Publ., 1987.

[7] T. B. Massalski,H. Okamoto, P. R. Subrmanian, and L. Kacprzak, Binary Alloys Phase Diagrams,Metals Park, Ohio, USA: ASM Int. Publ., 1990.

[8] E. K. Storms, The Refractory Carbides, New York: Academic Press, 1967.

[9] A. Markström, D. Andersson, and K. Frisk, Calphad **32**, 615 (2008).

[10] A. I. Gusev, Phys.-Usp. **43**, 1-37 (2000).

[11] E. M. Fedorov and R. A. Andrievskii, Izv. Akad. Nauk SSSR, Neog. Mater. **15**, 454 (1979).

[12] A. Zunger, S.-H. Wei, L.G. Ferreira, and J. E. Bernard, Phys. Rev. Lett. **65**, 353 (1990).

[13] K. A. Mäder and A. Zunger, Phys. Rev. B, **51**, 10462 (1995)

[14] I. A. Abrikosov, S. I. Simak, B. Johansson, A. V. Ruban, and H. L. Skriver, Phys Rev B **56**, 9319 (1997).

[15] C. Jiang, C. Wolverton, J. Sofo, L. Q. Chen, and Z.-K. Liu, Phys Rev B **69**, 214202 (2004).

[16] D. Shin, A. van de Walle, Y. Wang, and Z.-K. Liu, Phys Rev B, **76**, 144204 (2007).

[17] G. M. Stocks, D. M. Nicholson, W. A. Shelton, B. L. Gyorffy, F. J. Pinski, D. D. Johnson, *et al.* In: P. E. A. Turchi, A. Gonis, editors. Statics and dynamics of alloy phase transformations. NATO ASI Series. New York: Plenum Press; 1994.

[18] L. Vitos, I. A. Abrikosov, and B. Johansson, Phys. Rev. Lett. **87**, 156401 (2001).

[19] D. A. Rowlands, A. Ernst, B. L. Gyorffy, and J. B. Staunton, Phys. Rev. B, *73*, 165122 (2006).

[20] A. V. Ruban, S. I. Simak, S. Shallcross, and H. L. Skriver, Phys. Rev. B, *67*, 214302 (2003).

[21] A. E. Kissavos, S. Shallcross, L. Kaufman, O. Granas, A. V. Ruban, and I. A. Abrikosov, Phys. Rev. B **75**, 184203 (2007).

[22] B. Alling, A. V. Ruban, A. Karimi, O. E. Peil, S. I. Simak, L. Hultman, *et al.* Phys. Rev. B **75**, 045123 (2007).

[23] J. M. Sanchez, F. Ducastelle, and D. Gratias, Physica A **128**, 334 (1984).

[24] D. de Fontaine, Solid State Phys. **47**, 33 (1994).

[25] A. Zunger In: P. E. Turchi, and A. Finel, editors. Statics and dynamics of alloy phase transformations. NATO ASI Series. New York: Plenum Press; 1994.

[26] G. L. W. Hart, v. Blum, M. J. Walorski, and A. Zunger A., Nat. Mater. **4**, 391 (2005).

[27] A. van de Walle, G. Ghosh, and M. Asta, *Ab initio* modeling of alloy phase stability. In: G. Bozzolo, R. D. Noebe, and P. Abel, editors. Applied computational materials modeling: theory, simulation and experiment. New York: Springer; p. 1-34 (2007).

[28] A. van de Walle and G. Ceder, J. Phase Equilib. **23**, 348 (2002).

[29] A. van de Walle, M. Asta, and G. Ceder. CALPHAD J. **26**, 539 (2002).

[30] A. van de Walle and M. Asta, Modelling Simul. Mater. Sci. Eng. **10**, 521 (2002).

[31] B.P. Burton and A. Van de Walle, Phys. and Chem. Minerals **30**, 88 (2003).

[32] B.P. Burton and A. van de Walle, Chem. Geol. **225**, 222 (2006).

[33] B.P. Burton and A. van de Walle, J. Appl. Phys. **100**, 113528 (2006).

[34] B. P. Burton and T. Nishimatsu, Appl. Phys. Lett. **91**, 092907 (2007).

[35] J. Z. Liu, G. Ghosh, A. van de Walle, and M. Asta., Phys. Rev. B **75**, 104117 (2007).

[36] G. Ghosh, A. van de Walle, and M. Asta., Acta Mater. **56**, 3202 (2008).

[37] G. Kresse and J. Hafner, Phys. Rev. B **47**, 558 (1993); G. Kresse, Thesis, Technische Universität Wien 1993; Phys. Rev. B **49**, 14251 (1994); G. Kresse and J. Furthmüller, Comput. Mat. Sci. **6**, 15 (1996); Phys. Rev. B **54**, 11169 (1996); cf. http://tph.tuwien.ac.at/ vasp/guide/vasp.html.

[38] D. Vanderbilt, Phys. Rev. B **41**, 7892 (1990).

[39] J. P. Perdew, K. Burke, and M. Ernzerhof, Phys. Rev. Lett. **77**, 3865 (1996); **78**, 1396(E) (1997).

[40] A. van de Walle and G. Ceder, Rev. Mod. Phys. **74**, 11 (2002).

[41] E. J. Wu, G. Ceder, and A. van de Walle, Phys. Rev. B **67**, 134103 (2003).

[42] R. D. Shannon and C. T. Prewitt, Acta Cryst. B **25**, 925 (1969).

[43] L. G. ferriera, A. A. Mbaye, and A. Zunger, Phys. Rev. B **35**, 6475 (1987).

[44] A. Zunger, S-H. Wei, A. A. Mbaye and L. G. ferriera, Acta Metall. **36**, 2239 (1987).

[45] L. G. ferriera, A. A. Mbaye, and A. Zunger, Phys. Rev. B **37**, 10547 (1988).

[46] B. P. Burton, N. Dupin, S. G. Fries, G. Grimvall, A. Fernández Guillermet, P. Miodownik, W. A. Oats and V. Vinograd, Zeitschrift für Metallkunde **92**, 514 (2001).

Chapter 3

Mg_2SiO_4 liquid under high pressure from molecular dynamics

3.1 Abstract

We use a flexible potential model to perform large-scale molecular dynamics simulations of Mg_2SiO_4 melt up to pressures of 24 GPa and at temperatures between 2390 K and 3200 K. We find that thermal pressure and the Grüneisen parameter γ increase linearly with density, independent on temperature. γ increases from 0.5 at ambient pressure to 0.75 at 24 GPa. While Si stays overwhelmingly in tetrahedral coordination, the coordination of Mg increases significantly under compression, from an average 5-fold coordination at room pressure to 7-fold coordination at 24 GPa. Medium range order in Mg_2SiO_4 as expressed by X-ray and neutron structure factors change considerably with pressure, with features at low wave-vectors q sharpening considerably and shifting to higher q. Diffusivity of the atomic species in Mg_2SiO_4 decrease uniformly with pressure and are well described by an Arrhenius law. For viscosity η we find good agreement with experiments at room pressure, and predict a rapid increase with pressure.

3.2 Introduction

Melting is a ubiquitous process in planetary interiors that has major consequences for their chemical and thermal evolution. The importance of melts in the Earth range from extraction of basalt at mid-ocean ridges to the large scale magma ocean that governed the dynamics of the early planet [1]. As the major component of the Earth's upper mantle the magnesium orthosilicate Mg_2SiO_4 is of considerable importance.

Despite this importance the knowledge of thermodynamic and transport properties of Mg_2SiO_4 melt is limited. This is partly caused by the high melting point of Mg_2SiO_4 (2163±25 K [2]) that has lead to extrapolations of properties from supercooled liquids to high temperatures [e.g. 3] or extrapolation from other compositions to Mg_2SiO_4 [e.g. 4, 5]. Such extrapolations produce conflicting results for a number of properties, such as heat capacity [3, 6, 7] or compressibility [4, 8, 9] (Table 1). As the melting temperature increases rapidly with pressure [10], high pressure experiments on Mg_2SiO_4 melts are even more difficult and scarce.

Aside from the thermodynamic properties mentioned in the previous paragraph transport properties of the melt, such as viscosity, are of central importance as crystal growth [11], crystal settling [12] and convection dynamics [13] critically depend on them. Despite this importance there is limited information on melt viscosity, in particular at high pressure. At high pressure viscosity is measured most directly by the "falling sphere" method, in which the sinking velocity of a solid sphere through a liquid can be related to viscosity by Stokes' law [14–16]. For low viscosity depolymerized melts, such as diopside [15], peridotite [16] or the Mg_2SiO_4 liquid studied here, the fast sinking velocity makes the measurements challenging.

Ultimately, changes in physical properties must be caused by structural changes in the melt that are difficult to monitor experimentally. For a quantitative analysis using nuclear magnetic resonance for ^{27}Al, ^{29}Si or ^{17}O [17–19] samples must be synthesized at high pressure and temperature, and the quenched glass can then be analyzed at room pressure.

Alternatively, structure factors of quenched glasses can be measured with X-rays or neutrons and reveal structural correlations between different components. Such studies on Mg_2SiO_4 [20] reveal that glass/melt connectivity result from Mg-O polyhedra. SiO_4 units, that typically serve as network formers, show almost no connectivity, with Si_2O_7 dimers (Q^1 species) coexisting with isolated SiO_4 units (Q^0 species). In analogy to the crystalline phases, connectivity in the melt and coordination of Si can be expected to increase with pressure, but quantitative experiments to this extent have not been performed to date.

In light of these difficulties numerous molecular dynamics simulations on structure and physical properties of silicate melts have been performed over the past few years, with the goal to predict physical properties and to relate structural properties with macroscopic observables. These include the properties mentioned above, but the interpretation of integrated structural signals such as X-ray or neutron structure factors also depend critically on an understanding of the various partial contributions to the measured signal [21].

Computations for liquids typically fall in two categories: electronic structure (*ab-initio*) computations [22–28] and potential model simulations [29–33]. *Ab-initio* computations provide an accurate description of bonding and electronic structure and are transferable between different structure types and to different thermodynamic conditions (e.g. high pressure). Computational requirements, however, pose severe limitations on the maximum simulation cell size and run duration: *Ab-initio* studies are typically limited to a few hundred atoms in the cell and run durations of a few picoseconds (ps). While such short run durations allow for the evaluation of thermodynamic properties, longer runs and larger cells are needed to reliably obtain transport properties. Pair potentials [30] or shell models [29] are often used to efficiently explore physical properties; large system sizes and long run durations are readily accessible. However, such potentials suffer from the fact that they are typically fit to a set of experimental data and their transferability to different compositions or different thermodynamic conditions is limited.

Both of these simulation approaches have limitations for a comprehensive study of thermodynamic and transport properties of melts at high pressure and temperature, and here we attempt to bridge the gap between them. We apply an advanced ionic model that is derived from electronic structure calculations. The so called Aspherical Ion Model (AIM) [34, 35] has been applied successfully before for oxide melts, e.g. MgO melt [36],

Al_2O_3 melt [21] and MgO-Al_2O_3 melts [37]. Recently, a set of AIM-type potentials was constructed for silicates, which has successfully been applied to study crystalline magnesiosilicate materials in a wide range of pressures and temperatures [38]. Here we explore structural, thermodynamic, and transport properties of Mg_2SiO_4 liquid over a wide pressure and temperature range of 0-24 GPa and 2390-3200 K, respectively. The current manuscript is organized as follows: after briefly introducing the method and computational setup we explore the thermodynamics of the melt using a Mie-Grüneisen description of the thermal equation of state. We look at structural properties and transport properties in the melt along an isotherm of 2800 K. Results are compared to experimental data where available, and the behavior predicted is discussed. In the final section, conclusions are given.

3.3 Model and computational details

Details of the AIM interaction model and its parameterization are described elsewhere [34, 35]. In short, the AIM interatomic potential V is constructed from four components

$$V = V^{qq} + V^{disp} + V^{rep} + V^{pol} \tag{3.1}$$

The first two components, the charge-charge (V^{qq}) and dispersion (V^{disp}) interactions, are purely pairwise additive:

$$V^{qq} = \sum_{i \leq j} \frac{q^i q^j}{r_{ij}}, \tag{3.2}$$

$$V^{disp} = -\sum_{i \leq j} [f_6^{ij}(r_{ij}) C_6^{ij}/r_{ij}^6 + f_8^{ij}(r_{ij}) C_8^{ij}/r_{ij}^8], \tag{3.3}$$

where q^i is the formal charge on ion i (+4 for Si, +2 for Mg and -2 for O), C_6^{ij} and C_8^{ij} are the dipole-dipole and dipole-quadrupole dispersion coefficients respectively, and f_n^{ij} are Tang-Toennies dispersion damping functions [39], which describe short-range corrections to the asymptotic dispersion term.

The overlap repulsion component (V^{rep}) is given by

$$\begin{aligned} V^{rep} &= \sum_{i \in O, j \in Mg,Si} [A^{-+} e^{-a^{-+}\rho^{ij}} + B^{-+} e^{-b^{-+}\rho^{ij}} + C^{-+} e^{-c^{-+} r_{ij}}] \\ &+ \sum_{i,j \in O} A^{--} e^{-a^{--} r_{ij}} \\ &+ \sum_{i \in O} [D(e^{\beta\delta\sigma^i} + e^{-\beta\delta\sigma^i}) + (e^{\zeta^2 |\nu^i|^2} - 1) + (e^{\eta^2 |\kappa^i|^2} - 1)], \end{aligned} \tag{3.4}$$

with

$$\rho^{ij} = r_{ij} - \delta\sigma^i - S_\alpha^{(1)} \nu_\alpha^i - S_{\alpha\beta}^{(2)} \kappa_{\alpha\beta}^i, \tag{3.5}$$

and summation of repeated indexes is implied. The variable $\delta\sigma^i$ characterizes the deviation of the radius of oxide anion i from its default value, $\{\nu_\alpha^i\}$ are a set of three variables describing the Cartesian components of a dipolar distortion of the ion, and $\{\kappa_{\alpha\beta}^i\}$ are a set

of five independent variables describing the corresponding quadrupolar shape distortions ($\mid \kappa \mid^2 = \kappa_{xx}^2 + \kappa_{yy}^2 + \kappa_{zz}^2 + 2(\kappa_{xy}^2 + \kappa_{xz}^2 + \kappa_{yz}^2)$ with a traceless matrix κ). $S_\alpha^{(1)} = r_{ij,\alpha}/r_{ij}$ and $S_{\alpha\beta}^{(2)} = 3r_{ij,\alpha}r_{ij,\beta}/r_{ij}^2 - \delta_{\alpha\beta}$ are interaction tensors. The last summations include the self-energy terms, representing the energy required to deform the anion charge density, with β, ζ and η as effective force constants. The extent of each ion's distortion is determined at each molecular dynamics time-step by energy minimization.

The polarization part of the potential incorporates dipolar and quadrupolar contributions [40],

$$\begin{aligned} V^{pol} &= \sum_{i,j\in O} \Bigg((q^i\mu_\alpha^j - q^j\mu_\alpha^i)T_\alpha^{(1)} + (\frac{q^i\theta_{\alpha\beta}^j}{3} + \frac{\theta_{\alpha\beta}^i q^j}{3} - \mu_\alpha^i\mu_\beta^j)T_{\alpha\beta}^{(2)} \\ &\quad + (\frac{\mu_\alpha^i\theta_{\beta\gamma}^j}{3} + \frac{\theta_{\alpha\beta}^i\mu_\gamma^j}{3})T_{\alpha\beta\gamma}^{(3)} + \frac{\theta_{\alpha\beta}^i\theta_{\gamma\delta}^j}{9}T_{\alpha\beta\gamma\delta}^{(4)}) \Bigg) \\ &+ \sum_{i\in O, j\in Mg,Si} \left(q^j\mu_\alpha^i[1 - g_D(r^{ij})]T_\alpha^{(1)} + \frac{\theta_{\alpha\beta}^i q^j}{3}[1 - g_Q(r^{ij})]T_{\alpha\beta}^{(2)} \right) \\ &+ \sum_{i\in O} \left(k_1 \mid \vec{\mu}^i \mid^2 + k_2\mu_\alpha^i\theta_{\alpha\beta}^i\mu_\beta^i + k_3\theta_{\alpha\beta}^i\theta_{\alpha\beta}^i + k_4 \mid \vec{\mu}^i \cdot \vec{\mu}^i \mid^2 \right), \end{aligned} \tag{3.6}$$

where $k_1 = \frac{1}{2\alpha}$, $k_2 = \frac{B}{4\alpha^2 C}$, $k_3 = \frac{1}{6C}$, $k_4 = \frac{-B^2}{16\alpha^4 C}$, α, B and C the dipole, dipole-dipole-quadrupole and quadrupole polarizabilities of the oxygen ion, respectively, and $T_{\alpha\beta\gamma\delta} = \nabla_\alpha\nabla_\beta\nabla_\gamma\nabla_\delta ... \frac{1}{r_{ij}}$ are the multipole interaction tensors [41]. The instantaneous values of these moments are obtained by minimization of this expression. The charge-dipole and charge-quadrupole cation-anion asymptotic functions include terms which account for penetration effects at short-range by using Tang-Toennies damping functions [39] of the form,

$$g_D(r^{ij}) = c_D e^{-b_D r^{ij}} \sum_{k=0}^{4} \frac{(b_D r^{ij})^k}{k!}, \tag{3.7}$$

$$g_Q(r^{ij}) = c_Q e^{-b_Q r^{ij}} \sum_{k=0}^{6} \frac{(b_Q r^{ij})^k}{k!}, \tag{3.8}$$

with D and Q standing for dipolar and quadrupolar parts. While the parameters b_D and b_Q determine the range at which the overlap of the charge densities affects the induced multipoles, the parameters c_D and c_Q determine the strength of the ion response to this effect. Only oxygen ions are considered polarizable.

The set of AIM potentials used here was parameterized for the Ca-Mg-Al-Si-O system by reference to electronic structure calculations. The model was shown to be accurate and transferable in a wide range of pressures, temperatures and compositions [38]. Here, the same set of interatomic potentials and the same AIM code is used.

Molecular dynamics (MD) simulations are performed using a cubic simulation box with 2016 ions (288 formula units). At each MD step, the energy of the 'electronic degrees of freedom' (ionic polarization and deformation) is minimized before the ions are moved. This effectively describes many-body interactions (for more details see [34]). To

integrate Newton's equation of motion for the ions the code uses the Leapfrog algorithm [42], and we choose a time step of 1 fs. The starting configuration was obtained from a disordered structure of an aluminate melt by replacing the respective cations, which was followed by a 200 ps equilibration run at high temperature (3000 K). In the second half of this run, no measurable changes in the structural and dynamic properties of interest are observed and hence we concluded that equilibrium was achieved. At each pressure and temperature, additional equilibration runs of 50 ps are performed in the NPT ensemble using an isotropic barostat [43] coupled to a Nosé-Hoover thermostat [44] with a relaxation time of 6 ps. After equilibration, the barostat is switched off and production runs of 150 ps length are started in the NVT ensemble. Trajectories, the stress tensor and other properties are recorded every 10 time steps, i.e. with time interval of 10 fs. We explore a pressure range from 0 to 24 GPa, with steps of 4 GPa, and temperatures of 2390, 2600, 2800, 3000 and 3200 K.

3.4 Results and Discussion

3.4.1 Thermodynamics properties

In order to describe the thermodynamic properties of the Mg_2SiO_4 liquid we fit the results from the simulations with the thermal equation of state:

$$P(V,T) = P_{iso}(V,T_{ref}) + P_{therm}(V,T), \tag{3.9}$$

where the isothermal equation of state $P_{iso}(V,T_{ref})$ is evaluated at $T_{ref} = 2800$ K by a third order finite strain (Birch-Murnaghan) equation of state [45]:

$$P_{iso}(V,T_{ref}) = 3K_0 f\,(1+2f)^{5/2}\left[1+\frac{3}{2}\left(K_0^{'}-4\right)\right], \tag{3.10}$$

with the Eulerian finite strain

$$f = \frac{1}{2}\left[\left(\frac{V_0}{V}\right)^{\frac{2}{3}}-1\right]. \tag{3.11}$$

V_0, K_0, and $K_0^{'}$ are the volume, isothermal bulk modulus (K_T), and its pressure derivative at zero pressure, respectively. The third order finite strain equation of state is found to represent well the results from the simulations for all temperatures considered (Fig. 3.1). Equation-of-state parameters for T_{ref} are $V_0 = 55.0 \pm 0.3$ cm^3/mol (or $\rho_0 = 2.56$ g/cm^3), $K_0 = 26 \pm 2$ GPa, and $K_0^{'} = 5.8 \pm 0.5$.

We approximate the thermal pressure P_{therm} by the Mie-Grüneisen model:

$$P_{therm} = \left(\frac{\partial P}{\partial T}\right)_V (T - T_{ref}). \tag{3.12}$$

Through Maxwell relations the prefactor $(\partial P/\partial T)$ is related to K_T, the thermal expansivity (α), the Grüneisen parameter (γ) and the isochoric heat capacity (C_V):

$$\left(\frac{\partial P}{\partial T}\right)_V = \alpha K_T = \frac{\gamma C_V}{V}. \tag{3.13}$$

We evaluate $\partial P/\partial T$ by fitting isothermal equations of state for all simulation temperatures to obtain K_T and compute the thermal expansion coefficient from the volume-temperature relation at constant pressure:

$$\alpha = \frac{1}{V}\left(\frac{\partial V}{\partial T}\right)_P. \tag{3.14}$$

Similar to solids [e.g. 46] we find α to decrease rapidly with pressure. In our simulations it is, however, essentially independent on temperature for the range considered (Fig. 3.2). This is similar to results by Guillot and Sator [32] that find thermal expansivity constant for a wide range of melt compositions and a fairly large temperature range.

From considering the energetics (enthalpy H) of our simulations we are able to compute the isobaric heat capacity (C_P) of the liquid:

$$C_P = \left(\frac{\partial H}{\partial T}\right)_P. \tag{3.15}$$

As for α we find C_P to be independent on T, and use C_P, α, K_T, and V to compute C_V:

$$C_V = C_P - VT\alpha^2 K_T. \tag{3.16}$$

We find an isochoric heat capacity of $C_V = 3.75 \pm 0.1$ R. C_V is not only temperature- but also pressure-independent in our simulations, and we can readily invert eq. 3.13 for γ and find it is best described by a linear volume dependence (Fig. 3.3):

$$\gamma = \gamma_0 + \gamma^{'}\left(V - V_{0,ref}\right), \tag{3.17}$$

where we choose again $T = 2800$ K as the reference temperature. Fitting eq. 3.17 we obtain $\gamma_0 = 0.50 \pm 0.05$ and $\gamma^{'} = -0.016 \pm 0.003$ mol/cm^3.

To compare our results with previous experimental [3, 4, 6, 8, 9, 47] and computational estimates [28, 32, 33] on thermodynamic data we have compiled a table with physical properties, combining different experiments where necessary to compute properties (Table 1).

We find our results to be consistent with the *ab-initio* computations [28], except for heat capacity C_V where we predict a value considerably smaller (3.75 R compared to 4.4 R in the *ab-initio* results). The simulations using classical potentials [32, 33] unfortunately do not report a full set of thermodynamic properties, but only isothermal equations-of-state (Table 1); in these calculations, however, the zero pressure volume is predicted larger, accompanied in part by a smaller bulk modulus.

The results for the thermal equation-of-state are consistent with experimental data, although some of the compressional parameters (bulk modulus K_0 and its pressure derivative $K_0^{'}$ show large variations between different experiments. K_0 from Rivers and Carmichael [9] is in good agreement with all computational results, while values from Lange and Carmichael [4] and Bottinga [8] are significantly more and less compressible, respectively.

The one experimental value reported for $K_0^{'} = 3.8$ [8] is considerably smaller than all computational results, making the melt less compressible at higher pressure. The difference in bulk moduli is also reflected in the Grüneisen parameter γ where good agreement between computational results and experiments can only be obtained with the bulk modulus from Rivers and Carmichael [9]. For heat capacity our results are consistent with lower estimates, but the majority of values based on the experimental literature are larger, in good agreement with the *ab-initio* results [28].

The increase of γ with pressure predicted here agrees with the recent *ab-initio* results on Mg_2SiO_4 melt [28], although the increase predicted here is somewhat smaller (Fig. 3.3). It also follows systematics of other recent simulations on $MgSiO_3$ melt [24] and MgO [25]. Such behavior is in contrast to solids where the Grüneisen parameter generally decreases with increasing pressure [48], and only structural changes can lead to an increase of γ, e.g. for the α to β transition in Mg_2SiO_4 [49]. Shock wave experiments on Mg_2SiO_4 [50] also infer a strong increase of γ for the melt with pressure and obtain $\gamma \sim 2.6$ at pressures between 150-200 GPa.

A significant increase of γ has considerable bearings on the thermal state of a magma ocean as it would result in a much steeper adiabat in the magma ocean [50] than conventionally thought [51]. As Mosenfelder *et al.* [50] demonstrate this could lead to a crystallization of the magma ocean beginning near the surface or at depths of the transition zone.

3.4.2 Structural properties

Structural changes in the liquid are likely to be the underlying cause for the increase in γ discussed above and therefore we explore the structure of the liquid as a function of pressure from our simulations. From particle positions we compute the partial radial distribution functions $g_{ij}(r)$ $(i, j \in [Mg, Si, O])$. Oscillations in $g_{SiO}(r)$ only extend to the next nearest neighbor distance (~ 4.2 Å) (Fig. 3.4) showing the SiO_4 structural unit behaves rather rigidly. This holds not only for low pressures, but persists to 24 GPa; up to this pressure $\sim 80\%$ of the Si is in four-fold coordination (see discussion below). $g_{MgO}(r)$ and $g_{OO}(r)$ show fluctuations well beyond that range, indicating an ionic-like character of the liquid (Fig. 3.4). While the nearest neighbor cation-oxygen distances are almost unaffected by pressure, the oxygen-oxygen and second neighbor cation-oxygen distances are considerably shifted to lower r with increasing pressure.

Cation coordination numbers are obtained by counting the number of oxygens within the first coordination shell. The cutoff distance is defined by the first minimum in the respective $g_{ij}(r)$. We find only a modest increase in Si-O coordination, with an average coordination increase from 4.0 at 0 GPa to 4.2 at 24 GPa (Fig. 3.5). This stems from the fact that in our simulations $\sim 80\%$ of the Si remain four-fold coordinated while the rest of the Si are five-fold coordinated. Even at 24 GPa there is only a negligible amount of the Si in six-fold coordination. This is in contrast to the *ab-initio* results [28] that show a stronger increase in coordination (and connectivity). The rigid ion molecular dynamics [32] also predicts a rapid increase with pressure, capturing structural changes in the melt well.

Coordination for Mg increases considerably with pressure, and here our results agree

with those of the *ab-initio* computations [28] and the rigid ion model [32] (Fig. 3.5).

Apparently, the atomic structure of the melt depends in a sensitive way on the details of the interaction model. The high stability of the SiO_4 suggests that the Si-O interaction in the AIM potential may be slightly too strong.

In the pressure range considered, compression in the melt structure is taken up mostly by rearrangements of the second neighbor Si-O and O-O distances which is also represented by a rearrangement in the Si-O-Si bond angle (Fig. 3.6). Under compression the Si-O-Si angle distribution is shifted to smaller angles, allowing for a more dense packing of the SiO_4 tetrahedra.

In experiments the radial distribution function can not be obtained directly, but its Fourier transform is accessible in diffraction experiments where the total X-ray ($S^{X-ray}(q)$) or neutron structure factors ($S^{neu}(q)$) are measured. For a multicomponent system, the total structure factor is a weighted sum of partial structure factors, which represent structural correlations between the different components.

Since X-ray scattering gives almost equal weight to all three different species (O^{2-}, Mg^{2+} and Si^{4+} are isoelectronic), and neutrons are particularly sensitive to the positions of the oxygen ions, these two techniques give complementary structural information. The X-ray weighted structure factor, $S^{X-ray}(q)$, is determined from partial structure factors $S_{\alpha\beta}(q)$ by weighting them with X-ray form factors,

$$S^{X-ray}(q) = \frac{1}{\sum_\alpha N_\alpha f_\alpha^2(q)} \sum_{\alpha\beta} \sqrt{N_\alpha N_\beta} f_\alpha(q) f_\beta(q) S_{\alpha\beta}(q), \tag{3.18}$$

with $\alpha, \beta \in [Mg, Si, O]$ and $N_{\alpha,\beta}$ being the total number of ions of type α and β, respectively. The form factors $f_\alpha(q)$ depend on the magnitude of the wave-vector q. Note that the $f_\alpha(q)$ are taken from the literature [52]. Similarly, the neutron weighted structure factor, $S^{neu}(q)$, is determined by weighting them with the experimental coherent neutron scattering lengths $b_\alpha(\alpha \in [Mg, Si, O])$ [53]:

$$S^{neu}(q) = \frac{1}{\sum_\alpha N_\alpha b_\alpha^2} \sum_{\alpha\beta} \sqrt{N_\alpha N_\beta} b_\alpha b_\beta S_{\alpha\beta}(q). \tag{3.19}$$

Hence, the partial structure factors are needed to interpret diffraction data of complex melts but they are very difficult to obtain experimentally. However, the $S_{\alpha\beta}(q)$ are readily available from molecular dynamics simulations. At ambient pressure both $S^{X-ray}(q)$ and $S^{neu}(q)$ of Mg_2SiO_4 melt show few distinct features (Fig. 3.7). In $S^{X-ray}(q)$ two peaks at $q \sim 2.3$ Å^{-1} (A) and $q \sim 4.5$ Å^{-1} (C) can be identified. Contributions to (A) and (C) are from Mg-Mg and Mg-Si interactions primarily, with negative (canceling) contributions from Mg-O. In $S^{neu}(q)$ only (C) is clearly identifiable. At higher pressure the peaks sharpen, and an additional peak (B) becomes visible in $S^{X-ray}(q)$. This peak has significant contributions from O-O and Mg-O pairs, and is located in between the peaks of these two partial structure factors. At low pressure the broad O-O peak makes (B) invisible. Due to the smaller amplitude of the Mg-Mg and Mg-Si pairs in $S^{neu}(q)$, with the negative contribution from Mg-O essentially the same (A) can not be observed in $S^{neu}(q)$. The q position of the peak (A) at 0 GPa (~ 2.3 Å^{-1}) is in good agreement with the experimental data of Kohara *et al.* [20] on the structure of Mg_2SiO_4 glasses (~ 2.2 Å^{-1}).

The first Si-O peak at 0 GPa (~ 1.6 Å^{-1}), only visible in the partial structure factor is comparable to the position of the Si-O peak in vitreous silica and other nonorthosilicate glasses and melts (< 1.8 Å^{-1}) [54, 55].

Changes in the shapes of both $S^{X-ray}(q)$ and $S^{neu}(q)$ with pressure are significant: amplitudes of (A), (B) and (C) increase and shift to higher q.

3.4.3 Transport properties

Due to the long run durations and large system size we can reliably compute the diffusion coefficient D of the individual atomic species from the molecular dynamics runs via the Einstein relation [42]:

$$D_\alpha = \lim_{t\to\infty} \frac{1}{N_\alpha} \sum_{i=1}^{N_\alpha} \frac{\langle (\boldsymbol{r}_i(t+t_0) - \boldsymbol{r}_i(t_0))^2 \rangle}{6t}, \tag{3.20}$$

where $\boldsymbol{r}_i$ is the position of i^{th} ion of species α at time t after origin time t_0, and ensemble averages of the mean square displacements are taken for a specific species with a total number of ions N_α. As in the case for solid Mg_2SiO_4 [56] we find that the network modifying ion (Mg) diffuses much faster than the network forming cation (Si): $D_{Mg} >> D_O >> D_{Si}$ (Fig. 3.8).

We analyze our time series of mean square displacement in terms of uncertainty and found a standard deviation that is smaller than the symbol size in Fig. 3.8.

The diffusion coefficients decrease with pressure following an Arrhenius law (Fig. 3.8), and unlike for more polymerized melts [26] there is no initial increase in D. Diffusivities computed from *ab-initio* by de Koker *et al.* [28] and the potential model by Lacks *et al.* [33] report diffusivities larger by ~ 0.5 log units, and there is good agreement between the potential model and the *ab-initio* results. The *ab-initio* results show a much larger uncertainty in the diffusion constants, due to the smaller simulation cell. Experimental data on melt diffusivities are not available at the present time.

We compute the shear viscosity η from the Green-Kubo relation [42] which involves integration over time of the autocorrelation function for the off-diagonal components of the stress tensor:

$$\eta = \frac{V}{k_B T} \int_0^\infty dt \langle \sigma_{ij}(t+t_0)\sigma_{ij}(t_0) \rangle. \tag{3.21}$$

Here $\langle - \rangle$ denotes the thermal average, k_B is the Boltzmann constant, and σ_{ij} $(i \neq j)$ are the off-diagonal components of the stress tensor σ_{ij}. The three components of the stress tensor are averaged to obtain η. Uncertainties in η are estimated from fluctuations in the stress tensor.

The computed viscosity of Mg_2SiO_4 liquid at 2800 K at zero pressure is consistent with experimental data at ambient pressure [57] extrapolated to 2800 K (Fig. 3.9).

Within the standard deviations we can fit the pressure dependence of viscosity with an exponential function, increasing with pressure. In the rigid ion model [33] the viscosity is computed considerably smaller, consistent with their larger values for D.

This is in contrast to experimental estimates on melt viscosity for depolymerized melts, where for both diopside [15] and peridotite [16] viscosity initially increase with

pressure, then decrease. In Liebske *et al.* (2005) the initial increase was attributed to a redistribution of intertetrahedral angle, while the subsequent decrease was interpreted as an increase in coordination of network-forming cations. However, here we do not find any indication of sudden changes in coordination, but a continuous change, as many other computational studies [24–26, 28, 32] although to a smaller extent (Fig. 3.5).

In order to elucidate the experimentally observed anomaly by computations careful studies will be necessary, with a dense simulation grid in pressure and temperature, in order to pinpoint an anomaly closely. Also, the fluctuations in the stress tensor will need to be decreased considerably in order to improve the uncertainty in viscosity. From our simulations we find that longer run durations will do little to decrease the standard deviation, simulations on yet larger cells may be necessary.

3.5 Conclusions

Here we perform molecular dynamics simulations on Mg_2SiO_4 melt on a dense pressure - temperature grid over a wide pressure (0-24 GPa) and temperature (2390 - 3200 K) range, using a flexible potential model that has been successfully applied for high pressure and temperature properties of solids in the CMAS system and in oxide melts. We find that over the pressure range considered structural changes in the Mg_2SiO_4 melt are continuous, with only a slight increase in coordination of Si, and considerable coordination change in Mg. The observed change in Si coordination is smaller than in *ab-initio* [28] and rigid ion [32] simulations, hinting at a Si-O bond that is too strong in our potential model. Structural changes predicted by the present model should be observable in X-ray and neutron experiments as significant changes in the respective static structure factors occur, mostly driven by changing Mg coordination and interactions in the melt.

Contrary to solids under pressure we find thermal pressure and the Grüneisen parameter to increase with compression, consistent with recent shock wave experiments [50] and simulations in Mg_2SiO_4 [28] and other depolymerized silicate (and oxide) melts [24–26].

Large simulation cells and long run durations allow us to analyze the simulations in terms of transport properties of the melt, diffusivity and viscosity and estimate uncertainties on these properties from the simuations. We find that Mg is the fastest diffusing species over the whole compression range, but the difference between O- and Mg-diffusivity decreases considerably at high pressure. Diffusivities obtained are somewhat smaller than those of other recent *ab-initio* [28] and potential [33] simulations. The diffusivities computed can be fit readily with an Arrhenius law. For viscosity we find good agreement between the value computed from the Kubo-Green relations in the simulations and experiments at room pressure. Viscosity increases as a function of pressure.

3.6 Acknowledgments

We greatly appreciate helpful discussions with D. Dolejš, N. de Koker and D. C. Rubie. This work was partially funded by the State of Bavaria through the Graduate School "Structure, Reactivity and Properties of Oxide Materials".

3.7 Table

Table 3.1: Thermodynamic parameters for Mg_2SiO_4 melt at 0 GPa and 2390 K, comparing our fit to experimental data, extrapolated to 2390 K. Experimental data at other temperatures are included for comparison and the temperature are included. Equation of state parameters are also included for recent *ab-initio* and rigid ion molecular dynamics.

Property	AIM (2390 K, 0 GPa)	Experiment	Simulations Olivine ^{*,g} Mg_2SiO_4 ^{h}	*ab initio* ^{i}
V_0 (cm^3/mol)	53.5 ± 0.2	54.9 ± 0.2 ^{a} 53.6 ± 0.3 ^{b}	56.3 ^{g} (2273 K) 58.1 ^{h} (3000 K)	53.55 (2163 K)
K_0 (GPa)	27 ± 3	11^{b} 59 ^{c} (2494 K) 20 ± 1 ^{e}	18 ^{g} (2273 K) 16 ^{h} (3000 K)	23 ± 8 (2163 K)
K_0'	6.3 ± 0.5	3.8 ^{c} (2494 K)	7.2 ^{g} (2273 K) 6.4 ^{h} (3000 K)	7 ± 1 (2163 K)
α (10^{-6} K^{-1})	74± 15	119 ± 7 ^{a} 82 ^{c} (2163 K)		121 ± 50 (2163 K)
C_V (R)	3.75 ± 0.1	4.5 ± 0.4 ^{a,b,d} 3.5 ^{a,b,f} 4.2 ± 0.2 ^{a,d,e}		4.4 ± 0.5 (2163 K)
γ	0.50 ± 0.08	0.27 ± 0.05 ^{a,b,d} 0.34 ± 0.03 ^{a,b,f} 0.52 ± 0.08 ^{a,d,e}		0.6 ± 0.1 (2163 K)

* composition close to Fo90
^{a} Lange, 1997
^{b} Lange and Carmichael, 1987
^{c} Bottinga, 1985
^{d} Stebbins *et al.,* 1984
^{e} Rivers and Carmichael, 1987
^{f} Tangemann *et al.,* 2001
^{g} Guillot and Sator, 2007b
^{h} Lacks *et al.,* 2007
^{i} de Koker *et al.,* 2008

3.8 Figures

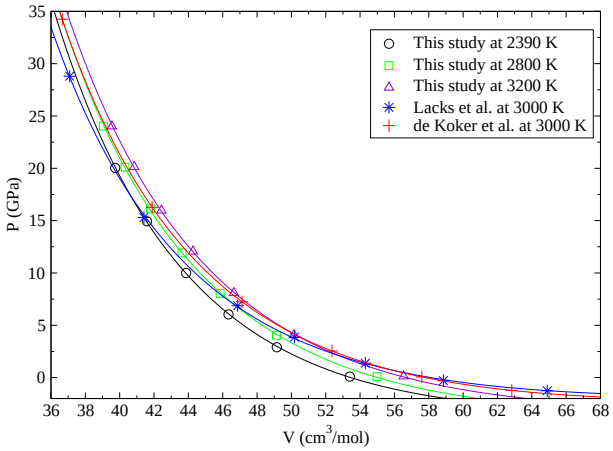

Figure 3.1: (color online) Pressure-volume equation of state for Mg_2SiO_4 liquid. Results from the molecular dynamics simulations (open symbols) and third-order Birch-Murnaghan equation of state fits (lines) at 3200 K (purple, triangles), 2800 K (green, squares), and 2390 K (black, circles) are shown. For comparison *ab-initio* [28] (red, crosses) and rigid ion simulation results [33] at 3000 K are included (blue, stars).

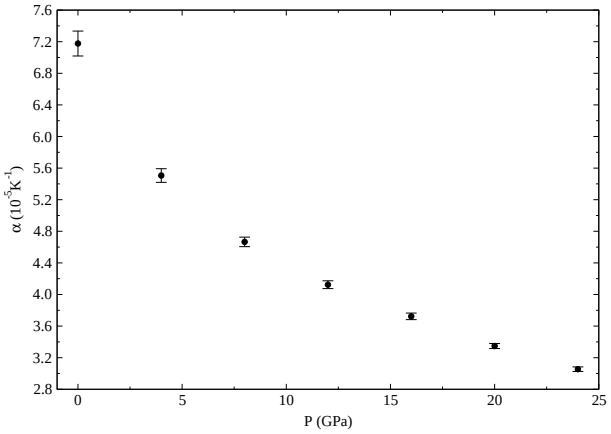

Figure 3.2: Thermal expansion (α) as a function of pressure for Mg_2SiO_4 liquid. α is found independent on temperature.

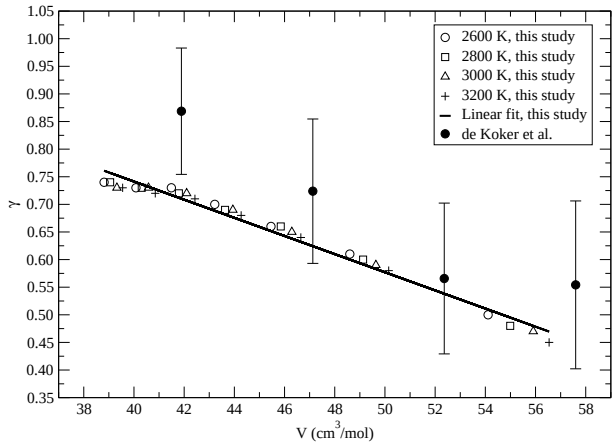

Figure 3.3: Grüneisen parameter γ as a function of volume for Mg_2SiO_4 liquid. Values for different temperature simulations are shown by the symbols, and a linear fit to the results is included. For comparison γ from recent *ab-initio* results [28] are included.

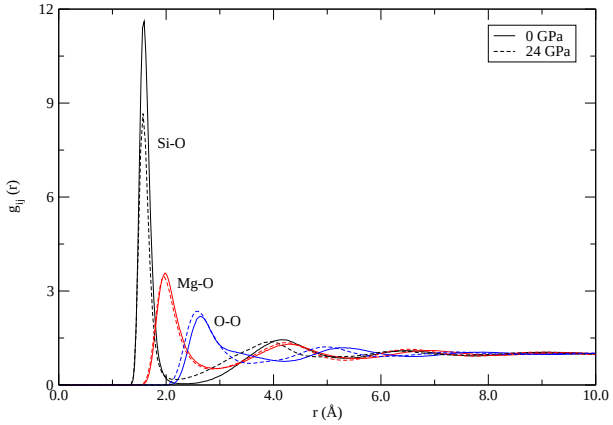

Figure 3.4: (color online) Radial distribution functions of Si-O (black), Mg-O (blue) and O-O (red) at 0 GPa (solid lines) and 24 GPa (dashed lines) at 2800 K.

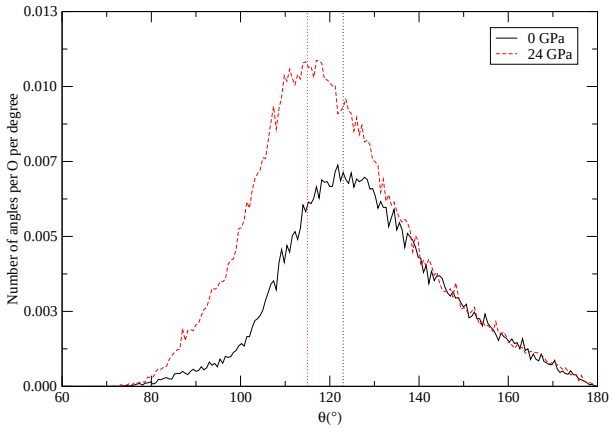

Figure 3.5: (color online) Average Si (a) and Mg (b) coordination numbers of Mg_2SiO_4. Closed circles present our results at 2800 K. For comparison we have included simulation results from *ab-initio* [28] at 3000 K (black squares) and rigid ion simulations [32] on peridotite liquid at 2273 K (blue line).

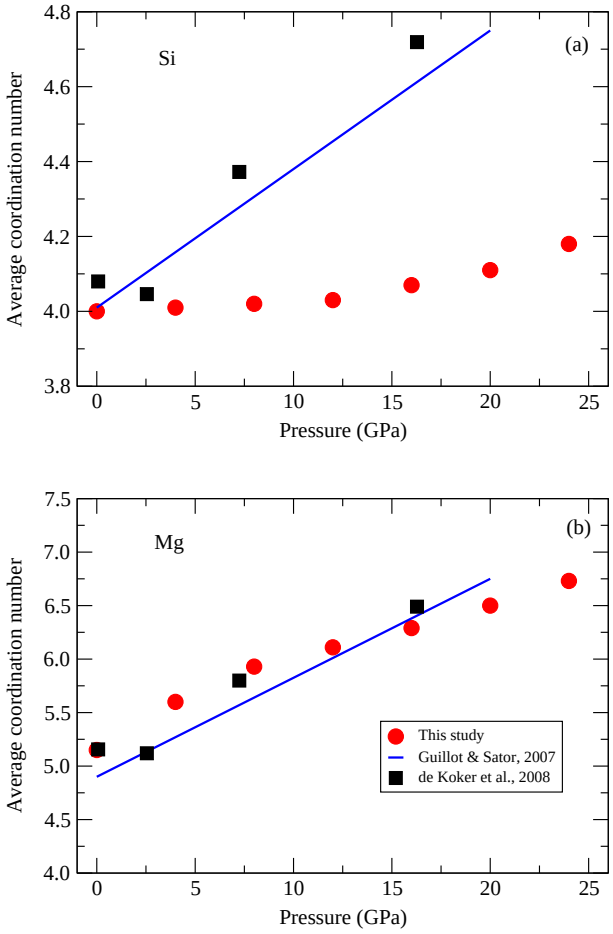

Figure 3.6: (color online) Bond-angle distribution of Si-O-Si bonds at 0 GPa (solid black line) and 24 GPa (dashed red line) at 2800 K. Vertical lines show the maximum in the distribution function.

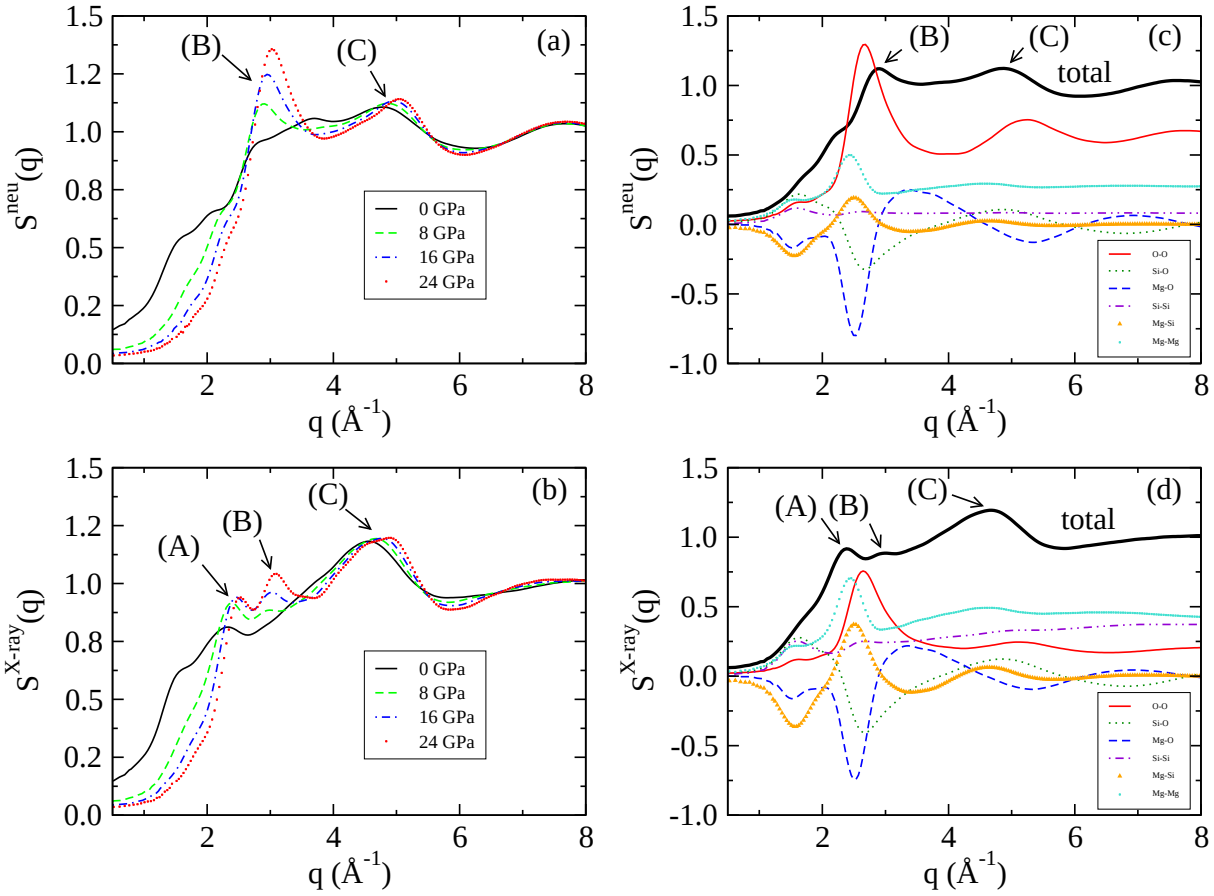

Figure 3.7: (color online) Neutron (a) and X-ray (b) weighted total structure factors of Mg_2SiO_4 liquid at 2800 K and four different pressures. Contribution of partial structure factors to the neutron (c) and X-ray (d) total structure factor at 8 GPa.

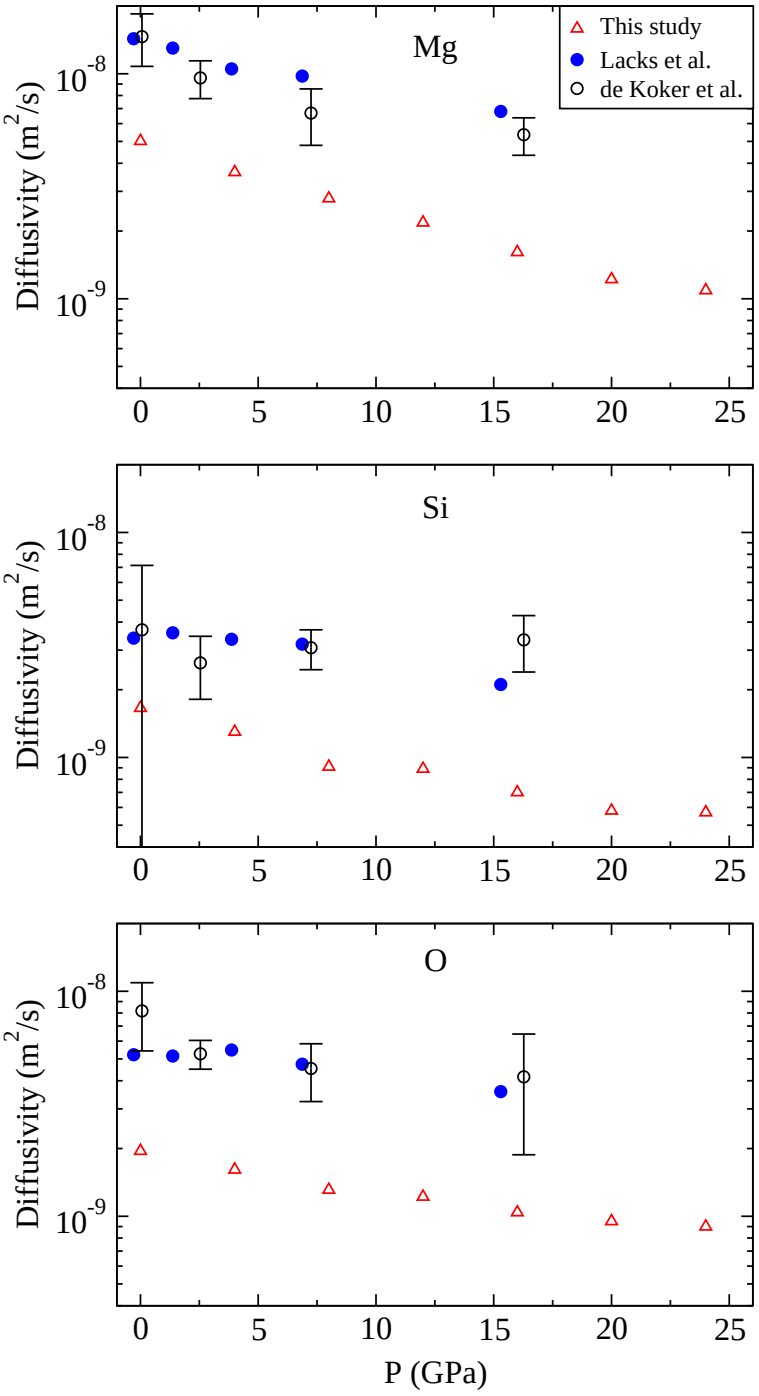

Figure 3.8: (color online) Diffusivity of the atomic species in Mg_2SiO_4 melt as a function of pressure. The upper panel shows the diffusivity for Mg, the middle panel for Si and the lower panel for O. Open red triangles present our results at 2800 K. Filled blue circles are from the rigid ion simulations Lacks *et al.* [33] and open diamonds from the *ab-initio* molecular dynamics by de Koker *et al.* [28], both at 3000 K.

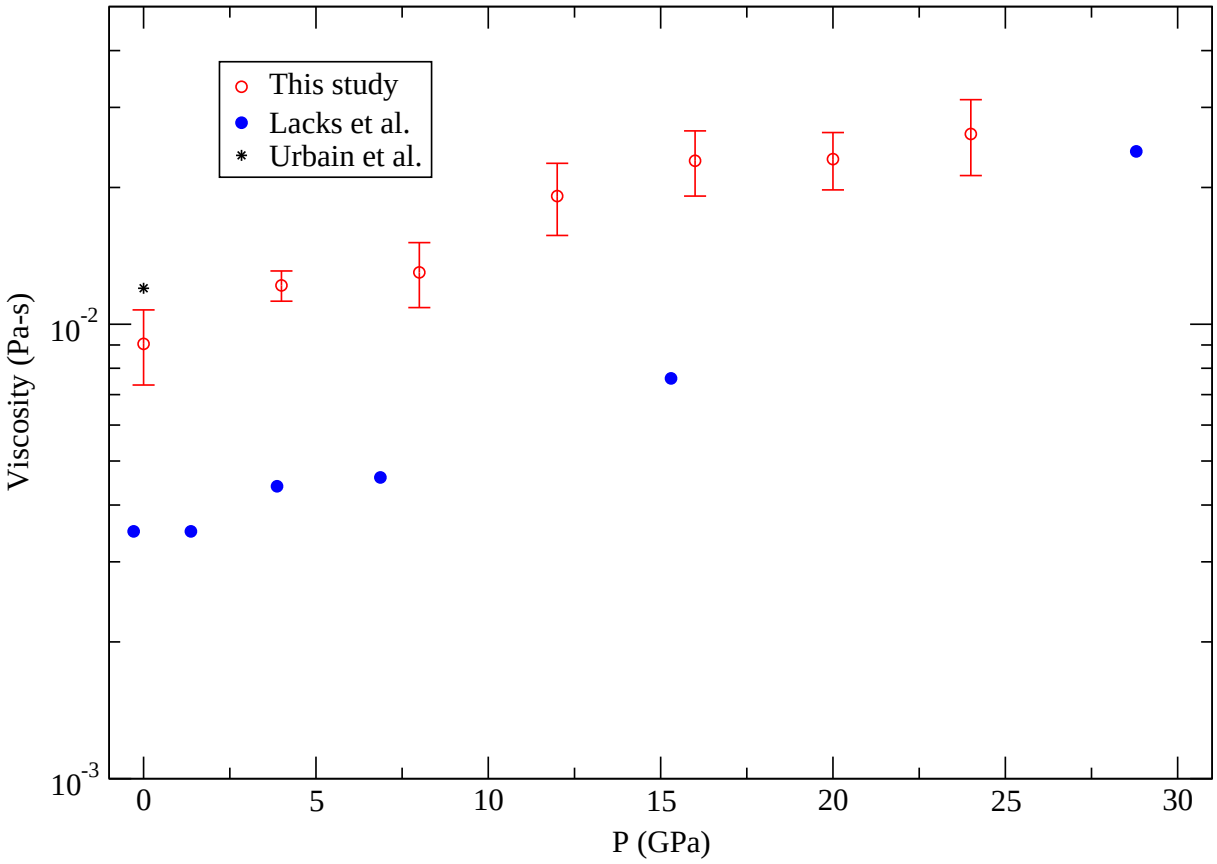

Figure 3.9: (color online) Viscosity of Mg_2SiO_4 melt as a function of pressure. Open red diamonds show our results at 2800 K, including an estimate of uncertainty.. Filled blue circles are from the rigid ion simulations of [33] at 3000 K. The star shows the experimental viscosity of Urbain *et al.* [57] at 0 GPa, extrapolated to 2800 K.

Bibliography

[1] Tonks, W.B., Melosh, H.J., 1993. Magma ocean formation due to giant impacts, J. Geophys. Res. 98, 5319-5333.

[2] Bowen, N.L., Andersen, O., 1914. The binary system MgO-SiO_2. Am. J. Sci. 37, 487-500.

[3] Tangemann, J.A., Phyllips, B.L., Navrotsky, A., Weber, J.K.R., Hixson, A.D., Key, T.A., 2001. Vitreous forsterite (Mg_2SiO_4): Synthesis, structure, and thermochemistry. Geophysical research letters 28, 2517-2520.

[4] Lange, R.A., Carmichael, I.S.E., 1987. Densities of Na_2O-K_2O-CaO-MgO-FeO-Fe_2O_3-Al_2O_3-TiO_2-SiO_2 liquids: new measurements and derived partial molar properties. Geochim. Cosmochim. Acta 51, 2931-2946.

[5] Rigden, S.M., Ahrens, T.J., Stolper, E.M., 1989. High-pressure equation of state of molten anorthite and diopside. J. Geophys. Res. 94, 9508-9522.

[6] Stebbins, J.F., Carmichael, I.S.E., Moret, L.K., 1984. Heat capacities and entropies of silicate liquids and glasses. Contrib. Mineral. Petrol. 86, 131-148.

[7] Lange, R., Navrotsky ,A., 1992. Heat capacities of Fe_2O_3-bearing silicate liquids. Contrib. Mineral. Petrol. 110, 311-320.

[8] Bottinga, Y., 1985. On the isothermal compressibility of silicate liquids at high pressure. Earth. Plant. Sci. Lett. 74, 350-360.

[9] Rivers, M.L., Carmichael, I.S.E., 1987. Ultrasonic studies of silicate melts. J. Geophys. Res. 92, 9247-9270.

[10] Ohtani, E., Kumazawa, M., 1981. Melting of forsterite Mg_2SiO_4 up to 15 GPa. Phys. Earth Planet. Inter. 27, 32-38.

[11] Solomatov, V.S., D.J., Stevenson, 1993. Kinetics of crystal growth in a terrestrial magma ocean. J. Geophys. Res. 98, 5407-5418.

[12] Solomatov, V.S., D.J., Stevenson, 1993. Suspension in convective layers and style of differentiation of a terrestrial magma ocean. J. Geophys. Res. 98, 5375-5390.

[13] Abe, Y., 1997. Thermal and chemical evolution of the terrestrial magma ocean. Phys. Earth Planet. Inter. 100, 27-39.

[14] Kushiro, I., 1978. Density and viscosity of hydrous calc-alkalic andesite magma at high pressure, Year B.-Carnegie Inst. Wash. 77 , 675-678.

[15] Reid, J.E., Suzuki, A., Funakoshi, K., Terasaki, H., Poe, B.T., Rubie, D.C., Ohtani, E., 2003. The viscosity of $CaMgSi_2O_6$ liquid at pressures up to 13 GPa. Phys. Earth Planet. Inter. 139, 45-54.

[16] Liebske, C., Schmickler, B., Terasaki, H., T. Poe, B.T., Suzuki, A., Funakoshi, K., Ando, R., Rubie, D.C., 2005. Viscosity of peridotite liquid up to 13 GPa: Implications for magma ocean viscosities. Earth Planet. Sci. Lett. 240, 589-604.

[17] Fiske, P.S., Nellis, W.J., Xu, Z., Stebbins, J.F., 1998. Shocked quartz; a ^{29}Si magic-angle-spinning nuclear magnetic resonance study. Am. Mineral. 83, 1285-1292.

[18] Allwardt, J.R., Stebbins, J.F., Terasaki, H., Du, L.-S., Frost, D.J., Withers, A.C., Hirschmann, M.M, Suzuki, A., Ohtani,E., 2007. Effect of structural transitions on properties of high-pressure silicate melts: ^{27}Al NMR, glass densities, and melt viscosities. Am. Mineral. 92, 1093-1104.

[19] Kelsey, K.E., Stebbins, J.F., Du, L.-S., Hankins, B., 2007. Constraining ^{17}O and ^{27}Al NMR spectra of high-pressure crystals and glasses: New data for jadeite, pyrope, grossular, and mullite. Am. Mineral. 92, 210-216.

[20] Kohara, S., Suzuya, K., Takeuchi, K., Loong, C.-K, Grimsditch, M., Weber, J.K.R., Tangeman, J.A., Key, T.S., 2004. Glass Formation at the Limit of Insufficient Network Formers. Sciences 303, 1649-1652.

[21] Jahn, S., Madden, P.A., 2007. Structure and dynamics in liquid alumina: Simulations with an *ab initio* interaction potential J. Non-Cryst. Solids 353, 3500-3504.

[22] Vocadlo, L., Alfe, D., Price, G. D., Gillan, M.J., 2000. First principles calculations on the diffusivity and viscosity of liquid Fe-S at experimentally accessible conditions. Phys. Earth Planet. Inter. 120, 145-152.

[23] Belonoshko, A.B., Skorodumova, N.V., Rosengren, A., Ahuja, R.,Johansson, B., Burakovsky, L., Preston, D.L., 2005. High-Pressure Melting of $MgSiO_3$. Phys. Rev. Lett. 94, 195701 (4 pages).

[24] Stixrude, L., Karki, B., 2005. Structure and freezing of $MgSiO_3$ liquid in Earth's lower mantle. Science 310, 297-299.

[25] Karki, B.B, Bhattarai, D., Stixrude, L., 2006. First-principles calculations of the structural, dynamical, and electronic properties of liquid MgO. Phys. Rev. B 73, 174208 (7 pages).

[26] Karki, B.B, Bhattarai, D., Stixrude, L., 2007. First-principles simulations of liquid silica: Structural and dynamical behavior at high pressure. Phys. Rev. B 76, 104205 (12 pages).

[27] Wan, J. T. K., Duffy, T. S., Scandolo, S., Car, R., 2007. First-principles study of density, viscosity, and diffusion coefficients of liquid $MgSiO_3$ at conditions of the Earth's deep mantle, J. Geophys. Res., 112, B03208, doi:10.1029/2005JB004135.

[28] de Koker, N.P., Stixrude, L., Karki, B.B., 2008. Thermodynamics, structure, dynamics, and freezing of Mg_2SiO_4 liquid at high pressure.Geochim. Cosmochim. Acta 72, 1427-1441.

[29] Gale, J.D., Catlow, C.R.A., Mackrodt, W.C., 1992. Periodic *ab initio* determination of interatomic potentials for alumina. Modell. Simul. Mater. Sci. Eng. 1, 73-81.

[30] Matsui, M., 1994. A transferable interatomic potential model for crystals and melts in the system CaO-MgO-Al_2O_3-SiO_2. Miner. Mag. 58A, 571-572.

[31] Guillot, B., Sator, N., 2007. A computer simulation study of natural silicate melts. Part I: Low pressure properties. Geochim. Cosmochim. Acta 71, 1249-1265.

[32] Guillot, B., Sator, N., 2007. A computer simulation study of natural silicate melts. Part II: High pressure properties. Geochim. Cosmochim. Acta 71, 4538-4556.

[33] Lacks, D.J., Rear, D.B., Van Orman, J.A., 2007. Molecular dynamics investigation of viscosity, chemical diffusivities and partial molar volumes of liquids along the MgO-SiO_2 join as functions of pressure. Geochim. Cosmochim. Acta 71, 1312-1323.

[34] Aguado, A., Bernasconi, L., Jahn, S., Madden, P.A., 2003. Multipoles and interaction potentials in ionic materials from planewave-DFT calculations. Faraday Discuss. 124, 171-184.

[35] Madden, P.A., Heaton, R., Aguado, A., Jahn, S., 2006. From first-principles to material properties. J. Mol. Struct. (Theochem) 771, 9-18.

[36] Aguado, A., Madden, P.A., 2005. New Insights into the Melting Behavior of MgO from Molecular Dynamics Simulations: The Importance of Premelting Effects. Phys. Rev. Lett. 94, 68501 (4 pages).

[37] Jahn, S., 2008. Atomic structure and transport properties of MgO-Al_2O_3 melts: A molecular dynamics simulation study. Am. Mineral. **93**, 1486 -1492.

[38] Jahn, S., Madden P.A., 2007. Modeling Earth materials from crustal to lower mantle conditions: A transferable set of interaction potentials for the CMAS system. Phys. Earth Planet. Inter. 162, 129-139.

[39] Tang, K.T., Toennies J.P., 1984. An improved simple model for the van der Waals potential based on universal damping functions for the dispersion coefficients. J. Chem. Phys. 80, 3726-3741.

[40] Wilson, M., Madden P.A., Costa-Cabral B.J., 1996. Quadrupole polarization in simulations of ionic systems: Application to AgCl, J. Phys. Chem. 100, 1227-1237.

[41] Stone, A.J., 1996. The theory of intermolecular forces. Oxford University Press, Oxford.

[42] Allen, M.P., Tildesley, D.J., 1987. Computer Simulation of Liquids. Oxford University Press, New York.

[43] Martyna, G.J., Tobias, D.J., Klein, M.L., 1994. Constant pressure molecular dynamics algorithms. J. Chem. Phys. 101, 4177-4189.

[44] Nosé, S., Klein, M.L., 1983. Constant pressure molecular dynamics for molecular systems. Mol. Phys. 50, 1055-1076.

[45] Birch, F., 1952. Elasticity and constitution of the earth's interior. J. Geophys. Res. 57, 227-286.

[46] Chopelas, A., 1989. Thermal properties of forsterite at mantle pressures derived from vibrational spectroscopy. Phys. Chem. Minerals 17, 149-156.

[47] Lange, R.A., 1997. A revised model for the density and thermal expansivity of K_2O-Na_2O-CaO-MgO-Al_2O_3-SiO_2 liquids from 700 to 1900 K: extension to crustal magmatic temperatures, Contrib. Mineral. Petrol. 130, 111.

[48] Karki, B.B., Wentzcovitch, R.M., de Gironcoli, S., Baroni, S., 2001. *Ab initio* lattice dynamics of $MgSiO_3$ perovskite at high pressure. Phys. Rev. B 62, 14750-14756.

[49] Stixrude, L., Lithgow-Bertelloni, C., 2007. Influence of phase transformations on lateral heterogeneity and dynamics in Earth's mantle. Earth and Planet. Sci. Lett. 263, 45-55.

[50] Mosenfelder, J.L., Asimow, P.D., Ahrens, T.J., 2007. Thermodynamic properties of Mg_2SiO_4 liquid at ultra-high pressures from shock measurements to 200 GPa on forsterite and wadsleyite. J. Geophys. Res. 112, B06208, doi:10.1029/2006JB004364.

[51] Miller, G.H., Stolper, E.M., Ahrens, T.j, 1991. The equation of state of a molten komatiite. 2. Application to komatiite petrogenesis and the Hadean mantle. J. Geophys. Res 96, 11849-11864.

[52] Cromer, D. T., Waber, J.T., 1974. International Tables for X-ray Crystallography, vol. IV, Kynoch Press, Birmingham, UK, pages 71-147.

[53] Sears, V.S., 1992. Neutron scattering lengths and cross sections. Neutron News 3, 26-37.

[54] Waseda, Y., 1980, Experimental techniques for structural analysis of non-crystalline materials. Structure of Non-crystalline Materials, McGraw-Hill, New York.

[55] Kohara, S., Suzuya, K., 2003. High-energy X-ray diffraction studies of disordered materials. Nucl. Instrum. Methods B199, 23-28.

[56] Andersson, K., G. Borchardt, K., Scherrer, S., Weber, S., 1989. Self-diffusion in Mg_2SiO_4 (forsterite) at high temperature. Fresenius' J. Analy. Chem. 333, 383-385.

[57] Urbain, G., Bottinga, Y., Richet, P., 1982. Viscosity of liquid silica, silicates and alumino-silicates. Geochim. Cosmochim. Acta 46, 1061-1072.

Chapter 4

Transport properties of Mg_2SiO_4 melt at high pressure: Viscosity of the magma ocean

4.1 Abstract

We use a flexible potential model to perform large-scale molecular dynamics simulations on diffusivity and viscosity of Mg_2SiO_4 melt up to pressures of 32 GPa and over a temperature range of 2600 to 3200 K. We find that diffusivity decreases uniformly with pressure, and viscosity increases unformly with pressure from values of 10^{-2} at 0 GPa to 10^{-1} Pas at 32 GPa (2600 K). Both transport properties can be readily fit with a closed Arrhenius expression over the whole pressure and temperature range considered. The independent estimates on diffusivity and viscosity allow us to examine their relation through the Eyring equation. The proportionality factor between them, the translation distance for a diffusion event, is determined as 18 Å at 0 GPa, and decreases with pressure. Combining previous simulation results on thermodynamics with the current viscosity fit we compute a magma ocean adiabat and the associated viscosity profile. These estimates allow us to constrain bounds on the Prandtl ($Pr_{max} < 75$) and Rayleigh number ($Ra > 10^{27}$) of the magma ocean that determine its convective regime.

4.2 Introduction

Viscosity of silicate melts is of central importance in many geological settings as it determines how magmas bodies cool, flow and erupt. Knowing the dependence of viscosity on temperature (e.g. Urbain *et al.* [1]), pressure [2–4], composition [1, 4] and water content [5–7] is hence of great importance in geochemistry and geophysics. High pressure (P) properties of silicate melts are necessary in order to interpret the potential occurrence of partial melt on top of the 410 km discontinuity [8] and the core-mantle boundary [9, 10]. In the young Earth the thermal and chemical evolution of our planet is governed by physical properties of melt that made up the magma ocean [11]. Viscosity of the silicate magma ocean is central to the understanding of convective dynamics [12] and its thermal evolution [12, 13] and has a strong influence on crystal growth and settling [14, 15] as well

as equilibration between the core-forming metal liquid and the proto-mantle [16].

With (MgO+FeO)/SiO_2 ratios of ∼1.7 for the primitive Earth (chondritic, [17]) and the eutectic point moving towards Mg_2SiO_4 at higher pressures [18–20] melts in the Earth are dominated by Mg_2SiO_4. As the major component in the magma ocean the properties of liquid Mg_2SiO_4 are of fundamental interest in understanding its structure and dynamics.

Despite this importance the knowledge of thermodynamic and transport properties of Mg_2SiO_4 melt from experiment is limited. This is partly caused by the high melting point of Mg_2SiO_4 (2163±25 K [21]) that has lead to extrapolations of properties from supercooled liquids to high temperatures [e.g. 22] or extrapolation from other compositions to Mg_2SiO_4 [e.g. 23, 24]. As the melting temperature increases rapidly with pressure [18] high P experiments on Mg_2SiO_4 melts are even more difficult and scarce. Viscosity measurements of Mg_2SiO_4 are restricted to ambient pressure (2300 K $\lesssim T \lesssim$ 2500 K) [1].

At high pressure, direct measurements of viscosity are based on the "falling sphere" method, in which the viscosity of a liquid can be computed from the sinking velocity of a solid sphere through a liquid by Stokes' law, monitored by X-ray radiography [2, 3, 25]. Due to the low viscosity (high velocity) the falling sphere method is extremely challenging for depolymerized melt compositions, including Mg_2SiO_4. Experiments on depolymerized liquid compositions have been performed for $CaMgSi_2O_6$ [2] and a peridotite liquid [3]. In both cases viscosity increased with pressure up to ∼ 9 GPa, and then decreased up to the highest pressures examined (∼ 13 GPa).

Determination of self-diffusion of oxygen and silicon are more readily accessible in the laboratory and can be measured over a wider pressure and temperature range [26–28] and then related to viscosity through the Eyring relation:

$$D = \frac{k_B T}{\lambda \eta}. \tag{4.1}$$

Here, D is the diffusion coefficient, k_B the Boltzmann constant, T the temperature, η the viscosity, and λ the ionic translation distance for a diffusion event. The value of λ is subject of debate. Phenomenologically it is found that $\lambda = 2R$ (with R the ionic radius of the diffusing species [29]) yields good correlation between D and η for oxygen diffusivity [26, 27] while other studies require a larger λ [e.g. 2, 30]. The anomaly reported for viscosity in $CaMgSi_2O_6$ [2] and peridotite [3] is reflected in diffusivity measurements [28, 31] which show a minimum at 10 GPa and 9 GPa, respectively. For peridotite, D shows a maximum near 16 GPa, after which the diffusivity decreases again [31].

Molecular dynamics (MD) simulations provide a complementary route to explore the high P and high temperature (T) behavior of silicate melts, including Mg_2SiO_4 *Ab-inito* computations based on density functional theory (DFT) are accurate and transferable, but they are computationally demanding, and cell sizes for simulations for silicate melts have been restricted to a few atoms and run durations to a few picoseconds (ps) [32–36]. This allows for accurate determination of structural and thermodynamic properties, but in order to obtain good statistics for the fluctuation formula that define transport properties much longer run durations are required (hundreds of ps). As statistical noise decreases with $1/\sqrt{N}$, where N is the number of atoms in the system, large simulation cells are required to obtain geophysically relevant precision of transport properties.

Empirical potentials [4, 37–40] are often used to efficiently explore physical properties;

large system sizes and long run durations are readily accessible. However, such potentials suffer from the fact that they are typically fit to a set of experimental data and their transferability to different compositions or different thermodynamic conditions is not guaranted. Using potential methods Guillot and Sator [40] have investigated diffusivity for peridotite at 2273 K up to 20 GPa, and found a maximum in D at 3 GPa. Similarly, Lacks *et al.* [4] computed D and viscosity for both $MgSiO_3$ and Mg_2SiO_4 at 3000 K and up to $\sim$ 50 GPa using pair potentials and, in agreement with Guillot and Sator [40], found an initial increase in D (as well as a decrease in η) for $MgSiO_3$ up to 3 GPa; for Mg_2SiO_4, by contrast, they do not predict an increase in D. Neither of these studies show the anomaly characteristic of the experiments in the depolymerized melt compositions at $\sim$10 GPa discussed above.

As pointed out in the previous paragraphs these simulation approaches have limitations for a comprehensive study of transport properties of melts at high pressure and temperature, and here we attempt to bridge the gap between them. We apply the Aspherical Ion Model (AIM) [41, 42] that is derived from electronic structure calculations. In AIM, potentials were constructed for silicates which have successfully been applied to study crystalline magnesiosilicate materials over a wide range of P and T [43] as well as Mg_2SiO_4 melts [45]. Overall, the AIM results for Mg_2SiO_4 melts show good agreement with the *ab-initio* thermodynamic results [36] and good experimental zero pressure η [1]. Here we expand our previous study on thermodynamic and transport properties of Mg_2SiO_4 melt and compute the pressure (P) and T dependence of diffusivity and viscosity between 0-32 GPa and 2600-3000 K, covering the proposed P-T range of the magma ocean (e.g. Righter [44]). As we obtain D and η independently from one another the computations provide a direct means to explore the validity of the Eyring relation.

4.3 Method

The AIM interaction model and its parameterization are described elsewhere [41, 42]. The model takes into account the Coulomb interaction between charged particles, short-range repulsion due to the overlap of the charge densities, dispersion, ionic polarization effects and ion shape deformations. The set of AIM potentials used here was parameterized for the Ca-Mg-Al-Si-O system by reference to electronic structure calculations. We use the same set of potentials that was constructed for crystalline magnesiosilicate [43] and that we applied in our previous work on the thermodynamics of Mg_2SiO_4 melt [45].

Molecular dynamics simulations were performed using a cubic simulation box with 2016 ions (288 formula units, similar to the simulation cell by Lacks *et al.* [4]), with a time step of 1 fs for the numerical integration of the equations of motion. Simulations are performed at constant P and T until equilibrium is achieved, then the volume is held constant. T is controlled by a Nosé-Hoover thermostat [46] with the relaxation time of 6 ps. The equilibration is performed with an isotropic barostat [47] coupled to the thermostat for 50 ps before the production run of 150 ps length is started. We explore a pressure range from 0 to 32 GPa, with steps of 4 GPa, and temperatures of 2600, 2800, 3000 and 3200 K.

Due to long run durations and large system size we can reliably compute the diffusion coefficient D of the individual atomic species from the molecular dynamics runs via the

Einstein relation [48]:

$$D_\alpha = \lim_{t\to\infty} \frac{1}{N_\alpha} \sum_{i=1}^{N_\alpha} \frac{\langle (\boldsymbol{r}_i(t) - \boldsymbol{r}_i(0))^2 \rangle}{6t}, \tag{4.2}$$

where $\boldsymbol{r}_i$ is the position of i^{th} ion of species α at time t, and ensemble averages of the mean square displacements are taken for a specific species with a total number of ions N_α.

Shear viscosity η is computed by the Green-Kubo relation [48] which involves integration over time of the autocorrelation function for the off-diagonal components of the stress tensor:

$$\eta = \frac{V}{k_B T} \int_0^\infty dt \langle \sigma_{ij}(t)\sigma_{ij}(0) \rangle. \tag{4.3}$$

Here $\langle - \rangle$ denotes the thermal average, V is the system volume, k_B is the Boltzmann constant, and σ_{ij} $(i \neq j)$ are the off-diagonal components of the stress tensor σ_{ij}. The three components of the stress tensor are averaged to obtain η.

In contrast to smaller cell sizes our computations do not suffer from finite size effects and both D and η are well converged. We have looked at finite cell size effects in detail and find well converged results for $\sim$ 1000 atoms.

4.4 Results

Aggregate diffusivity of Mg_2SiO_4 in our simulations increases slightly with T in our simulations and decreases uniformly with P (Fig. 4.1), being reduced by $\sim$ 0.3 log-units from 0 to 32 GPa at 3000 K. Overall, it is well represented by a closed Arrhenius relation

$$D = D_0 exp\left[-\frac{E_a + PV_a}{RT}\right], \tag{4.4}$$

where E_a and V_a are the activation energy and volume, respectively. D_0 is a pre-exponential factor (Table 4.1 and Fig. 4.1). The computed pressure dependence of D is similar to results by de Koker *et al.* [36] and Lacks *et al.* [4], although our D values are $\sim$ 0.5 log-units lower than in those studies. As discussed above we can here see the low precision in the *ab-initio* simulations [36] due to small cell sizes: the uncertainty on D can reach values in excess of one log-unit.

Total diffusivity in Mg_2SiO_4 is well approximated by the O-diffusivity, as O is the dominant ionic species and has intermediate diffusivity compared to the network modifyers (Mg) and the network former (Si) [4, 36, 45]. In agreement with the previous simulations we do not compute an anomalous behavior in D in the 10-15 GPa range as has been observed experimentally for diopside [2, 28] and peridotite [3].

Similar to diffusivity, viscosity η decreases with T and increases with P (Fig. 4.1), again consistent with previous simulations using ionic potentials [4], except for their highest pressure point which shows a much stronger increase in η. Consistent with lower values in D viscosity in our simulations is computed higher (by $\sim$ 0.3 log-units) than in Lacks *et al.* [4]. As for D the computed viscosities can readily be fit with a closed Arrhenius

expression, with η_0 as a pre-exponential factor (Table 4.1):

$$\eta = \eta_0 exp\left[\frac{E_a + PV_a}{RT}\right]. \tag{4.5}$$

At zero pressure simulation results for D and η can be related via the Eyring relation (eq. 4.1) with a diffusion distance $\lambda = 18$ Å (or $\sim 13\ R_O$, with $R_O = 1.4$ Å the ionic radius for oxygen, [29]) (Fig. 4.2). From the simulations a T depedence cannot be resolved, but using the Arrhenius fit to both D and η a slight increase in λ with T is apparent (Fig. 4.2). λ computed here is lower than that obtained by Lacks *et al.* [4] ($\sim 16\ R_O$), but significantly larger than for $CaMgSi_2O_6$ (λ =3.2 R_O) [2] and more polymerized melts (e.g. Shimizu and Kushiro [26], Poe *et al.* [27], Reid *et al.* [28], Tinker *et al.* [30]).

The Eyring relation can also be derived from considering the Brownian motion of a sphere moving through a fluid, leading to the Stokes-Einstein equation which is equivalent to eq. 4.1. Here, λ is related to the radius of the moving sphere (r) by $\lambda = 4\pi r$ for a free-slip fluid-sphere and $\lambda = 6\pi r$ for a no-slip boundary sphere [4]. The value obtained for bulk diffusivity in Mg_2SiO_4 melt is very similar to the theoretical value for a free slip fluid sphere with $r = R_O$.

With the activation energy E_a and volume V_a for D and η different (Table 4.1) it is apparent that λ depends on P and T. We find that λ decreases with P (to $\sim 9\ R_O$ at 32 GPa) but as for zero pressure the simulation results themselves can not resolve a T-dependence at high pressure (Fig. 4.2).

4.5 Discussion

With a ratio of non-bridging oxygen per tetrahedrally coordinated cation (NBO/T) of 4.0, Mg_2SiO_4 categorizes as a depolymerized composition. With NBO/T=2 $MgSiO_3$, the other major component of mantle mineralogy, is also a depolymerized composition. As thermodynamic [49, 50] and transport properties [4] between these two melt compositions are predicted to be very similar, it is possible to explore magma ocean structure by thermodynamic and viscosity results for Mg_2SiO_4 alone.

The magma ocean adiabat (Fig. 4.3) is based on the previously published thermodynamic data [45] and shows a significantly steeper slope than the komatiite adiabat that has long been considered for the magma ocean [51], in qualitative agreement with recent shock wave results [52]. The Grüneisen parameter γ governs the adiabat through

$$\gamma = \left[\frac{\partial \ln T}{\partial \ln \rho}\right]_S, \tag{4.6}$$

with ρ the density. We compute an adiabat with a potential temperature T_0=2163 K (the melting point of forsterite, [21]), and give a slightly colder (T_0=2000 K) and hotter (T_0= 2400 K) adiabat as envelopes for the thermal profile in the magma ocean. Using this adiabat we can establish a viscosity profile of the magma ocean using the viscosity fit (eq.4.5, Table 4.1) and find $\eta \sim 2.10^{-2}$ Pas at the surface, increasing to $\eta \sim 6.10^{-2}$ Pas at 32 GPa ($\sim$ 700 km).

Using these values of η we can compute an upper bound on the Prandtl number (Pr) and a lower bound on the Rayleigh number (Ra) for the terrestrial magma ocean to explore its convection dynamics:

$$Pr = \frac{\eta c_P}{k}, \tag{4.7}$$

$$Ra = \frac{\alpha c_P g \Delta T L^3 \rho^2}{k\eta}. \tag{4.8}$$

The thermodynamic parameters, i.e. thermal expansivity α, heat capacity c_P, and the mean density ρ can be estimated from our thermodynamic fit [45] (Table 4.2). For a magma ocean in the accretion stage the graviational accelaration g is in the range of a martian sized planet and the current Earth. The depth of the magma ocean L is estimated between 600 km (e.g. Righter [44]) to the depth of the whole mantle. With a dense insulating atmosphere [53, 54] the temperature difference ΔT throughout the magma ocean is that of the adiabat. The thermal conductivity k of silicate melts at high pressures is unexplored, but ambient pressure measurments on lavas [55] and synthetic samples [56] provide useful bounds.

Using the numerical values from Table 4.2 we obtain $Pr_{max} = 75$ and $Ra_{min} = 10^{27}$ which places the convection dynamics of the magma ocean in the convective regime of hard turbulence [13, 57]. In such a regime coherent large scale circulation occurs through constructive interference of random plume-like features. In the case of the magma ocean cold plumes sinking from the surface are the most likely cause of such coherent motion.

4.6 Conclusions

Simulations on transport properties of Mg_2SiO_4 by molecular dynamics at high pressures and temperatures by the flexible aspherical ion method yield results on diffusivity and viscosity that can readily be fit with an Arrhenius equation, but do not show the anomaly that was found for experimental measurements of depolymerized melts in the 10-15 GPa range. Combining a thermodynamic model for Mg_2SiO_4 melt [45] with the viscosity fit we are able to constrain an adiabat and a related viscosity profile through the magma ocean. The thermodynamic data and constraints on viscosity allow us to qualitatively consider the dynamic regime of the magma ocean by establishing an upper bound on the Prandtl ($Pr < 75$) and a lower bound on the Rayleigh number ($Ra > 10^{27}$). Further tighting of these constraints will depend on future work in geochemistry and simulations to determine the depth of magma ocean and size of the Earth at magma ocean stage.

4.7 Acknowledgments

This work was funded by the State of Bavaria through the Graduate School “Oxides” in the Elitenetzwerk Bayern. Computations were in part performed at the Leibniz Computer Center Munich. We greatly appreciate helpful discussion with N. de Koker, D. Dobson, D. Frost, and D.C. Rubie.

4.8 Tables

	X_0	E_a (kJ/mol)	V_a (cc/mol)
Diffusivity D	$(212 \pm 9)\cdot 10^{-9}$ m^2/s	101 ± 1	1.069 ± 0.004
Viscosity η	$(23.6 \pm 3.2)\cdot 10^{-5}$ Pas	83 ± 4	1.344 ± 0.021

Table 4.1: Parameters derived from fitting an Arrhenius relation to diffusivity (eq. 4.4) and viscosity (eq. 4.5). X_0 refers to D_0 and η_0, respectively.

Property	upper bound	lower bound
α (K^{-1})	$5 \cdot 10^{-5}$	$2 \cdot 10^{-5}$
c_P (J/kgK)	250	250
g (m/s^2	10	4
ΔT (K)	3000	1500
L (km)	3000	600
ρ (g/cm^3)	3.0	2.65
k (W/mK)	1.0	0.1
η (Pas)	$3 \cdot 10^{-2}$	$1 \cdot 10^{-2}$

Table 4.2: Upper and lower bounds on properties of the magma ocean and Mg_2SiO_4 melt.

4.9 Figures

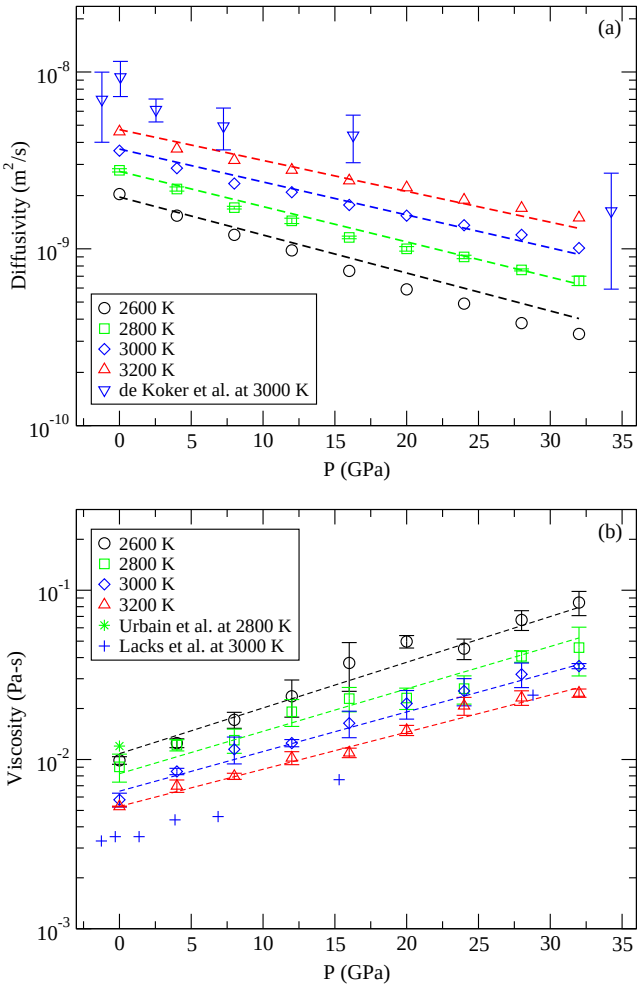

Figure 4.1: Pressure and temperature dependence of total diffusivity (a) and viscosity (b) in Mg_2SiO_4 melt. Values of different temperatures are shown by symbols and colors. The dashed lines represent fits to Arrhenius relation (eq. 4.4 for diffusivity and eq. 4.5 for viscosity). In the upper panel triangle show diffusivity results from *ab initio* computations at 3000 K [36]. In lower panel plus symbols are from rigid ion simulations at 3000 K [4]. The star shows ambient pressure viscosity from experiments extrapolated to 2800 K [1].

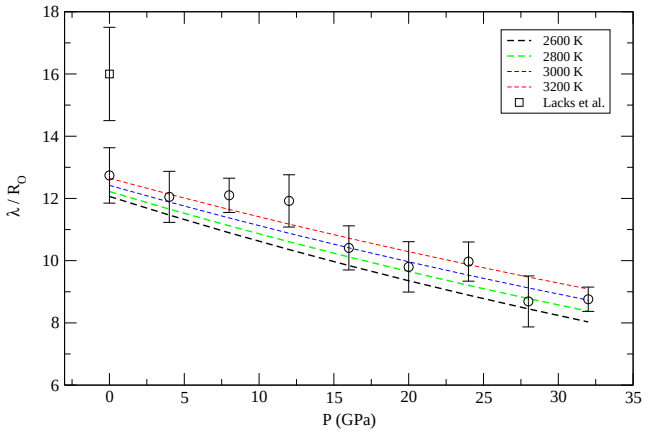

Figure 4.2: The pressure dependence of diffusion length λ, relating viscosity to diffusivity (eq. 4.1). Open circles are the λ values calculated directly from our simulations and dashed lines show λ from the independent fits of D and η with the Arrhenius equation. The open square is the result from the rigid ion simulations at 0 GPa [4].

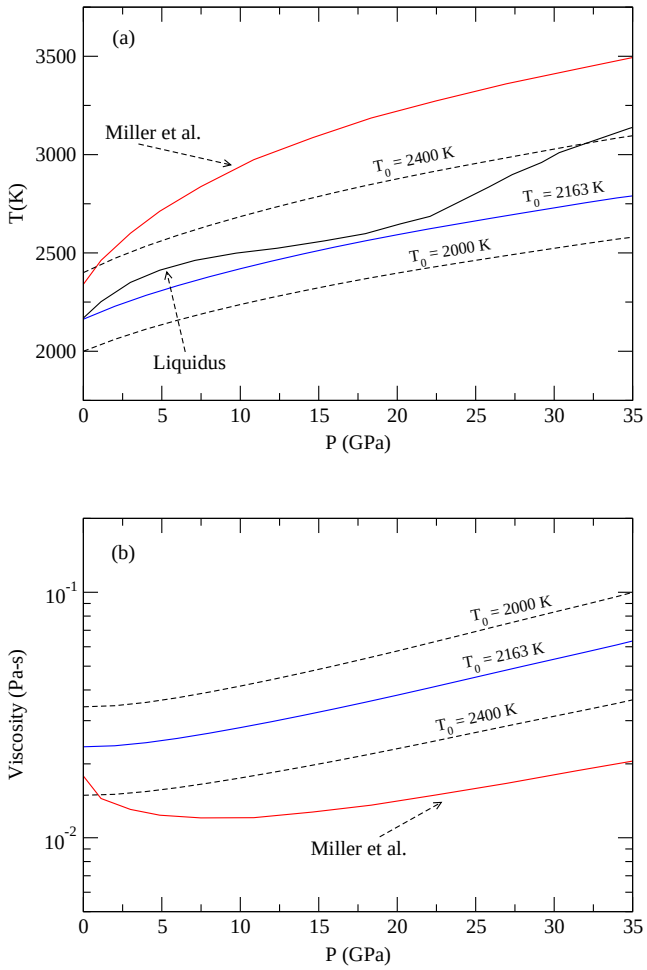

Figure 4.3: The adiabatic temperature profile of a forsterite magma ocean with a potential temperature T_0=2163 K (panel a) based on our previously published thermodynamic results on Mg_2SiO_4 melt [45] (blue solid line). Dashed lines represent slightly colder (T_0=2000 K) and hotter (T_0=2400 K) adiabats. Corresponding viscosity profiles of an Mg_2SiO_4 magma from our simulations using the Arrhenius fit (Table 4.1) are shown in panel b. For comparison the komatiite adiabat from Miller *et al.* [51] with T_0= 2300 K and corresponding viscosity profile are included, along with the liquidus of Mg_2SiO_4.

Bibliography

[1] Urbain, G., Bottinga, Y., Richet, P., 1982. Viscosity of liquid silica, silicates and alumino-silicates, Geochim. Cosmochim. Acta **46**, 1061-1072.

[2] Reid, J. E., Suzuki, A., Funakoshi, K., Terasaki, H., Poe, B.T., Rubie, D.C., Ohtani, E., 2003. The viscosity of $CaMgSi_2O_6$ liquid at pressures up to 13 GPa, Phys. Earth Planet. Inter. 139, 45-54.

[3] Liebske, C., Schmickler, B., Terasaki, H., T. Poe, B.T., Suzuki, A., Funakoshi, K., Ando, R., Rubie, D.C., 2005. Viscosity of peridotite liquid up to 13 GPa: Implications for magma ocean viscosities, Earth Planet. Sci. Lett. 240, 589-604.

[4] Lacks, D. L., D. B. Rear, J. A. Van Orman, Molecular dynamics investigation of viscosity, chemical diffusivities and partial molar volumes of liquids along the MgO-SiO_2 join as functions of pressure, Geochim. Cosmochim. Acta **71**, 1312 (2007).

[5] Lange, R. A., The effect of H_2O, CO_2 and F on the density and viscosity of silicate melts, Rev. Mineral. **30**, 331 (1994).

[6] Hui, H., and Y. Zhang, Toward a general viscosity equation for natural anhydrous and hydrous silicate melts, Geochim. Cosmochim. Acta, **71**, 403 (2007).

[7] Mookherjee, M., L. Stixrude, and B. Karki, Hydrous silicate melt at high pressure, Nature, **452**, 983 (2008).

[8] Revenaugh, J., and S. A. Sipkin, Seismic evidence for silicate melt atop the 410 km mantle discontinuity, Nature, **369**, 474 (1994).

[9] Garnero, E. J., and D. V. Helmberger, A very slow basal layer underlying large-scale low-velocity anomalies in the lower mantle beneath the Pacific: evidence from core phases, Phys. Earth Planet. Inter., **91**, 161 (1995).

[10] Williams, Q., and E. J. Garnero, Seismic evidence for partial melt at the base of Earth's mantle, *Science*, **273**, 1528 (1996).

[11] Rubie, D. C., C.K. Gessmann and D.J. Frost, Partitioning of oxygen during core formation of the Earth and Mars, Nature, **429**, 58 (2004).

[12] Abe, Y., Thermal and chemical evolution of the terrestrial magma ocean, Phys. Earth Planet. Inter. **100**, 27 (1997).

[13] Solomatov, V. S., Magma oceans and primordial mantle differentiation, in *Treatise on Geophysics*, edited by G. Schubert, Elsevier, **9**, 91 (2007).

[14] Solomatov, V. S., and D. J. Stevenson, Suspension in convective layers and style of differentiation of a terrestrial magma ocean, J. Geophys. Res. **98**, 5375 (1993).

[15] Solomatov, V. S., and D. J. Stevenson, Kinetics of crystal growth in a terrestrial magma ocean, J. Geophys. Res., **98**, 5407 (1993).

[16] Rubie, D. C., H.J. Melosh, J.E. Reid, C. Liebske and K. Righter, Mechanisms of metal-silicate equilibration in the terrestrial magma ocean, Earth Planet. Sci. Lett. **205**, 239 (2003).

[17] Allègre, C. J.,J. P. Poirier, E. Humler, and A. W. Hofmann, The chemical composition of the Earth, Earth Planet. Sci. Lett., **134**, 515 (1995).

[18] Ohtani, E., Kumazawa, M., 1981. Melting of forsterite Mg_2SiO_4 up to 15 GPa. Phys. Earth Planet. Inter. 27, 32-38.

[19] Kato, T., and M. Kumazawa, Effect of high-pressure on the melting relation in the system Mg_2SiO_4-$MgSiO_3$. 1. Eutectic relation up to 7 GPa, J. Phys. Earth, **33**, 513 (1985).

[20] Presnall, D. C., and T. Gasparik, Melting of enstatite ($MgSiO_3$) from 10 to 16.5 GPa and the forsterite (Mg_2SiO_4)-majorite (MgSiO3) eutectic at 16.5 GPa: implications for the origin of the mantle, J. Geophys. Res., **95**, 15771 (1990).

[21] Bowen, N.L., Andersen, O., 1914. The binary system MgO-SiO_2. Am. J. Sci. **37**, 487-500.

[22] Tangemann, J. A., Phyllips, B.L., Navrotsky, A., Weber, J.K.R., Hixson, A.D., Key, T.A., 2001. Vitreous forsterite (Mg_2SiO_4): Synthesis, structure, and thermochemistry. Geophysical research letters 28, 2517-2520.

[23] Lange, R. A., Carmichael, I.S.E., 1987. Densities of Na_2O-K_2O-CaO-MgO-FeO-Fe_2O_3-Al_2O_3-TiO_2-SiO_2 liquids: new measurements and derived partial molar properties. Geochim. Cosmochim. Acta 51, 2931-2946.

[24] Rigden, S. M., Ahrens, T.J., Stolper, E.M., 1989. High-pressure equation of state of molten anorthite and diopside. J. Geophys. Res. 94, 9508-9522.

[25] Kushiro, I., 1978. Density and viscosity of hydrous calc-alkalic andesite magma at high pressure, Year B.-Carnegie Inst. Wash. **77** , 1978 (675).

[26] Shimizu, N., and I. Kushiro, Diffusivity of oxygen in jadeite and diopside melts at high pressures, Geochim. Cosmochim. Acta, **48**, 1295 (1984).

[27] Poe, B. T., P.F. McMillan, D.C. Rubie, S. Chakraborty, J. Yarger and J. Diefenbacher, Silicon and oxygen self-diffusivities in silicate liquids measured to 15 gigapascals and 2800 Kelvin, *Science*, **276** 1245 (1997).

[28] Reid, J. E.,B.T. Poe, D.C. Rubie, N. Zotov and M. Wiedenbeck, The self-diffusion of silicon and oxygen in diopside ($CaMgSi_2O_6$) previous termliquid upnext term to 15 GPa, Chem. Geol. 174 (2001), 77-86.

[29] R. D. Shannon and C. T. Prewitt, Effective ionic radii in oxides and fluorides, Acta Cryst. B **25**, 925 (1969).

[30] Tinker, D.,C.E. Lesher, G.M. Baxter, T. Uchida and Y. Wang, High-pressure viscometry of polymerized silicate melts and limitations of the Eyring equation, Am. Mineral., **89**, 1701 (2004).

[31] Schmickler, B., Liebske, C., Holzapfel, C., Rubie, D.C., Viscosity of peridotite liquid up to 24 GPa predicted from self-diffusion coefficients. Eos Trans., Fall Meeting Suppl. Abstract 86, MR11A-06 (2005).

[32] Belonoshko, A. B., Skorodumova, N.V., Rosengren, A., Ahuja, R.,Johansson, B., Burakovsky, L., Preston, D.L., 2005. High-Pressure Melting of $MgSiO_3$. Phys. Rev. Lett. 94, 195701 (4 pages).

[33] Stixrude, L., Karki, B., 2005. Structure and freezing of $MgSiO_3$ liquid in Earth's lower mantle. Science 310, 297-299.

[34] Karki, B. B., Bhattarai, D., Stixrude, L., 2007. First-principles simulations of liquid silica: Structural and dynamical behavior at high pressure. Phys. Rev. B 76, 104205 (12 pages).

[35] Wan, J. T. K., Duffy, T. S., Scandolo, S., Car, R., 2007. First-principles study of density, viscosity, and diffusion coefficients of liquid $MgSiO_3$ at conditions of the Earth's deep mantle, J. Geophys. Res., 112, B03208, doi:10.1029/2005JB004135.

[36] de Koker, N. P., Stixrude, L., Karki, B.B., 2008. Thermodynamics, structure, dynamics, and freezing of Mg_2SiO_4 liquid at high pressure. Geochim. Cosmochim. Acta 72, 1427-1441.

[37] Gale, J. D., Catlow, C.R.A., Mackrodt, W.C., 1992. Periodic *ab initio* determination of interatomic potentials for alumina. Modell. Simul. Mater. Sci. Eng. 1, 73-81.

[38] Matsui, M., 1994. A transferable interatomic potential model for crystals and melts in the system CaO-MgO-Al_2O_3-SiO_2. Miner. Mag. 58A, 571-572.

[39] Guillot, B., Sator, N., 2007. A computer simulation study of natural silicate melts. Part I: Low pressure properties. Geochim. Cosmochim. Acta 71, 1249-1265.

[40] Guillot, B., Sator, N., 2007. A computer simulation study of natural silicate melts. Part II: High pressure properties. Geochim. Cosmochim. Acta 71, 4538-4556.

[41] Aguado, A., L. Bernasconi, S. Jahn, and P. A. Madden (2003), Multipoles and interaction potentials in ionic materials from planewave-DFT calculations. Faraday Discuss. **124**, 171-184.

[42] Madden, P. A., Heaton, R., Aguado, A., Jahn, S., 2006. From first-principles to material properties. J. Mol. Struct. (Theochem) 771, 9-18.

[43] Jahn, S., Madden P.A., 2007. Modeling Earth materials from crustal to lower mantle conditions: A transferable set of interaction potentials for the CMAS system. Phys. Earth Planet. Inter. **162**, 129-139.

[44] Righter, K., Metal-silicate partitioning of soderophile elements and core formation in the early Earth, Annu. Rev. Earth Planet. Sci. **31**, 135 (2003).

[45] Adjaoud, O., G. Steinle-Neumann, and S. Jahn, Mg_2SiO_4 liquid under high pressure from molecular dynamics, Chem. Geol., **256**, 185 (2008).

[46] Nosé, S., Klein, M.L., 1983. Constant pressure molecular dynamics for molecular systems. Mol. Phys. 50, 1055-1076.

[47] Martyna, G. J., Tobias, D.J., Klein, M.L., 1994. Constant pressure molecular dynamics algorithms. J. Chem. Phys. 101, 4177-4189.

[48] Allen, M.P., Tildesley, D.J., 1987. Computer Simulation of Liquids. Oxford University Press, New York.

[49] Stixrude, L., N. P. de Koker, N. Sun, M. Mookherjee, B. B. Karki, Thermodynamics of silicate liquids in the deep Earth, Earth Planet. Sci. Lett. (2009), doi:10.1016/j.epsl.2008.12.006.

[50] de Koker, N. P., and L. Stixrude, 2009. Self-Consistent Thermodynamic Description of Silicate Liquids, with Application to Shock Melting of MgO Periclase and $MgSiO_3$ Perovskite. Geophys. J. Int (in press).

[51] Miller, G. H., Stolper, E. M., and Ahrens, T. J., The Equation of State of a Molten Komatiite 2. Application to Komatiite Petrogenesis and the Hadean Mantle, Geophys. Res. **96**, 11849-11864 (1991).

[52] Mosenfelder, J.L., Asimow, P.D., Ahrens, T.J., 2007. Thermodynamic properties of Mg_2SiO_4 liquid at ultra-high pressures from shock measurements to 200 GPa on forsterite and wadsleyite. J. Geophys. Res. 112, B06208, doi:10.1029/2006JB004364.

[53] Hashimoto, G.L., Y. Abe, S. Sugita, 2007. The chemical composition of the early terrestrial atmosphere: Formation of a reducing atmosphere from CI-like material. J. Geophys. Res., **112**, 05010 (1990).

[54] Abe, Y., and T. Matsui Early evolution of the Earth: accretion, atmosphere formation, and thermal history, J. Geophys. Res. **91**, 291-302 (1986).

[55] (Buttner R., Zimanowski B., Lenk C., Koopmann A., Lorenz V, 2000. Determination of thermal conductivity of natural silicate melts. Appl. Phys. Lett. **77**, 1810-1812.

[56] Kang, Y., Morita, K., 2006. Thermal conductivity of the CaO-Al_2O_3-SiO_2 system. ISIJ INTERNATIONAL **46**, 420-426.

[57] Yuen, D. A., U. Hansen, W. Zhao, A. P. Vincent, and A. V. Malevsky, 1993. Hard Turbulent Thermal Convection and Thermal Evolution of the Mantle, J. Geophys. Res. **98**, 5355-5373.

Acknowledgments

This work has been performed in the frame of my Ph.D. thesis at Bayerisches Geoinstitut, University of Bayreuth. I acknowledge with thanks the Elitenetzwerk Bayern, International Graduate School program for funding my research projects.

First and foremost, I sincerly would like to thank Prof. Dr. David Rubie, who gave me the opportunity to perform this thesis at Bayerisches Geoinstitut.

I heartly thank Dr. Gerd Steinle-Neumann for his patience and constant guidance along all my Ph.D. He shared with me several of his ideas and never stopped his interest on my research works.

Warm thanks to Dr. Sandro Jahn who introduced me to the use of the AIM potential. I have enjoyed working with him and I am glad that I will join his group for a postdoctoral position.

Special thanks to Prof. Dr. Benjamin Burton who introduced me to the use of the MAPS code and for answering my questions about the ATAT package.

I thank Dr. David Dolejs, and Dr. Nico de Koker for fruitful discussions about my PhD projects.

Warm thanks to the entire administrative and technical stuff of the Bayerisches Geoinstitut for all the assistances.

I thank Prof. Dr. Hamid Bouzar from the University of Mouloud Mammeri of Tizi-Ouzou who put me on the rails of computational physics.

Thanks also to my friends for the nice time which we spend together and they allow me to think about other thing than the thesis. I would like to thank colleagues with whom I shared enjoyable discussions, jokes, beers and beers.

I thank everybody who directly and indirectly contributed to this thesis work.

To my parents, who have been away from the eyes but close to the heart, I dedicate with pleasure this thesis.

Omar Adjaoud

Bayreuth, February 2009

Erklärung

Hiermit versichere ich, die vorliegende Arbeit selbstständig verfasst und keine anderen als die von mir angegebenen Quellen und Hilfsmittel benutzt zu haben.

Ferner erkläre ich, dass ich weder an der Universität Bayreuth, noch an einer anderen Hochschule versucht habe, eine Dissertation einzureichen, oder mich einer Promotionsprüfung zu unterziehen.

Bayreuth, Februar 2009

Omar Adjaoud